Transition Metal-Doped Sb_2Te_3 and Bi_2Te_3 Diluted Magnetic Semiconductors

by

Yi-Jiunn Chien

A dissertation submitted in partial fulfillment
of the requirements for the degree of
Doctor of Philosophy
(Applied Physics)
in The University of Michigan
2007

Doctoral Committee:

Professor Ctirad Uher, Chair
Professor Bradford G . Orr
Professor Roy Clarke
Professor Xiaoqing Pan
Associate Professor Cagliyan Kurdak

© Yi-Jiunn Chien

All Rights Reserved

2007

DEDICATION

This Dissertation is dedicated to the Thermoelectric Physics Group at the University of Michigan.

ACKNOWLEDGMENTS

I first wish to thank Professor Ctirad Uher, my committee chair, academic advisor, and mentor. Throughout the past years, Professor Uher has done a great deal to assist me in completing this dissertation and has always supported me in my research. I am entirely grateful for his kindness, endless patience and enthusiasm, and for allowing me the freedom to continue at my sometimes very slow pace whenever I was stuck due to experimental difficulties.

My committee members deserve thanks for serving on my doctoral committee and for their helpful comments. Professors Orr and Clarke deserve special thanks for convincing me to enroll in the Applied Physics program, giving me very helpful advice on qualifying and preliminary exams, and encouraging me to pursue a Ph.D.

Special thanks are due to Professor Jeffrey S. Dyke and Dr. Zhenhua Zhou. They contributed a lot to my research when they were in our group as post-docs. The research presented in this dissertation would not have been possible without significant contributions from them.

My current lab mates, post-doc Dr. Xun Shi, my junior Huijun Kong and Lynn Endicott also merit special acknowledgement for helping me in the lab on a daily basis. I wish for many fruitful results to my smart junior Lynn, who has taken over this project and helped me a lot in proofreading my dissertation. I would like to thank Dr. Carl Henderson and Dr. Kai Sun at EMAL for their help on EPMA, SEM, TEM

and XPS measurement. I greatly appreciate their assistance.

I would like to thank these friendly Taiwanese people from Ann Arbor Taiwanese Association and Michigan Taiwanese Student Association. They helped me to adapt to my new environment and offered a lot of interesting activities to ease my homesickness. I also would like to thank my classmates and friends for their precious friendship. Without their warmth I can hardly imagine how I could have survived many cold Ann Arbor winters and the heavy workload at UM. I am so lucky to have all of them as friends. My studies at UM were greatly enriched by them.

I also recognize my friends in Taiwan for their efforts to smooth the way, as much as possible. Special thanks should go to my closest friend Bo-Ru Chen for always being able to cheer me up and making my life easier during these last few months.

My family has been a tremendous source of support over the years. My parents, Wen-Lin Chien and Yueh-Tao Lu, have been an endless source of encouragement and love. They taught me the value of hard work and devotion by example. They have always believed in me and had high expectations. I could never have reached this stage without their driving force. Thanks also go to Yi-Hui, Yi-Fang and Yi-Li for being my wonderful siblings who never hesitate to give their best support and encouragement.

Funding for this project was provided by the National Science Foundation Grant No. NSF-DMR-0305221 and No. NSF-DMR-0604549.

TABLE OF CONTENTS

DEDICATION ii

ACKNOWLEDGMENTS iii

LIST OF FIGURES x

LIST OF TABLES xiii

ABSTRACT xiv

Chapter 1 Introduction 1

1.1 Magnetic Semiconductors and Spintronics 1

1.2 The Early Development of Magnetic Semiconductors 2

1.3 Recent Studies on Diluted Magnetic Semiconductors (DMSs) 3

1.4 Mechanisms of Ferromagnetism in DMSs 6

1.5 Tetradymite-Type DMSs 10

1.6 Dissertation Outline 11

Chapter 2 Tetradymite-Type Diluted Magnetic Semiconductors 14

2.1 Introduction 14

2.2 Crystal Structure of Tetradymite-Type Semiconductors 14

2.3 Electrical Properties of Sb_2Te_3 and Bi_2Te_3 Tetradymite-Type Semiconductors 18

2.3.1 Semiconducting Properties of Sb_2Te_3 and Bi_2Te_3 18

2.4 Magnetic Properties of Bulk TM-Doped Tetradymite-Type Semiconductors 19

2.4.1 Discovery of Ferromagnetism in Transition Metal-Doped Tetradymite-Type Semiconductors 19
2.4.2 The Role of Transition Metals in Tetradymite Structure 19
2.4.3 Ionic Radius of Transition Metals...20
2.4.4 Solubility Limit of TMs in Sb_2Te_3 and Bi_2Te_3 21
2.5 Low-Temperature MBE Non-equilibrium Crystal Growth 22
2.6 Summary 22

Chapter 3 Experimental Methods...23
3.1 Introduction...23
3.2 Molecular Beam Epitaxy 24
3.2.1 The Configuration of the Custom Designed MBE System.................25
3.3 Standard Procedure for Sample Preparation 28
3.3.1 Growth Parameters..28
3.3.1.1 Pressure Detection 29
3.3.2 Substrate Consideration 30
3.3.2.1 Substrate Properties 30
3.3.2.2 Substrate Cleaning 31
3.3.2.3 *In situ* Substrate Cleaning 32
3.3.3 Metal Masks and Sample Cutting..32
3.4 Crystal Structural Determination 35
3.4.1 Reflective High Energy Electron Diffraction (RHEED) 35
3.4.2 X-Ray Scattering Techniques...38
3.4.2.1 X-Ray Diffraction 38
3.4.2.2 X-Ray Photoelectron Spectroscopy (XPS) 39
3.4.3 Electron Probe X-Ray Microanalyzer (EPMA)..................................40
3.4.4 Thin Film Thickness 40

3.5 Electrical and Magnetic Characterization 41
3.5.1 Magnetic Property Measurement System (MPMS) 41
3.5.1.1 Background and Substrate Response Subtraction 42
3.5.2 Determination of the Ordering Temperature 42
3.5.3 Hall Effect 44
3.5.3.1 Ordinary Hall Effect 44
3.5.3.2 Anomalous Hall Effect 45
3.5.4 Resistivity Measurement 45
3.6 Summary 46

Chapter 4 Epitaxial Thin Films of Vanadium-Doped Antimony Telluride 47
4.1 Introduction 47
4.2 Sample Preparation 47
4.2.1 Growth Parameters 48
4.2.1.1 Deposition Rate and Flux Ratio 48
4.2.1.2 Vanadium Flux Control 49
4.3 Structural Characterization 50
4.3.1 RHEED Patterns 50
4.3.2 X-Ray Diffraction (XRD) 53
4.3.3 EPMA and Chemical Properties 56
4.4 Transport and Magnetic Characterization 56
4.4.1 Transport Properties 56
4.4.2 Magnetization Measurement 58
4.4.2.1 Temperature-Dependent Magnetization 58
4.4.2.2 M(H) Hysteresis Loop 60
4.4.3 Arrott Plots 61

4.4.4 Anomalous Hall Effect 63
4.5 Discussion 65
4.6 Summary 67

Chapter 5 Chromium-Doped Tetradymite-Type Antimony Telluride 68
5.1 Introduction 68
5.2 Sample Preparation and Growth Condition 68
5.3 Structural Characterization 69
5.3.1 RHEED Patterns 69
5.3.2 EPMA 69
5.3.3 X-Ray Diffraction 70
5.3.4 Lattice Constants 71
5.4 Electrical and Magnetic Properties 72
5.4.1 Magnetization 73
5.4.2 Arrott Plots and Critical Temperatures 75
5.4.3 Resistivity and Transport Behavior 76
5.4.4 Hall Measurement 78
5.4.4.1 Hall Measurement and Carrier Concentration 78
5.4.4.2 Anomalous Hall Measurement 79
5.4.5 XPS Measurement 80
5.5 Discussion 83
5.6 Summary 85

Chapter 6 Iron-Doped Tetradymite-Type Bismuth Telluride 87
6.1 Introduction 87
6.2 Sample Preparation 87
6.3 Structural Determination 88

6.3.1 RHEED and XRD 88
6.3.2 Lattice Constants 88
6.4 Characterization 90
6.4.1 Transport Properties and Hall Measurement 90
6.4.2 Magnetic Properties of *n*-Type $Bi_{2-x}Fe_xTe_3$ 92
6.5 Discussion 92
6.6 Summary 93

Chapter 7 F/N/F Trilayer Structure 94
7.1 Introduction 94
7.2 Sample Preparation 94
7.3 Interlayer Exchange Coupling (IEC) 95
7.4 IEC on F/N/F Trilayers 96
7.5 Characteristics 99
7.6 Summary 103

Chapter 8 Conclusions 104
8.1 Conclusions 104
8.2 Future Work 105

BIBLIOGRAPHY 107

LIST OF FIGURES

Figure 2.1 Atomic layers in the Sb_2Te_3 crystal structure. Dashed lines indicate van der Waals gaps separating five-atomic layer lamella. The octahedral coordination is highlighted for a $Te^{(2)}$ atom. 16

Figure 2.2 The unit cell of Sb_2Te_3 crystal under the hexagonal representation. 17

Figure 3.1 Our custom designed MBE thin film deposition system. 24

Figure 3.2 A schematic of the growth chamber with various ports marked. 25

Figure 3.3 The schematic picture of the sample holder from both the side view and the top view. 34

Figure 3.4 Two metal masks designed for Hall effect and transport measurements. 34

Figure 3.5 A RHEED pattern observed on clear sapphire (0001) plane. 36

Figure 3.6 The origin of streaks and Laue circles according to the Ewald's sphere construction. 37

Figure 4.1 RHEED patterns of a (0001) sapphire substrate for $[0\ 1\ \bar{1}\ 0]$ incident beam after 30min 850°C *in situ* substrate cleaning. 51

Figure 4.2 RHEED patterns observed during the first 10nm of $Sb_{2-x}V_xTe_3$ growth for $[2\ \bar{1}\ \bar{1}\ 0]$ incident beam. 52

Figure 4.3 RHEED pattern observed after the first 10nm of $Sb_{2-x}V_xTe_3$ growth for $[2\ \bar{1}\ \bar{1}\ 0]$ incident beam. 52

Figure 4.4 X-ray diffraction pattern from a bulk Sb_2Te_3 crystal and from $Sb_{2-x}V_xTe_3$ epitaxial thin films for x=0, 0.15, 0.32 and 0.35 54

Figure 4.5 Lattice constants and cell volumes of $Sb_{2-x}V_xTe_3$ films vs. vanadium fraction x. 55

Figure 4.6 Temperature-dependent electrical resistivity of $Sb_{2-x}V_xTe_3$ films grown on sapphire (0 0 0 1) substrates. 58

Figure 4.7 Temperature-dependent magnetization of $Sb_{2-x}V_xTe_3$ (x=0.15, 0.32, 0.35) thin films during field cooling from 300 to 2 K in the field of 500 Oe applied parallel to the c axis of the films. The arrows mark the inflection points on the curves. 60

Figure 4.8 Hysteresis loops obtained on the $Sb_{1.65}V_{0.35}Te_3$ film at 2K and 160K. ..61

Figure 4.9 The Arrott plot for a thin-film sample $Sb_{1.65}V_{0.35}Te_3$ that yields the ordering temperature of 177 K. 62

Figure 4.10 Ordering temperature of $Sb_{2-x}V_xTe_3$ thin films as a function of the vanadium concentration x. The error bars indicate an uncertainty in the content of vanadium. 63

Figure 4.11 Hysteresis loops in the Hall effect and magnetoresistance observed at 2K on a film with the composition $Sb_{1.65}V_{0.35}Te_3$. 64

Figure 5.1 X-ray diffraction patterns of $Sb_{2-x}Cr_xTe_3$ films on sapphire (0001) substrates. 70

Figure 5.2 Lattice constants of $Sb_{2-x}Cr_xTe_3$ films as a function of Cr fraction x. 72

Figure 5.3 Temperature dependent magnetization of $Sb_{2-x}Cr_xTe_3$ thin films. 74

Figure 5.4 Magnetic hysteresis loops of $Sb_{2-x}Cr_xTe_3$ thin films. 75

Figure 5.5 Curie temperature of $Sb_{2-x}Cr_xTe_3$ thin films as a function of Cr concentration x. 76

Figure 5.6 Temperature dependent electrical resistivity of $Sb_{2-x}Cr_xTe_3$ films in zero magnetic field. 77

Figure 5.7 Room temperature hole concentration as a function of Cr content x. 79

Figure 5.8 Magnetic field dependent Hall resistivity of $Sb_{2-x}Cr_xTe_3$ films. 80

Figure 5.9 XPS Spectrum of the $Sb_{1.78}Cr_{0.22}Te_3$ thin film sample before ion etching and after 40mins, 90mins and 140mins ion etching, marked with specific

binding energies of related elements..82

Figure 5.10 The enlarged XPS spectrum for binding energy around 575eV for the analysis of Cr...83

Figure 5.11 Curie temperature of $Sb_{2-x}Cr_xTe_3$ thin films as a function of $xp^{1/3}$.........85

Figure 6.1 a-axis lattice constant a vs. Fe fraction x 89

Figure 6.2 c-axis lattice constant vs Fe fraction x 89

Figure 6.3 Temperature dependent electrical resistivity of $Bi_{2-x}Fe_xTe_3$ films in zero magnetic field...91

Figure 7.1 A schematic of the *F*/*N*/*F* trilayer structure based on $Sb_{2-x}Cr_xTe_3/Sb_2Te_3/Sb_{2-y}Cr_yTe_3$. The coercive fields for $Sb_{2-x}Cr_xTe_3$ and $Sb_{2-y}Cr_yTe_3$ ferromagnetic layers are assumed to be H_{c2} and H_{c1} respectively. 97

Figure 7.2 (Left side) A schematic of the spin configuration of the *F*/*N*/*F* trilayer *without* IEC. (Right) A schematic of the spin configuration of the *F*/*N*/*F* trilayer *with* IEC...98

Figure 7.3 Magnetic field-dependent Hall resistivity for $Sb_{1.66}Cr_{0.34}Te_3$/ Sb_2Te_3/ $Sb_{1.81}Cr_{0.19}Te_3$ trilayer structures with various spacer thickness: (a) 10 nm, (c) 4 nm, (e) 2 nm, and (g) 0 nm. Coercive fields as a function of temperature for $Sb_{1.66}Cr_{0.34}Te_3$ /Sb_2Te_3/ $Sb_{1.81}Cr_{0.19}Te_3$ trilayer structures with various spacer thickness: (b) 10 nm, (d) 4 nm, (f) 2 nm, and (h) 0 nm. 100

Figure 7.4 Saturation field H_S as a function of temperature and Sb_2Te_3 spacer thickness...103

LIST OF TABLES

Table 2.1 A list of radii of various transition metal ions and Sb^{3+}, Bi^{3+}, and Te^{2-} 21

Table 4.1 Effusion cell temperatures and deposition rates of antimony and tellurium for $Sb_{2-x}V_xTe_3$ epilayer growth. 49

Table 4.2 A list of vanadium deposition rates given by different e-beam power levels. e-beam current and chamber pressure are also listed for reference. 50

Table 4.3 Hall coefficient (R_H), carrier concentration (p), resistivity (ρ) and mobility (μ) of a single crystal of Sb_2Te_3 and of $Sb_{2-x}V_xTe_3$ films at 300K. 57

Table 5.1 Chromium fraction and film thickness measured on different samples. 70

Table 6.1 Carrier concentration (n or p), resistivity (ρ) and mobility (μ) of a single crystal of Bi_2Te_3 and of $Bi_{2-x}Fe_xTe_3$ films at 10K. 91

ABSTRACT

Transition Metal-Doped Sb_2Te_3 and Bi_2Te_3 Diluted Magnetic Semiconductors

by
Yi-Jiunn Chien

Chair: Ctirad Uher

Motivated by the discovery of the ferromagnetic order in V-doped Sb_2Te_3 and Fe-doped Bi_2Te_3 bulk crystals, the study of the transition metal (TM) doped tetradymite-type semiconductors was extended to their thin film forms with the hope of significantly increasing the content of TM and thus enhancing the Curie temperature. High quality $Sb_{2-x}V_xTe_3$ (x up to 0.35) and $Sb_{2-x}Cr_xTe_3$ (x up to 0.59) epitaxial films have been successfully prepared on sapphire (0001) substrates by non-equilibrium MBE growth technique, and their structural, transport and magnetic properties have been determined. Magnetization studies, Arrott plot analyses, and anomalous Hall effect measurements indicate that long range magnetic order persists to temperatures of at least 177K (in the case of $Sb_{2-x}V_xTe_3$) and 190K (for $Sb_{2-x}Cr_xTe_3$). The observed carrier mediated, *p*-type favored ferromagnetic behavior supports a

scenario of RKKY interaction with mean-field approximation. $Bi_{2-x}Fe_xTe_3$ samples have also been prepared (for x up to 0.46), and they displayed n-type behavior and no signature of spontaneous magnetic ordering down to 2K. Trilayer structures with a normal Sb_2Te_3 layer sandwiched between two ferromagnetic $Sb_{2-x}Cr_xTe_3$ layers were fabricated in order to explore the influence of the interlayer exchange coupling mechanism (IEC). Such coupling was found to be present for small thickness of the spacer layer at low temperatures. Transition metal-doped tetradymite-type semiconductors represent a new class of diluted magnetic semiconductors that are octahedrally coordinated and that possess highly anisotropic structural and magnetic properties.

Chapter 1
Introduction

1.1 Magnetic Semiconductors and Spintronics

The remarkable achievements in the field of microelectronics and information technologies have had an enormous impact on our daily life and have changed the style of living all over the world. Whenever people use computers to facilitate their work, deliver messages over the Internet, watch TV or enjoy a song on their i-Pod, they are essentially exploiting the properties of electron charge and spin. Microelectronic devices and circuits were invented for data processing by manipulating the electron charge, while electron spin was used in data storage media such as a hard disk in a computer, a magnetic tape for a camcorder or Magnetoresistive Random Access Memory (MRAM). The conventional semiconductors currently used in microelectronic devices, integrated circuits and optoelectronic devices, such as silicon and GaAs are all non-magnetic. In this case the spin property of carriers is neglected and only the charge property is used. The great progress achieved in miniaturization of the devices and in increasing their packing density on chips, the process well described by Moore's law, has now reached a distinct bottleneck; the devices are starting to approach the fundamental fabrication and performance limit. Even if a major breakthrough is made in the fabrication process, these scaled down electronic devices will not function properly since the

quantum effects can no longer be neglected in the nanoscale regime. In nanostructures where conventional devices for manipulating electron charges come to a dead end of miniaturization, magnetic exchange interactions have more pronounced effects, and manipulation of the quantum mechanics spin states becomes more relevant. Thus the use of spin in semiconductors for data processing represents an exciting new concept called spintronics (a neologism for "spin-based electronics").

Generating a current of spin polarized electrons, preserving the spin polarization, manipulating spin states and sensing the polarization are basic requirements for realization of spintronic technologies. The simplest method of generating a spin polarized current is to run the current through a ferromagnetic material. Ferromagnetic materials can function as a spin supplier and injector. Ferromagnetic metals were considered to be the first and obvious candidate since their Curie temperatures are above room temperature. However, the spin injection efficiencies of ferromagnetic metals were found to be very low, on the order of ~1% [1]. This low spin injection efficiency is due to the conductivity mismatch at the metal-semiconductor interface. Advances in material science have led to the development of ferromagnetic semiconductors which are believed to have better injection efficiency.

1.2 The Early Development of Magnetic Semiconductors

The nature of tunable conductivity in semiconductors makes magnetic semiconductors a better candidate. A better spin injection efficiency can be achieved by matching the conductivity of the channel material by way of altering the dopant level in magnetic semiconductors. Long range order magnetism of semiconductors had been seen in some structures (Eu chalcogenides and certain semiconducting

spinels [2]) as early as the late 1960s, and extensive studies have been made of the coexistence of magnetism and semiconducting property. However, due to the difficulty of fabrication in a thin film form and lacking a reliable control of their doping level, these early developed magnetic semiconductors are hardly compatible with current mainstream semiconductors widely used in the industry such as GaAs and silicon. Instead of seeking these unique magnetic semiconductor structures, a more productive way is to introduce magnetic ions to non-magnetic semiconductors. This approach was initially pursued in II-VI compound semiconductor systems such as CdTe and HgTe alloyed with MnTe. The non-magnetic CdTe and HgTe semiconductors can become magnetic after introducing 2^+ manganese ions into their semiconducting structure. In this case, the concentration of Mn can be very high since the divalent Cd or Hg cations can be easily replaced by Mn. Therefore, the magnetism is believed to arise as a consequence of direct exchange between the Mn^{2+} ions leading to either paramagnetic or antiferromagnetic coupling or to a spin-glass state [3,4]. Ferromagnetism was found difficult to achieve by this approach. One study [5] indicated that an n-type II-VI compound of arbitrary large carrier concentration will not hold ferromagnetism above 1K.

1.3 Recent Studies on Diluted Magnetic Semiconductors (DMSs)

A superior approach is to use a diluted magnetic semiconductor. Diluted magnetic semiconductors (DMS) are semiconducting materials with a small fraction of the host cations replaced by some transition metal or rare earth ions which dramatically change the magnetic properties of the host semiconductor but act just like dopants and leave the important nature of semiconductivity substantially unchanged. These transition metals and rare earths play the role of magnetic

impurities since they can form partially filled *d* states or *f* states. These partially filled states contain unpaired electrons, and the unpaired spins of these electrons support the magnetic behavior in the DMS. Since the semi-conductive nature is preserved in DMS, the conductivity can be tuned by altering the doping level to match that of the channel material and thus enhance the spin injection efficiency. Aside from the gains in spin injection efficiency, another distinct advantage of DMS materials is their carrier-mediated nature of ferromagnetism, which enables tuning and control of the magnetic properties by applying a gate voltage or by optical excitation of charge carriers. The ability to control magnetic properties and spin states of DMSs by the application of light and electric fields gives rise to a new concept to develop entirely new devices having unconventional properties that can use the degrees of freedom of both charge and spin. Semiconductor quantum spin electronics with applications in quantum computing is also an area that has greatly benefited from the progress in diluted magnetic semiconductors. The electron spin is a natural candidate for the qubit—the fundamental unit of quantum information. In step with the progress in the research on non-magnetic semiconductors and quantum-confined nanostructures such as quantum wells and quantum dots, diluted magnetic semiconductors make it possible to manipulate spin directly as a quantum mechanical entity.

Mn-doped III-V compound diluted magnetic semiconductors have attracted much interest because their host semiconductors such as GaAs, InAs and InP are mature materials for optoelectronic and high speed IC applications. The equilibrium solubility of magnetic impurities in III-V semiconductors, however, is very low and these magnetic impurities tend to segregate and form secondary phases. Thus an ideal density of magnetic impurities cannot be obtained by using conventional equilibrium crystal growth methods. The first successful non-equilibrium DMS epilayer growth

was demonstrated by Munekata, *et al.* [6]. They used low-temperature molecular beam epitaxy (LT-MBE) to achieve the epitaxial growth of InMnAs on GaAs substrate and successfully suppressed the surface segregation and second phase formation. This, in turn, led to the discovery of ferromagnetism in *p*-type InMnAs at low temperatures [7]. In 1996 the epitaxial growth of GaAs-based DMS — specifically GaMnAs films — was demonstrated and ferromagnetic transition was reported at somewhat higher temperatures [8]. After intensive study in this field for over a decade, the highest Curie temperature reported on GaMnAs is around 170K [9]. An important finding concerning the direction of magnetization should be mentioned in this research field. It turns out that the easy axis of magnetization in GaMnAs grown on GaAs (001) plane is oriented within the plane due to the compressive strain since the lattice constant of GaMnAs is slightly larger than that of GaAs. In contrast, the pseudomorphic InMnAs epilayer on a GaAs substrate under biaxial tensile strain tends to have an easy axis of magnetization oriented perpendicular to the plane. This interesting strain-dependent behavior of magnetization orientation offers an interesting way to manipulate the direction of the easy axis of magnetization in epilayers. On the other hand, strain may lead to segregation and clustering which are bad for DMS preparations. One can easily enhance or reduce the effect of strain by simply introducing a proper buffer layer.

Interest in the wider band gap DMSs was aroused by the theoretical prediction of Dietl and coworkers [5]. Based on their work, wider band gap DMSs should have higher Curie temperatures. It was suggested theoretically that Mn-doped ZnO and GaN would exhibit higher than room temperature ferromagnetism, and this prediction was subsequently verified by several experimental results on wider bandgap DMSs. Ferromagnetic transition above room temperature was reported for Mn-doped GaN

[10,11], Mn-doped ZnO [12,13,14] and transition metal-doped TiO_2 [15,16]. Above room temperature ferromagnetism was also found in other crystal systems such as Mn-doped GaP [17], $(Cd_{1-x}Mn_x)GeP_2$ [18], $(Zn_{1-x}Mn_x)GeP_2$ [19] although they are not necessarily wide bandgap materials.

Although many appealing results have been demonstrated in these DMS systems, the magnetic order in some of these systems was realized as a result of phase-segregated magnetic impurities, and spin-polarized carriers cannot be obtained in some of these materials above room temperature [20]. Additionally, many of these oxide systems are rather poor electrical conductors.

1.4 Mechanisms of Ferromagnetism in DMSs

In the above DMSs, even though the density of magnetic impurities can be increased by non-equilibrium LT-MBE technique, the density is still very low compared to the density of the host atoms, thus these magnetic impurities are far apart. Therefore, the large distance between the closest magnetic impurities makes direct coupling impossible. Another important experimental fact is that ferromagnetism in these DMSs is observed only when the structure is a *p*-type semiconductor. The carrier dependence behavior and low magnetic impurity density imply that the ferromagnetic interaction is carrier-induced via indirect coupling. A variety of theoretical models based on mean field theory or first principle calculations has been proposed to understand the mechanism of ferromagnetism in DMSs. Ruderman-Kittel-Kasuya-Yoshida (RKKY) interaction is the most famous one in dealing with long-range indirect coupling. In the RKKY model, the sea of free charge carriers is polarized in the form of long range oscillatory polarization waves by a magnetic ion and carries this information to another ion, where the indirect coupling

can be either in the same or opposite direction depending on the separation of the two ions. This indirect exchange mechanism is the essential feature of magnetism in metals containing dilute magnetic impurities. In semiconductors, the typical carrier density is much lower than in metals, by around three to five orders of magnitude (~10^{19} /cm^3 in semiconductors and larger than 10^{23}/cm^3 in metals). Thus, in a DMS, the mean distance between the charge carriers is comparable or even larger than the distance between the magnetic impurities. As a consequence, for a DMS with a typical carrier density, the period of the Friedel oscillations becomes very large, and the first zero of the oscillation falls at a distance greater than the cut-off length of the indirect exchange interaction. In this case, the RKKY interaction degenerates into the Zener model of magnetism [21] developed in 1950. To gain a better feel for how the RKKY approach becomes equivalent to the Zener model, it is helpful to consider some simple theoretical estimates. Strictly speaking, the Zener model can be regarded as a special result of the RKKY interaction under the mean field approximation.

Consider the coupling between conduction electrons or holes and a localized spin, the so called "*s-d* interaction". We can begin with the Anderson Hamiltonian

$$H = \sum_{k\sigma} \epsilon_{k\sigma} c_{k\sigma}^{\dagger} c_{k\sigma} + \sum_{\sigma} \epsilon_d n_{d\sigma} + U n_{d\uparrow} n_{d\downarrow} + \sum_{k\sigma} \left(V_k c_{k\sigma}^{\dagger} d_{\sigma} + V_k^* d_{\sigma}^{\dagger} c_{k\sigma} \right) \quad . \tag{1}$$

After the 2nd order perturbation on V, one can find the Hamiltonian of s-d interaction

$$H_{ij} = J_{ij} S_i \cdot S_j \, , \tag{2}$$

where J_{ij} is a coupling coefficient that can be expressed in the following form

$$J_{ij} = \frac{\rho_d(\varepsilon_F) k_F^d I^2}{2\pi} F_d(2k_F |r_i - r_j|) |\varphi_o(\zeta_i)|^2 |\varphi_o(\zeta_j)|^2 \, , \tag{3}$$

$\rho_d(\varepsilon_F)$ is the density of states of the carriers at the Fermi level, k_F is the Fermi wave vector, I is the exchange integral, r is the vector in the *d*-dimensional space,

and $\varphi_o(\zeta)$ is the ground-state envelope function of the carriers in the confining potential $V(\zeta)$. For 1D, 2D and 3D, the function F_d has the following forms

$$
\begin{aligned}
&F_1(x) = -\pi \mathrm{si}(x)/2, \\
&F_2(x) = \int_1^{\infty} dt \frac{\Im_1(xt)}{xt(t^2-1)^{1/2}}, \\
&F_3(x) = [\sin(x) - x\cos(x)]/x^4,
\end{aligned}
\tag{4}
$$

where $\mathrm{si}(x)$ is the sine-integral and $\Im_n(xt)$ is the Bessel function. One can obtain the asymptotic behavior of $F_d(x)$:

$$
\left\{
\begin{aligned}
&F_1(x) \cong \pi\cos(x)/2x \\
&F_2(x) \cong \sin(x)/x^2 \\
&F_3(x) \cong -\cos(x)/x^3
\end{aligned}
\right\} \text{ for } x \gg 1 \ , \tag{5}
$$

and

$$
\left\{
\begin{aligned}
&F_1(x) \cong \pi/4 \\
&F_2(x) \cong [1/2 - \gamma + \ln(4/x)]/2 \\
&F_3(x) \cong 3/x
\end{aligned}
\right\} \text{ for } x \to 0, \tag{6}
$$

where γ =0.57721 is the Euler constant.

For example, one can get the following result for 1D RKKY interaction.

$$J_{ij}^{1D} = -J^2[\frac{\pi}{2} - si(2k_F R)], \tag{7}$$

and

$$H \propto -J^2[\frac{\pi}{2} - si(2k_F R)]S_1 \cdot S_2 \cong -J^2\frac{\cos(2k_F R)}{2k_F R}S_1 \cdot S_2 \ \text{ for } \ k_F R \gg 1, \tag{8}$$

where $R = r_i - r_j$ is the average distance between two close magnetic ions, J is the interaction constant and k_F is the Fermi wave vector. This formula indicates that the interaction decreases as $1/k_F R$, oscillates with a period of π/k_F, and has a collinear coupling behavior of local spins.

Now we can take the next step to calculate the mean-field value of the

Curie-Weiss temperature of spins located at ζ_i, given by the formula below

$$\Theta(\zeta_i) = S(S+1)\sum_j J_{ij} / 3k_B \quad . \tag{9}$$

In semiconductors, the distance between the nearest-neighbors is much smaller than the period of the oscillation function in $F_d(x)$. Therefore, $x = 2k_F R \ll 1$, and it allows us to replace the summation over the ion position by an integration extending from $x = 0$ to ∞. Assume that the distribution of magnetic ions is random and their effective concentration $\tilde{x}N_0$ is microscopically uniform. Then Θ can be rewritten as

$$\Theta(\zeta) = S(S+1)\tilde{x}N_0\rho_d(\varepsilon_F)\left|\varphi_o(\zeta)\right|^2 I^2 / 12k_B, \tag{10}$$

which shows that the net RKKY interaction is ferromagnetic, i.e. $\Theta > 0$. From this simple result, we can easily see that Θ is proportional to the effective mass, to the concentration $\tilde{x}N_0$, to the degree of confinement, and to I^2. It is reasonable to expect much greater Θ in the presence of holes than electrons because of the generally greater effective mass of holes.

The important experimental fact of the *p*-type dominant ferromagnetism observed in the DMSs is usually explained in term of the small effective mass of electrons and the small exchange integral for the conduction band. The RKKY related Zener model is in accord with some recent experimental results. However, the validity of the RKKY interaction as applied to the III-V DMS has been questioned by some theorists [22,23,24,25]. The objection concerns the likely dual role played by manganese in these structures; in other words, manganese not only contributes magnetic ions but also acts as an acceptor, and a significant fraction of the charge carrying holes may have the Mn 3*d* character. The *d*-states of manganese are very different from free electron states and shouldn't be regarded as a part of the RKKY

picture. Based on these arguments, first principle calculations have been suggested instead of the RKKY picture. By first principle calculations on a model of *d*-electrons, Akai *et al*. [22] showed that when holes are present, the half-metallic ferromagnetic state becomes stable. The ferromagnetism was considered to be a result of double exchange interaction caused by hopping of *d*-holes.

Aside from the ones just mentioned above, many other theoretical models based on density function theory and *ab initio* band structure calculation have been proposed to understand the magnetic and transport properties of DMSs. Whether they prove useful or not, only time will tell. The RKKY theory and these first principle calculations are based on Bloch wave functions and most of these models include mean field approximation. Therefore, an ideal DMS for the related research fields should have a homogenous magnetic impurities distribution and crystalline ordering.

1.5 Tetradymite-Type DMSs

In 2003, while studying the effect of transition metal impurities in bulk single crystals of the archetypal thermoelectric materials Sb_2Te_3 and Bi_2Te_3, our group and, independently a team in Russia, observed that vanadium in Sb_2Te_3 [26] and Fe in Bi_2Te_3 [27] stimulate ferromagnetism with a Curie temperature of about 23K and 12K, respectively. In the study, very small amounts of vanadium (1~3 atomic %) doped in the matrix of Sb_2Te_3 can lead to a robust ferromagnetic state. The magnetization results showed a highly anisotropic manner of the ferromagnetism—the easy axis of magnetization is oriented along the c-axis while the magnetic susceptibility has a simple paramagnetic behavior with no hint of magnetic ordering when an external magnetic field is applied perpendicular to the c-axis. Most of the DMS materials currently under study crystallize in either zinc-blende or wurtzite structure by

establishing tetrahedral bonds between atoms. Our tetradymite-type DMSs based on Sb_2Te_3 have a very different crystal structure and different magnetic impurity. Both Sb_2Te_3 and Bi_2Te_3 crystallize in a highly anisotropic tetradymite-type structure where atoms form an octahedral coordination. If transition metal atoms are introduced to the tetradymite-type structure, there are various possible ionic states and the spin-orbit interaction would also be much more complicated due to the expanded octet bonding where not only *p*-orbitals but also *d*-orbitals join the hybridization. The complicated feature of tetradymite structure on one hand causes the difficulty in theoretical calculation, but on the other hand gives a lot of structural and chemical factors which might yield new, unexpected electronic and magnetic properties. The detailed crystal structure and properties of tetradymite-type DMSs will be described in the next chapter.

1.6 Dissertation Outline

This thesis is devoted to the investigation of a number of structural, electric and magnetic properties of the transition metal doped antimony telluride and bismuth telluride compound, prepared as epitaxial, monocrystalline thin films.

In the coming chapter, the unique structure of tetradymite-type Sb_2Te_3 and Bi_2Te_3 will be introduced. Inspired by the versatility of transition metal oxides, transition metals doped into the tetradymite structure may have a variety of *d*-electron hybridization forms and thus increase the possibility of strong spin exchange interactions. In order to estimate this possibility, a series of transition metals will be analyzed in terms of their *d*-shell configuration, the ionic radius and of the different valence number.

The experimental techniques employed for growth and for structural, electric and magnetic characterization of the transition metal-doped antimony telluride and bismuth telluride thin films are presented in Chapter 3. First, every component of our custom-designed compact, low-temperature molecular beam epitaxy system will be described in detail, and then the important *in situ* surface morphology monitoring tool—RHEED will also be mentioned. In the second part, a standard procedure for preparing epitaxial thin films will be described. The last part will focus on various techniques for characterizing the crystal structures, electron transport and magnetic properties of our epitaxial thin film samples.

In Chapters 4 and 5, attention will be paid to the Sb_2Te_3 based diluted magnetic semiconductor system. Both vanadium and chromium have been successfully introduced into Sb_2Te_3 during an epitaxial growth, yielding Curie temperatures of 177K and 190K, respectively.

Chapter 6 is dedicated to the study of Fe-doped Bi_2Te_3 diluted magnetic semiconductors. Although bulk $Bi_{2-x}Fe_xTe_3$ crystal was confirmed to have ferromagnetic ordering at around 12K, Fe-doped Bi_2Te_3 epitaxial thin films prepared in our lab tend to be *n*-type and show no spontaneous magnetic ordering even at a temperature as low as 2K. Possible reasons for the discrepancy between bulk and thin film samples will be discussed.

In Chapter 7 we demonstrate a Ferromagnetic-Normal-Ferromagnetic (F/N/F) trilayer epitaxial structure based on $Sb_{2-x}Cr_xTe_3$ diluted magnetic semiconductors. The non-magnetic Sb_2Te_3 layer sandwiched between two ferromagnetic layers plays very interesting role for verification of the interlayer exchange coupling. This work can be regarded as a successful initial step for future advanced multilayer spintronic devices based on the Sb_2Te_3 system.

Chapter 8 is a summary of all previous studies in this dissertation. Conclusions and suggestions for future work will also be included in this last chapter.

Chapter 2
Tetradymite-Type Diluted Magnetic Semiconductors

2.1 Introduction

This chapter introduces basic properties and describes the special crystal structure of tetradymite-type $A_2^{V}B_3^{VI}$ (*A*=Sb, Bi; *B*=Sb) V-VI compound semiconductors. In this dissertation, most of the efforts are devoted to Sb_2Te_3 and Bi_2Te_3 since ferromagnetic transitions were first discovered in bulk forms of these two tetradymite-type compounds with transition metal doping. Transition metals must play important roles in these tetradymite-type crystals so that small doping levels can arouse a significant ferromagnetic response. This discovery motivated follow-up research on thin films to fully explore the concentration dependence of the Curie temperature and to understand the possible mechanisms of ferromagnetism in these transition metal-doped Sb_2Te_3 and Bi_2Te_3. We utilized low temperature MBE growth of the films to increase the concentration of the transition metal elements and we made thorough investigation of their magnetic properties.

2.2 Crystal Structure of Tetradymite-Type Semiconductors

The word *tetradymite* is used to describe minerals consisting of bismuth, tellurium and sulfur, Bi_2Te_2S, also known as telluric bismuth. Since a set of similar

V-VI group compounds with a formula form of $A_2^{V}B_3^{VI}$ (A=Bi, Sb and B=Te, Se) tends to crystallize in the same structure as Bi_2Te_2S, tertadymite-type structure became a general term to describe this special crystalline structure. The crystal lattice is rhombohedral (or trigonal) and belongs to a space group of $R\overline{3}m\text{-}D_{3d}^{5}$. There is a perfect cleavage parallel to the basal plane, and these minerals usually occur in foliated masses of irregular outline due to the weak van der Waal bonding. The essence of the tetradymite-type lattice in $A_2^{V}B_3^{VI}$ (A=Bi, Sb and B=Te, Se) is characterized by the octahedral bonding (with dsp^3 and d^2sp^3 hybridizations) and a van der Waals gap separating five atom layer lamellae. The sequence of layers within the lamellae, for example in Sb_2Te_3, is

Te $^{(1)}$—Sb—Te $^{(2)}$—Sb—Te $^{(1)}$

in the plane perpendicular to the trigonal axis as shown in Figure 2.1. The superscripts (1) and (2) denote differently bonded tellurium atoms. The bonding is primarily ionic and covalent within the layers (Te $^{(1)}$—Sb and Sb—Te $^{(2)}$), and the van der Waals force dominates between the Te double layers (Te $^{(1)}$— Te $^{(1)}$) [28]. Although the crystal system of $A_2^{V}B_3^{VI}$ tetradymite semiconductors is classified as a rhombohedral Bravais lattice, these crystals are twinned together in groups of four into a larger hexagonal system. It is convenient to denote the crystal orientation in the hexagonal representation since the growth direction of the five atomic layer lamella is along the c-axis of a hexagonal structure. (In this thesis, the Bravais-Miller index which has 4 numbers (h k i l) may be used. The indices, h, k and l are identical to the Miller index and $i = -h-k$.) Fig. 2.2 shows the crystal structure of Sb_2Te_3 in the hexagonal representation. In a unit cell under the hexagonal representation, the lattice constant along the c-axis is much larger than the lattice constant along a-axis in tetradymite semiconductors. This big difference in the lattice constants along different directions

results in a highly anisotropic crystal structure. For Sb_2Te_3, the lattice constants are a=4.25 Å and c=30.30 Å. In Bi_2Te_3, the constants are a= 4.38 Å and c= 30.45 Å.

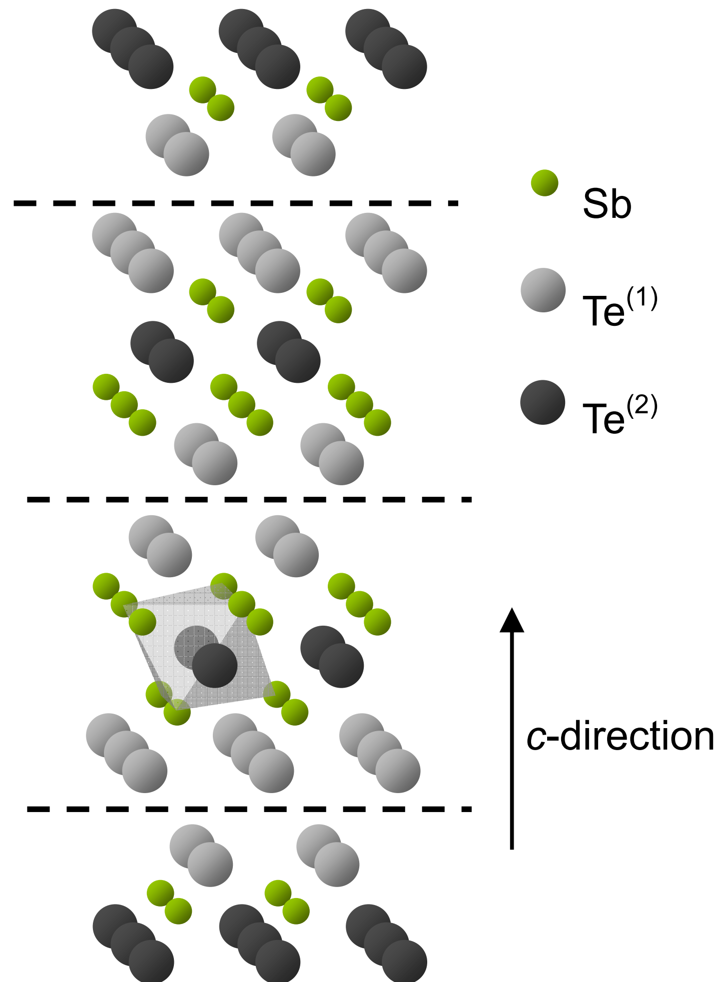

Figure 2.1 Atomic layers in the Sb_2Te_3 crystal structure. Dashed lines indicate van der Waals gaps separating five-atomic layer lamella. The octahedral coordination is highlighted for a $Te^{(2)}$ atom.

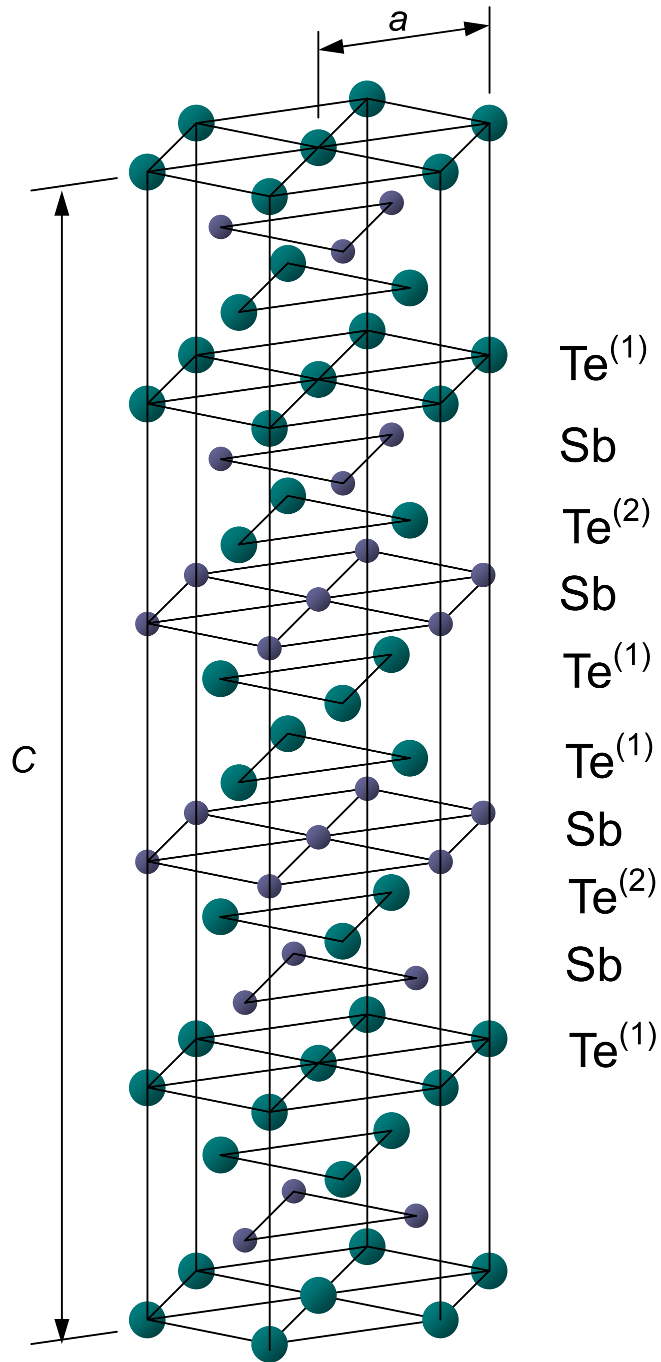

Figure 2.2 The unit cell of Sb_2Te_3 crystal under the hexagonal representation.

2.3 Electrical Properties of Sb_2Te_3 and Bi_2Te_3 Tetradymite-Type Semiconductors

2.3.1 Semiconducting Properties of Sb_2Te_3 and Bi_2Te_3

Sb_2Te_3 and Bi_2Te_3 are narrow-bandgap semiconductors with bandgap of around 0.3eV and 0.25eV, respectively [29]. Crystals of both Sb_2Te_3 and Bi_2Te_3 grown under stoichiometric conditions are prone to having antistructural defects (Sb or Bi atom in a Te position), resulting in a typical room temperature background hole concentrations in the high $10^{20}/cm^3$ range for Sb_2Te_3 and the high $10^{19}/cm^3$ range for Bi_2Te_3. The difference in the carrier densities is related to the higher polarity of the Bi-Te bond than that of the Sb-Te bond. These high hole concentrations result in a weakly degenerate electron gas. Because of the intrinsic concentration due to the high density of defects and the weakly degenerate electron states, Sb_2Te_3 and Bi_2Te_3 crystals cannot be used as semi-insulating substrates for the homoepitaxial growth. For the convenience of electric property measurement, a proper insulating substrate should be used for Sb_2Te_3 and Bi_2Te_3 thin film growth. Although the intrinsic carrier concentration is high, a wide range of carrier densities can still be achieved by impurity doping. For instance indium suppresses the concentration of holes while tin enhances it. Changing the polarity of the bond is also a way to alter the carrier concentration; as an example, stoichiometric conditions of Bi_2Se_3 growth result in an *n*-type semiconductor.

2.4 Magnetic Properties of Bulk TM-Doped Tetradymite-Type Semiconductors

2.4.1 Discovery of Ferromagnetism in Transition Metal-Doped Tetradymite-Type Semiconductors

The interest in the research on transition metal-doped, tetradymite-type semiconductors was stimulated by our discovery of low temperature ferromagnetism in single crystals of layered, narrow bandgap semiconductor Sb_2Te_3 doped with very small concentration of vanadium in 2003 [26]. Independently, an observation of low temperature ferromagnetism in the related tetradymite-type semiconductor, Bi_2Te_3 with Fe-doping was reported by a Russian group [27].

2.4.2 The Role of Transition Metals in Tetradymite Structure

In addition to the exciting discovery of ferromagnetism in vanadium-doped Sb_2Te_3 and iron-doped Bi_2Te_3, it was found that crystalline materials containing transition metal atoms exhibit a large variety of physical properties and extremely diverse magnetic properties primarily due to the localized nature of the *d*-electrons[30]. For example, transition-metal oxides show many fascinating phenomena such as "colossal magnetoresistance" behavior. Transition-metal telluride may have similar, intriguing physical properties due to the spin-orbit interaction which might also yield novel and diverse magnetic behaviors.

In order to understand the origin of ferromagnetism in DMS, it is imperative to clarify the electron configuration of the transition metal ion in the lattice where it resides and the hybridizations upon the ion. This is particularly important for

transition metal ions such as vanadium since they are known to have several valence states depending on the lattice environment due to the complex 3*d* and 4*s* outer shells. The transition metal typically substitutes on the Sb ($5s^2 5p^3$) or Bi ($6s^2 6p^3$) sub-lattice sites and should supply 3 electrons for bonding. In the case of bulk $Sb_{2-x}V_xTe_3$ crystals, based on magnetic and transport measurement, the spin of vanadium ($3d^3 3s^2$) is estimated as S=1 corresponding to the V^{3+} ion. In the picture based on *ab initio* band structure and total energy calculations, the spin configuration is described as a triple degenerate t_{2g} state and a double degenerate e_g state ($(t_{2g})^3(e_g)^2$). Similarly, favored ions such as Cr^{3+} ($3d^5$), Mn^{2+} ($3d^5$) in the crystals of Sb_2Te_3 and Bi_2Te_3 could possibly hold high spin configurations of S=3/2 and 5/2, respectively.

2.4.3 Ionic Radius of Transition Metals

The information concerning the radius of transition metal ions with various valence states gives some useful clues how to predict the possible bonding states and spin configurations of these transition metals ions in the crystals of Sb_2Te_3 and Bi_2Te_3. The impurity ion usually has a tendency to substitute for a host ion with a similar ionic radius. Otherwise, the large discrepancy in ionic radii would create lattice vacancies or large strains that could even destroy the crystal structure. Table 2.1 shows a list of ionic radii for some transition metal ions. The ionic radii of the host ions, Sb^{3+}, Bi^{3+}, and Te^{2-} are also included in the table for comparison. With one more electron in the outer shell, the ionic radii of these TM^{2+} ions are larger than those of TM^{3+} and closer to the radii of Sb^{3+} and Bi^{3+}. If only considering the similarity of ionic radii, TM^{2+} is more likely to substitute at the site of Sb^{3+} or Bi^{3+} in the crystal matrix and give one extra hole thus resulting in a *p*-type structure. If it is TM^{3+} that substitutes Sb^{3+} or Bi^{3+}, the doping level is left unchanged. By comparing the lattice

constants and doping levels between transition metal-doped and undoped samples, the nature of the transition metal ions can be determined.

Table 2.1 A list of radii of various transition metal ions and Sb^{3+}, Bi^{3+}, and Te^{2-} [31].

Ion	Coordination	Spin State		Radius (pm)	
Sb^{3+}	VI			76	
Bi^{3+}	VI			103	
Te^{2-}	VI			221	
V^{2+}	VI			79	
V^{3+}	VI			64	
V^{4+}	VI			58	
V^{5+}	VI			54	
Cr^{2+}	VI	Low	High	73	80
Cr^{3+}	VI			61.5	
Cr^{4+}	VI			55	
Cr^{5+}	VI			49	
Mn^{2+}	VI	Low	High	67	83
Mn^{3+}	VI	Low	High	58	64.5
Fe^{2+}	VI	Low	High	61	78
Fe^{3+}	VI	Low	High	55	64.5

2.4.4 Solubility Limit of TMs in Sb_2Te_3 and Bi_2Te_3

It was exciting to discover that robust ferromagnetism was induced by a small amount of transition metal doping in a bulk crystal sample prepared by a conventional equilibrium growth method. However, based on the experience with equilibrium crystal growth, the tetradymite-type structure can only dissolve transition metal impurities in a very limited quantity, usually at a level of 1% atomic composition (atomic precent, at.%). The solubility limit of vanadium in Sb_2Te_3 for equilibrium growth of bulk crystals was found to be around 3-4 at.%. Attempts to introduce larger

amounts of vanadium into Sb_2Te_3 resulted in phase segregation.

2.5 Low-Temperature MBE Non-equilibrium Crystal Growth

Solubility limitation is also a problem for bulk crystal growth of Mn-doped GaAs. In order to overcome the doping limit, non-equilibrium growth employing low temperature MBE had been used and successfully incorporated large doping levels of Mn in GaAs (up to ~10%) while maintaining a single crystal form. Following this approach, we anticipated that larger quantities of transition metals like vanadium, chromium or iron could be doped into single crystal tetradymite-type semiconductors, provided they were prepared as thin films by non-equilibrium LT-MBE growth.

2.6 Summary

The confirmation of the ferromagnetic state at low temperature in transition metal doped tetradymite-type semiconductors and the observation of the diverse magnetic properties induced by transition metals in crystal materials stimulated further extended investigations in the field of diluted magnetic tetradymite-type semiconductors. In order to study the TM doping-level dependent ferromagnetism and achieve high Curie temperatures, a high doping level is required. However, the traditional near-equilibrium crystal growth process such as the Bridgman growth severely limits the solubility. In the bulk Sb_2Te_3 matrix, the solubility of transition metals is typically on the order of 1 atomic %. Low-temperature molecular-beam epitaxy (MBE) growth overcomes the low TM solubility problem and provides a means of greatly increasing the transition metal doping concentration. Using this technique, we are able to prepare high quality epitaxial films of Sb_2Te_3 doped with a wide range of vanadium and chromium impurities.

Chapter 3
Experimental Methods

3.1 Introduction

In this chapter, the experimental methods for the study of transition metal-doped tetradymite-type semiconductors are described in detail. As discussed in the previous chapter, LT-MBE system is required for the study in order to achieve higher transition metal doping. The first part of this chapter focuses on how to prepare a thin film sample. The specifications of the important components in a custom designed MBE system will be introduced to offer a general view on the abilities and restrictions of the MBE system due to the hardware limitation. Based on the knowledge of the hardware configuration, a standard sample preparation procedure is described that meets the goal of high quality epitaxial thin film growth. The procedure includes optimal tuning of growth parameters and other crucial issues relevant to the quality of thin films such as substrate properties and pre-growth cleaning. In the second part, a variety of techniques used for characterization of thin film samples will be introduced. For crystal structure studies, *in situ* RHEED and *ex situ* X-ray diffraction have been used while Electron-beam Microprobe analysis (EMPA) and X-ray Photoelectron Spectroscopy (XPS) have been used for elemental composition (stoichiometry), and chemical or electronic state determination. Electric and magnetic properties of the samples in this thesis were mainly measured by a Quantum Design

Magnetic Property Measurement System (MPMS) that is instrumented for wide range of magnetic measurements as well as for magneto-transport studies.

3.2 Molecular Beam Epitaxy

The key piece of instrumentation for the research is a deposition system allowing compound semiconductor epitaxial thin film growth. A research-oriented MBE system that uses commercially available hardware pieces was designed and assembled to achieve controllable, high-precision crystal growth and meet the research requirement. Figure 3.1 is a schematic drawing of the custom designed MBE system showing some of the important parts including a growth chamber, high vacuum pumps, valves, material source ports etc. The specifications and functions of the crucial parts will be described in detail in the following sections.

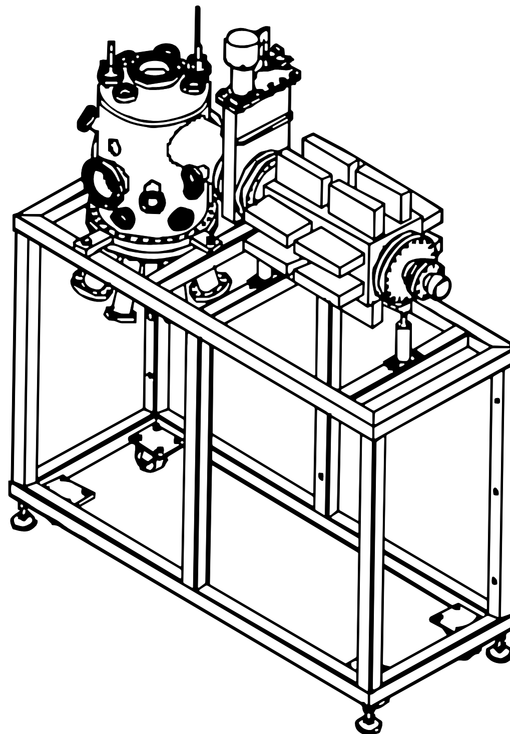

Figure 3.1 Our custom designed MBE thin film deposition system.

3.2.1 The Configuration of the Custom Designed MBE System

3.2.1.1 Growth Chamber

The growth chamber is a 16” diameter by 22” high bell jar constructed of 304 stainless steel with all metal seals. The lower part of the chamber is a 19” O.D. bolt type source flange with four effusion cell ports, two e-gun source ports and an LN_2 cryoshroud. The surface of the chamber has been electro-polished for a smooth UHV surface and the entire system is fully cryoshrouded. Fig. 3.2 is a schematic of the growth chamber. Among the important items are:

- Four 1.38” dia. source viewports, one 1.38” dia. sample viewport, one 3.88” dia. sample viewport with a shutter, and one 5.38” dia. RHEED screen viewport with a shutter.
- Two 4.5” dia. flanged ports for miniature e-Gun evaporators.
- Four 2.75” flanged ports for effusion cells with electro-pneumatically actuated source shutters.
- One manually actuated sample shutter.

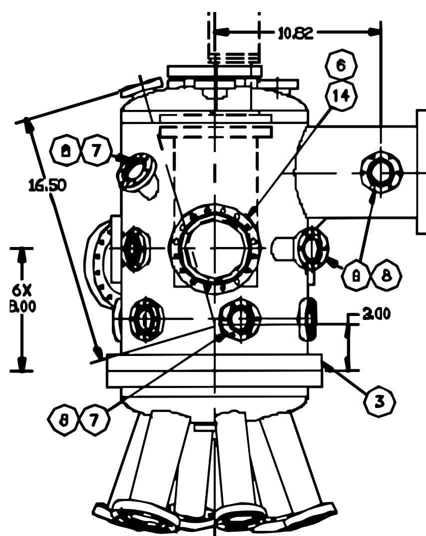

Figure 3.2 A schematic of the growth chamber with various ports marked.

3.2.1.2 Load-Lock System

The loading chamber is constructed of 304 stainless steel with all metal seals except for Viton sealed quick access door for sample loading. A rack and pinion linear feedthrough (RPL) is used with a sample transfer fork for up to 1" wafer size substrates.

3.2.1.3 Pumping System

The main chamber is pumped by a Thermionics COV-2000 ion pump (400 l/sec ion pump with LN_2 cryoshroud and titanium sublimation pump) which is isolated from the main chamber via a manually actuated 10 inch gate valve with a metal sealed bonnet.

Rough pumping of the system is provided via a Varian TV-301 turbomolecular pump together with a Varian SH-100 dry scroll vacuum pump. The main chamber is isolated from the loadlock chamber by an 8 inch gate valve.

A small appendage ion pump assembly (2 l/sec) is installed at the differentially-pumped rotary stage to ensure the ultra high vacuum condition can be maintained when the sample is rotated for RHEED inspection.

Two ion gauges and two thermocouple gauges are used for monitoring pressure in the MBE system. For high-vacuum detection, one ion gauge is installed in the growth chamber and the other one is in the loading chamber. The thermocouple gauges are used for monitoring the operation of the turbo pump and the scroll pump. One thermocouple gauge is installed in the roughing part near the exhaust port of the turbo pump, and the other is located on the differentially pumped rotary stage.

3.2.1.4 Sample Handling

A standard Thermionic FM series manipulator is used with the following specifications:

- 2” Z travel, 1.88” I.D. bellows
- Differentially pumped rotary stage (model No. RNN-600/FA)
- Custom gearbox and drive, sample holder with 1” sample holder with radiant heater capable of 1,000^{o}C operation

3.2.1.5 Effusion Cells and e-Beam Evaporator

Antimony, bismuth and tellurium are all high vapor pressure materials, and low temperature effusion cells are ideal for their deposition. We use three such cells, one each for deposition of bismuth, antimony and tellurium.

A miniature electron beam evaporator is usually employed to provide a vapor stream from materials commonly difficult to evaporate with standard thermal techniques. A miniature e-beam evaporator QUAD-EV-C from Mantis deposition LTD., allowing independent co-evaporation of up to four materials is used for depositing high melting point materials. Since each material uses an independent high-voltage connection, the evaporator will still function if there is a short-circuit due to accidental overheating of material in one of the pockets.

3.2.1.6 RHEED System

A Staib Instrument 20keV RHEED gun and power supply with a 5.68” diameter phosphor screen and screen shutter is utilized. A kSA 400 RHEED analyzing

system from k-Space associates, Inc., facilitates *in situ* surface analysis. The working principle and analysis methods for *in situ* surface morphology monitoring will be discussed in another section.

3.3 Standard Procedure for Sample Preparation

As an initial step, the growth of pure Bi_2Te_3 and Sb_2Te_3 single crystalline films of high quality should be demonstrated prior to attempting doping with TM. Based on this successful initial step, one then may proceed with establishing high doping concentration of transition metals consistent with good crystalline quality of the films. This is achieved by fine tuning of the growth conditions such as source flux rate, substrate temperature, and growth pressure. In addition to tuning these basic growth parameters, several crucial procedures had to be developed to ensure the high quality of our thin film samples. These include the choice of a substrate, pre-growth substrate cleaning, and post annealing.

3.3.1 Growth Parameters

In order to obtain a quality thin film, one must establish ideal growth parameters for the MBE epitaxial growth. These parameters include, but are not limited to, background and growth pressure, growth temperature (*i.e.* substrate temperature during the growth), deposition rates and flux ratio. Based on prior experience, the ideal growth temperature for growing an epitaxial layer is usually close to two-thirds of the melting temperature of that material. For example, the melting point of Sb_2Te_3 is around 895 Kevin, so the ideal growth temperature should be around 597 Kevin (326°C). Given a low growth temperature, atoms do not have enough kinetic energy to move around and find the best place where to attach, and

this results in a higher defect density. A low growth temperature usually produces a polycrystalline or amorphous layer. On the other hand, if the growth temperature is set too high, the growth behavior would be more like an equilibrium growth and the MBE technique would lose the advantages of its non-equilibrium nature; thus phase segregation and low solubility would again be problems. Flux ratio is directly related to the stoichiometry of the epitaxial layer. Although the atomic ratio of Sb_2Te_3 and Bi_2Te_3 is 2:3, the optimal flux ratio for growing Sb_2Te_3 and Bi_2Te_3 are around 1:3. This tellurium rich flux ratio is likely the consequence of a lower sticking coefficient of tellurium. Under high vacuum conditions, slower deposition rates always result in better epitaxial quality; however, if the pressure is higher during the growth, a higher deposition rate is preferred to reduce the defect density. In our MBE system, the typical growth pressure is around $2x10^{-9}$ Torr and the typical deposition rate is around 1 Å/sec.

3.3.1.1 Pressure Detection

As mentioned earlier, thermocouple gauges are used in the system for pressure monitoring in the range from 10^{-3} Torr to 1 Torr while Bayard-Alpert ion gauges are used in the high vacuum range. The standard B-A gauge measures down to 1×10^{-9} Torr. It does not go lower because primary electrons generate soft X-rays when they hit the grid. An X-ray hitting the ion collector electrode releases a photoelectron, which is indistinguishable from positive ions arriving there. Below 1×10^{-9} Torr, photoelectron emission is a large enough fraction of the ion current to distort the pressure reading. Although in the ultra high vacuum range the pressure reading from the B-A gauges can not accurately reflect the actual pressure, the inaccurate readings cause no problem for the growth of high quality epitaxial thin films.

3.3.2 Substrate Consideration

3.3.2.1 Substrate Properties

The choice of a substrate is very crucial for epitaxial crystal growth. Several kinds of substrates have been tried and tested in the past for both Sb_2Te_3 and Bi_2Te_3 thin film MBE growth, including Corning glass, silicon wafers [32], GaAs, MgO, sapphire, BaF_2, and mica.

We started with Corning glasses as substrates to make test runs and calibration for our home-built MBE system on account of their low-cost. Since these glasses are not crystalline, we of course never got good crystalline Sb_2Te_3 and Bi_2Te_3 thin films on these substrates even though a lot of different growth conditions had been tried.

Sapphire is one of the most common substrates and extensively used for hexagonal structure crystal growth, such as GaN. As an insulator, sapphire also offers the convenience for electric property measurement. Successful single crystal Sb_2Te_3 and Bi_2Te_3 growth using MBE and MOCVD technique on sapphire substrate had been reported previously by some research groups [33, 34]. Our research made use of their experiences with sapphire. Sapphire is one of the hardest materials beside diamond. Compared to sapphire, the hardness of Sb_2Te_3 and Bi_2Te_3 is much lower. This big hardness difference brings a lot of trouble in preparing cross-section TEM samples.

BaF_2 has a simple cubic crystalline structure with a lattice constant 6.46 Å; therefore, on its (111) plane three nearby points form an equilateral triangle with sides of length of 8.62 Å . This unique length in a special hexagonal lattice or equilateral triangular lattice arrangement on BaF_2 (111) plan is very close to twice the *c*-plane Sb_2Te_3 lattice constant which makes BaF_2 a very promising lattice matching substrate

for Sb_2Te_3. However, BaF_2 is expensive and not easy to obtain, and is also soft and fragile. These drawbacks considerably overshadow its advantage of the lattice matching.

Mica is cheap and easily cut into desired shapes. Because crystalline mica forms in flat layered sheets, a very smooth and clean surface can be easily obtained via simple cleaving (RMS roughness of < 1 nm over one square micron is easily achieved). Mica is an insulator so that there is no interference while measuring the transport property of a conducting thin film grown on mica. These advantages make mica a popular substrate material. However, a fair amount of mica is of poor quality for epitaxial growth. In addition, the brittle nature and trapping of solvent in the substrate cause the difficulties in handling this substrate.

3.3.2.2 Substrate Cleaning

Substrate cleaning is one of the most important steps for our thin film growth since none of the substrates used was epi-ready. Without proper cleaning procedures, high quality films cannot be obtained.

Prior to growth, all substrates were degreased by hot bathing in acetone for five minutes and then in isopropanol (IPA) for five minutes. For sapphire substrates, we used a modification of the RCA-1 process [35] but used 25% phosphoric acid instead of ammonium hydroxide and hydrogen peroxide mixture. For Pyrex and glass substrates, a buffer HF solution was used. Right before loading into the vacuum chamber, a simple IPA vapor drying process is applied to the substrates to avoid the formation of water marks.

3.3.2.3 *In situ* Substrate Cleaning

After being loaded into the growth chamber, substrates are heated to a high temperature to remove any possible residual contaminations. Sapphire substrates were heated up to 650°C for at least 4 hours and then further to 850°C for 15 minutes. A clear RHEED pattern can usually be obtained after the *in situ* substrate cleaning indicating a perfect and clean substrate surface. Otherwise, substrates will be taken out of the growth chamber and the RCA chemical wet etching procedure is repeated.

3.3.3 Metal Masks and Sample Cutting

Our thin film samples under test are required to have some special shapes and sizes to fit in different measurement apparatus. The typical substrate in our experiment is a square of 10mm side. A diamond pen is used to cut and shape substrates such as GaAs, BaF_2, MgO, mica and silicon. For harder substrates such as sapphire, a low speed diamond wheel saw (South Bay Technology Model 650) is utilized. However, the cutting fluid with sawdust during the saw cutting will contaminate substrate surface or thin film epilayers. To protect the quality of our samples and substrates from possible cutting contamination, we spin a thin layer of PMMA polymer (PMMA in Chlorobenzene) on the substrate or thin film surface prior to cutting. The layer of PMMA polymer is then removed by acetone solvent and IPA vapor drying process as mentioned in section 3.3.2.2.

The cutting procedure can be done either before or after a thin film epilayer has been grown. Both approaches have their advantages and drawbacks. The prior growth cutting avoids damaging the epilayers; moreover these substrates are usually more robust than the delicate epilayers so that a more aggressive wafer cleaning

procedure can be carried out on the substrates to remove the polymer layer and sawdust and leave an ideal surface for epitaxial thin film growth. A specially designed metal mask can be used for these small substrates to define some ideal deposition patterns especially for sample intended for Hall measurements. However, the small pieces of substrates plus the extra thickness from the metal mask cause us problems during RHEED observations. No such difficulties arise and a clear *in situ* RHEED pattern can easily be seen if we grow the epilayer on a larger substrate. In that case much more care must be exercised during the after growth cutting and the wafer cleaning after cutting. Peeling off or detachment of the epilayer from the substrate happens occasionally when careless wafer cutting and cleaning are performed.

As shown in Fig. 3.3, a special sample holder has been designed to hold not only a large piece of substrate but also two small ones for Hall effect and resistance measurements. The dashed shadow areas indicate three shallow grooved regions that hold the substrates. Two different deposition patterns defined by two kinds of metal masks are shown in Fig. 3.4.

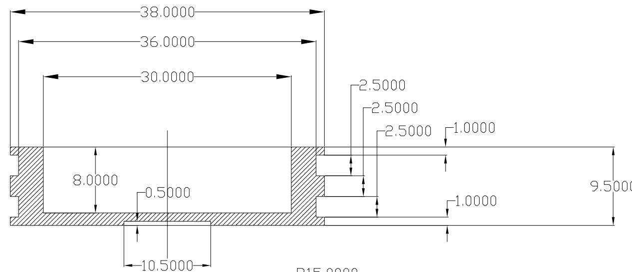

Uher's Lab MBE Sample Holder
Material: Stainless Steel
Unit: mm
Quantity: 1
Account No.:045825
ROOM: SB214
TEL: 33512
Designer: Yi-Jiunn Chien

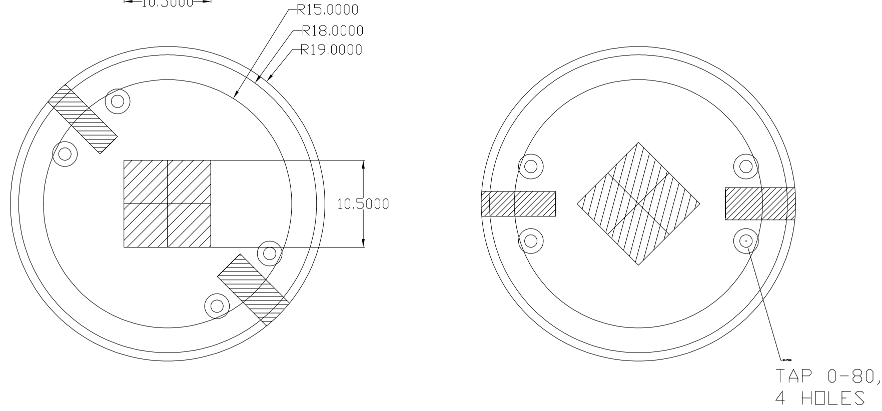

Figure 3.3 The schematic picture of the sample holder from both the side view and the top view.

Uher's Lab
Hall Measurement Metal Masks
Unit: mm
Designer: Yi-Jiunn Chien
Material: Molybdenum
Room: SB214 TEL:33512
Account: 045825

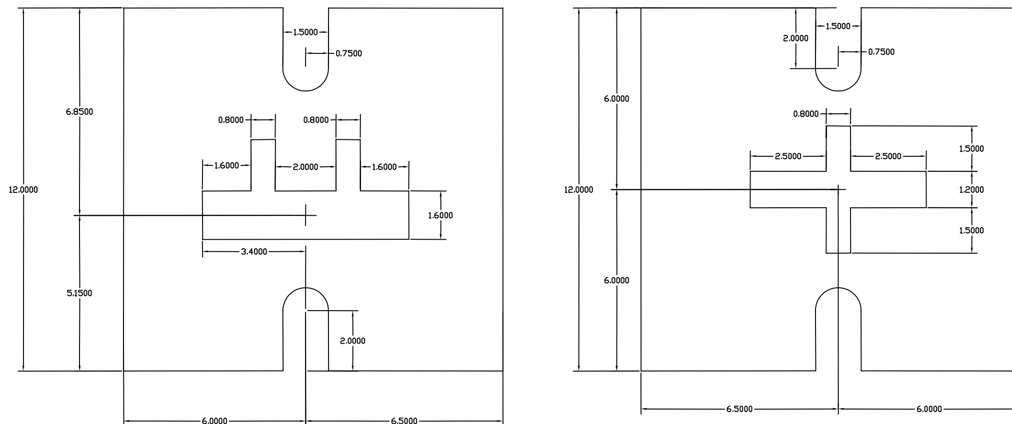

Figure 3.4 Two metal masks designed for Hall effect and transport measurements.

3.4 Crystal Structural Determination

3.4.1 Reflective High Energy Electron Diffraction (RHEED)

Reflective high energy electron diffraction (RHEED) uses high energy electrons (typically 5-100keV) and low incidence angles (<5°). The higher energy sharpens the diffraction patterns, while the lower angle restrains electrons from penetrating more than a few atomic layers into the crystal. Consequently RHEED patterns represent the symmetry in surface morphology and not the bulk crystal; therefore, changes in periodicity in the plane of incidence cannot be seen.

During the growth of epilayers, several interesting features can be found in a RHEED pattern, depending on the growth conditions. These include, Kikuchi lines [36], Laue circles [37], streak lines [38,39,40,41], and chevron patterns [42]. As shown in Fig. 3.5, an ideal RHEED pattern from a smooth crystal surface consists of well defined streaks which follow the shape of Laue circles. Chevron patterns are related to the formation of dots or islands [43], while streak lines reflect the surface morphology or reconstruction structures. A RHEED pattern formation can be understood by the Ewald Sphere construction. Two-dimensional lattice dots in the real space become lattice rods in the reciprocal lattice (which are perpendicular to the surface). Reciprocal lattice rods have a non-zero width and so the observed pattern is a streak. Figure 3.6 is an example of RHHED pattern formation according to the Ewald sphere construction. Since these RHEED streaks form according to the diffraction condition given by Bragg's Law, the lattice constant can be obtained by knowing the spacing between the streaks.

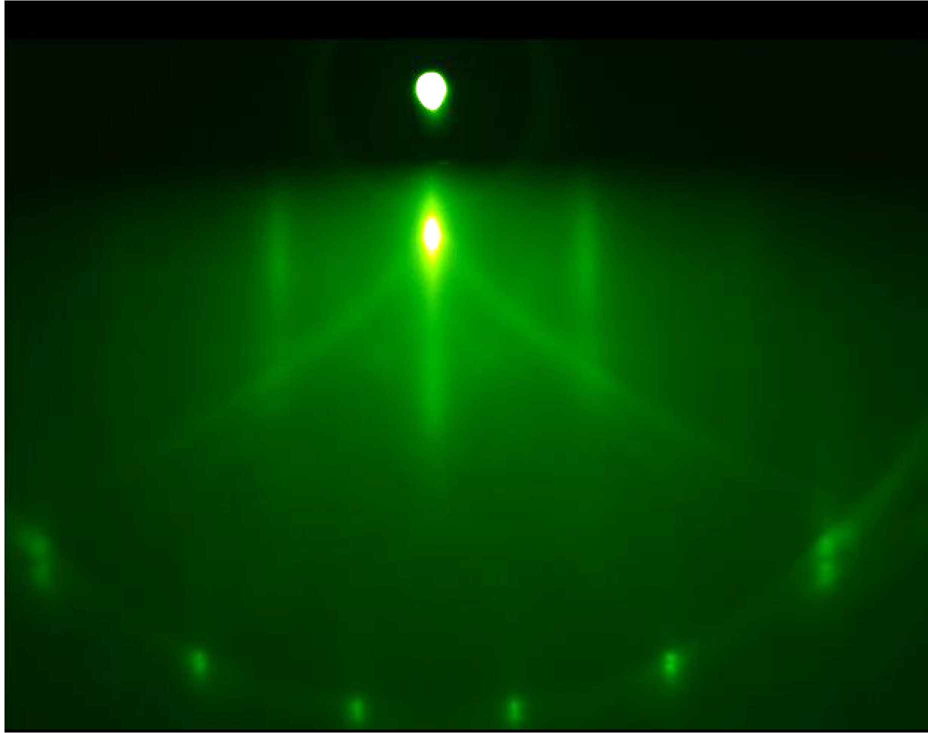

Figure 3.5 A RHEED pattern observed on clear sapphire (0001) plane.

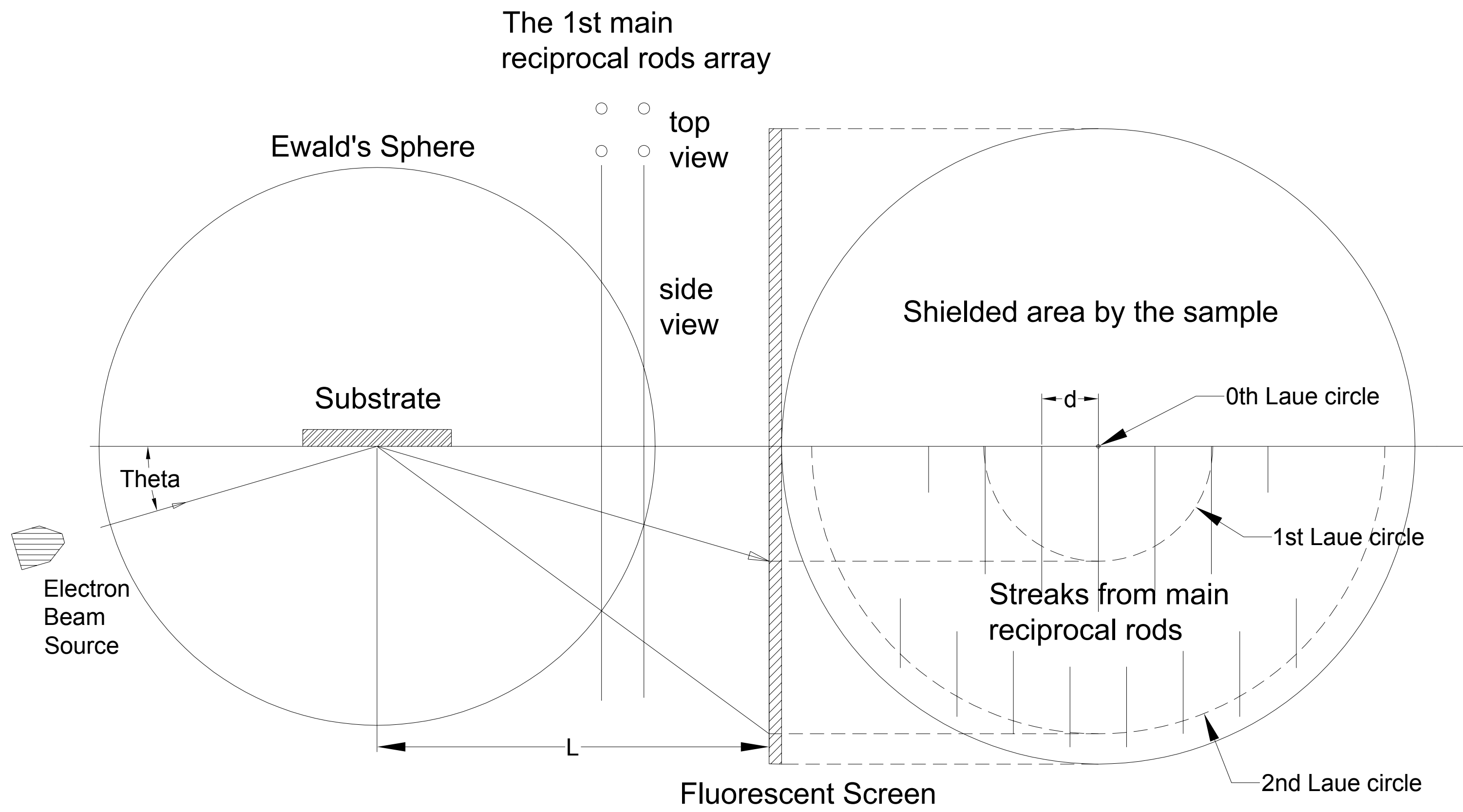

Figure 3.6 The origin of streaks and Laue circles according to the Ewald's sphere construction.

The RHEED system is very useful in MBE growth facilities for real-time analysis and monitoring of crystal growth since the formation of RHEED patterns is extremely sensitive to the surface roughness, down to monolayer thickness. In order to orient thin film crystals and observe streak patterns, RHEED requires at least a partial rotation of the sample. The rotating sample holder in our MBE system fulfills this requirement.

3.4.2 X-Ray Scattering Techniques

X-ray scattering is an excellent electromagnetic method for determining structures of molecules since their wavelengths (~1Å) are on the scale of a lattice constant. By monitoring the scattering of x-rays in solids, one can get useful information from these scatterers such as their crystallography and their inner shell electron states. X-ray diffraction is a form of elastic scattering which is useful in determining the distribution of scatterers within the matter. In contrast, inelastic scattering is useful for probing excitations of matter. When the energy and angle of the inelastically scattered x-rays are monitored, scattering techniques can be used to probe the electronic band structure of materials. X-ray Photoelectron Spectroscopy (XPS) is a case of inelastic scattering since bounded electrons gained energy from x-ray and emitted. It provides a possible way to determine the valance states of transition metals in tetradymite-type semiconductors.

3.4.2.1 X-Ray Diffraction

X-ray diffraction techniques are based on the elastic scattering of X-rays from structures that have long range order. Since the periodic structure along the growth direction cannot be examined by RHEED, X-ray diffraction is used to further explore

the crystallography of our thin film samples. In principle, X-ray diffraction can be used to solve the complete structure of crystalline materials. However, in the case of thin film crystallography, small angle X-ray scattering is preferable to probing structure in the nanometer to micrometer range by measuring scattering intensity at scattering angles 2θ close to 0°. In this work, a conventional powder diffractometers with the Bragg-Brentano focusing geometry is used to characterize epitaxial layers. Although diffractometers of this type can achieve high resolution via a slit aperture placed in front of the detector, mosaic misorientation effects cannot be detected. Actually, powder diffractometers are designed to cancel the misorientation effects, especially for structural analysis of powdered samples. It was reported that the FWHM observed for such diffractometers is not a measure of mosaic spread, but instead is a measure of the size of the mosaic pieces and of the strain within them [44,45].

3.4.2.2 X-Ray Photoelectron Spectroscopy (XPS)

X-ray Photoelectron Spectroscopy (XPS) is a process using inelastic X-ray scattering where X-ray photons cause emission of core electrons. XPS spectra are obtained by irradiating a material with a beam of X-rays while simultaneously measuring the kinetic energy (KE) and number of electrons that escape from the top 1 to 10 nm of the material being analyzed.

Because the energy of a particular X-ray wavelength is a known quantity, we can determine the electron binding energy (BE) of each of the emitted electrons by using an equation that is based on the work of Ernest Rutherford (1914):

$$E_{\mathrm{binding}} = E_{\mathrm{photon}} - E_{\mathrm{kinetic}} - \Phi$$

where $E_{binding}$ is the energy of the electron emitted from one electron configuration within the atom, E_{photon} is the energy of the X-ray photons being used, $E_{kinetic}$ is the kinetic energy of the emitted electron as measured by the instrument and Φ is the work function of the spectrometer. Transition metal ions with different valence states have different binding energies since they have different bonding in the states. The bonding states can be determined by analyzing the binding energies.

3.4.3 Electron Probe X-Ray Microanalyzer (EPMA)

The electron microprobe is an analytical tool used to non-destructively determine the chemical composition of small volumes of solid materials. The basic process of EPMA can be described as the following. Electrons are produced from a tungsten filament cathode and accelerated by an anode plate to 10 to 30 KeV. These high energy electrons are focused by a series of magnetic lenses and apertures. The resulting approximately 1 micrometer diameter electron beam can be used to generate X-rays characteristic of the elements present within a sample volumes around 1 micrometer across. Then the characteristic X-rays can be used for chemical analysis. Specific X-ray wavelengths are selected and counted, either by wavelength dispersive spectrometry (WDS) or energy dispersive X-ray spectroscopy (EDS). By comparing the intensities of characteristic X-rays from the material of the sample under test with intensities from standard samples, chemical compositions can be quantitatively determined with a precision levels as low as 100 ppm. In this thesis, EPMA is the method for determining the stoichiometry of those tetradymite-type thin film samples.

3.4.4 Thin Film Thickness

Thin film thickness is a very important parameter. Since a number of physical

parameters such as carrier density, resistivity, magnetization etc. is related to the thickness, a precise value of thickness should be obtained. Several methods have been used for thickness determination. A crystal thickness monitor mounted in our MBE system provides real time deposition rate and thickness monitoring. However, the thickness of the deposition layer on the crystal monitor is different from the thickness on the substrate due to the different sticking coefficients and temperatures. More precise and direct measurements of thickness are carried out on a Dektak surface profiler and Atomic Force Microscope (AFM). The thickness readings from the crystal monitor were found to have a linear relation to the values obtained by Dektak and AFM measurement. If the same growth parameters (substrate temperature, flux ratio) are followed, the simple relation can be used to calibrate the thickness monitor, then giving a reliable and consistent real time thickness reading. Given a known density, EPMS also can provide information on thin film thickness. Since most of the thin films prepared by MBE technique are homogenous, the thickness values from this method are consistent with the results from the Dektak and AFM.

3.5 Electrical and Magnetic Characterization

3.5.1 Magnetic Property Measurement System (MPMS)

Most of the measurements of electronic and magnetic properties of the thin films are done on a Quantum Design Magnetic Property Measurement System, MPMS XL. The MPMS is basically a cryogenic probe which integrates a superconducting magnet with a SQUID detection system and a temperature controller in a specially designed Dewar. These sophisticated configurations provide rapid precision measurements over a temperature range of 1.9 to 400 Kelvin.

3.5.1.1 Background and Substrate Response Subtraction

The typical thickness of the thin films we grow is around 100 to 400 nm, which is much thinner than the 0.5mm thick substrates. Therefore, the small magnetic response of the thin film may be masked by a stronger diamagnetic response from a substrate. Thus, in order to analyze the magnetic response from the thin film, subtraction of the response from the system background and the substrate is necessary. The first step of the subtraction procedure is collecting the magnetic data generated by the background addenda and establishing its magnetic field dependence at different temperatures. The second step is to assume that all our substrates are homogenous in their magnetic property so that we can regard their measured diamagnetic response as being proportional to their mass.

3.5.2 Determination of the Ordering Temperature

The values of critical temperatures are determined experimentally from both Arrott plots and the temperature dependence of the magnetization at low magnetic field. In addition, Arrott plots are calculated in terms of mean field theory with three fitting parameters derived from the fitting of the *M*(T) curves.

3.5.2.1 Curie-Weiss Law

Above the magnetic ordering temperature, the magnetic susceptibility is well described by a Curie-Weiss law,

$$\chi = \frac{C}{T - \Theta_p} + \chi_o, \tag{11}$$

where C is the Curie constant, Θ_p is the paramagnetic Curie temperature, and χ_o is the temperature-independent diamagnetic lattice term. For a given concentration of vanadium in each sample, the magnetic state of the ions can be inferred from the Curie constant using the equation $C = N_V \mu_B^2 p_{eff}^2 / 3k_B$. Here N_V is the concentration of transition-metal atoms, μ_B is the Bohr magneton, p_{eff} is the effective Bohr magneton number given by $g[S(S+1)^{1/2}]$ with the Landé g factor (g=2) and the spin S. We are assuming complete quenching of the orbital angular momentum, which is the usual case for transition-metal ions. An abrupt change in the magnetic susceptibility occurs at the critical temperature. Below this temperature, the Curie-Weiss law is no longer valid. Therefore, by fitting the measured susceptibility data with the Curie-Weiss law, not only paramagnetic Curie temperatures can be determined, but also ferromagnetic or anti-ferromagnetic critical temperatures can be obtained. Transition-metal ions with different valence states usually have different effective Bohr magneton. Comparing the value of the effective Bohr magneton extracted from the experimental data with a theoretical one, the valence state of the transition-metal ion can be estimated.

3.5.2.2 Arrott Plot

Of all the methods of determining critical temperature of a ferromagnet, Arrott plots are perhaps the most trustworthy because the technique minimizes the contribution arising from domain rotation and magnetic anisotropy. In the case of a conventional second order ferromagnetic transition, Arrott plot should yield positive slope straight lines given that the magnetic field is high enough so that possible domain or stray field effects can not be seen. In some cases, the predictions of mean field theory do not work well for some materials; thus the conventional Arrott plots

were expanded to meet various model prediction by properly choosing the critical exponents, β and γ in the equation [46]

$$\left(\frac{H}{M}\right)^{1/\gamma} = \frac{T - T_c}{T_1} + \left(\frac{M}{M_1}\right)^{1/\beta}, \tag{12}$$

(in the mean field theory, β=0.5 and γ=1). In the equation, T_1 and M_1 are material dependent parameters. Although the low field curvatures in the Arrott plots are not ideal for critical temperature determination, it may reveal some useful information related to the spin structure. Some physical reasons for curvature have been given in ref.[47].

3.5.3 Hall Effect

The Hall effect is a conducting phenomenon involving moving charge particles in conductors under the influence of the Lorentz force. If an electric current flows through a conductor in a magnetic field, the magnetic field exerts a transverse Lorentz force on the moving charge carriers which tends to push them to one side of the conductor. A buildup of charge on the sides of the conductors will balance this magnetic influence, producing a measurable transverse voltage between the two opposite sides of the conductor. The presence of this measurable transverse voltage is called the Hall effect.

3.5.3.1 Ordinary Hall Effect

The ordinary Hall effect provides a relatively simple method for determining accurately carrier density, electrical resistivity, and the mobility of carriers in semiconductors due to its simplicity, low cost, and fast turnaround time; thus ordinary

Hall measurement is regarded as an essential characterization technique in the semiconductor industry and in research laboratories.

3.5.3.2 Anomalous Hall Effect

In ferromagnetic materials (and paramagnetic materials in a magnetic field), the Hall resistivity includes an additional contribution, known as the anomalous Hall Effect (extraordinary Hall effect or spontaneous Hall effect), which depends directly on the magnetization of the material, and is often much larger than the ordinary Hall effect. The anomalous Hall coefficient can be expressed as the following form [49],

$$\rho_{Hall}=R_0B+R_sM, \tag{13}$$

where R_0B is the term due to the ordinary Hall effect, M is magnetization of the sample under test. By finding the anomalous Hall coefficients, the magnetization can be determined. Therefore, anomalous Hall effect has been recognized as a useful tool for measuring the magnetic hysteresis M(H) loops of diluted magnetic semiconductors. Although a well-recognized phenomenon, there is still debate about its origins in the various materials. The anomalous Hall effect can be either an extrinsic (disorder-related) effect due to spin-dependent scattering of the charge carriers, or an intrinsic effect which can be described in terms of spin chirality or the Berry phase effect in the crystal momentum space.

3.5.4 Resistivity Measurement

Resistivity measurements can usually be done together with Hall measurements if proper measurement methods (such as van der Pauw technique or Hall bar with more than 2 voltage terminals) can be applied. However, the restriction

on the sample size in the MPMS cause technical difficulties in designing a Hall bar metal mask with an extra voltage terminal for resistivity measurement. Since indium ohmic contact formation and wire bonding are required to implement the measurement, a specific four terminal bar shape metal mask for resistivity measurement is used to prevent the difficulties with wire bonding. Temperature dependent resistivity measurements can be done in our MPMS, and this allows us to analyze the possible charge carrier scattering mechanisms and transport processes in the epitaxial thin films.

3.6 Summary

A detailed experimental procedure for transition metal-doped Sb_2Te_3 and Bi_2Te_3 tetradymite-type diluted magnetic semiconductors has been proposed. As mentioned in the previous chapter, most of the theoretical predictions for ferromagnetic state of DMSs are based on Bloch theory. Therefore, preparing a crystalline sample is most desired for the study in this field. MBE technique exhibits not only the non-equilibrium growth nature to enhance transition metal doping levels, but it also facilitates the layer-by-layer epitaxial growth that ensures quality crystalline samples. Thus, MBE is regarded as one of most promising methods for preparing the tetradymite-type DMS thin films.

Specific characterization methods have been described in this chapter. RHEED, X-ray diffraction are used to verify the orientation and quality of thin film crystals, while XPS and EMPA are used for detecting the chemical composition and valence states. Electric and magnetic properties of thin films are obtained by SQUID-based magnetic measurements and careful transport studies.

Chapter 4
Epitaxial Thin Films of Vanadium-Doped Antimony Telluride

4.1 Introduction

The experimental method proposed in the previous chapter for studying transition metal-doped tetradymite-type semiconductors has been first carried out on vanadium-doped Sb_2Te_3 epitaxial thin films. By adjusting the electron beam power on the miniature e-beam evaporator, a series of vanadium-doped Sb_2Te_3 epitaxial thin film samples with various vanadium concentrations have been prepared. As will be shown in this chapter, the non-equilibrium molecular beam epitaxy growth technique has been confirmed to be useful for solving the problem of low solubility of transition metals in the tetradymite-type semiconducting matrix. More than 10 times increase in the vanadium doping level (0.35 vs. 0.03 in mole fraction of vanadium) has been achieved, yielding a robust ferromagnetism at temperatures up to 177K. A series of samples with different content of vanadium have been prepared to explore the relations between the doping level and electric and magnetic properties of thin films.

4.2 Sample Preparation

Vanadium-doped Sb_2Te_3 epitaxial thin films were prepared on sapphire (0001) substrates by molecular beam epitaxy. Growth rates of 1.7–1.8 Å/ s were used for all

samples with a fixed flux ratio (Sb,V):Te from 1:2 to 1:3 at a substrate temperature of around 310 °C. A miniature e-beam evaporator was used for the deposition of vanadium and the Knudsen effusion cells for antimony and tellurium.

4.2.1 Growth Parameters

4.2.1.1 Deposition Rate and Flux Ratio

Deposition rates of antimony, tellurium and the transition metals were monitored on a calibrated crystal thickness monitor and the flux ratio of these deposition sources was calculated according to their deposition rates. The relations of effusion cell temperatures and deposition rates are listed in Table 4.1. The effusion cell containing Sb was set at a temperature around 512°C, resulting in a deposition rate of 0.6Å/sec on the thickness monitor. The temperature of the tellurium (Te) source was about 375 ^{o}C and yielded a deposition rate of 1.4 Å/sec. The miniature e-beam evaporator used for high melting point transition metal sources gives tunable e-beam power and its own flux monitors for controlling the deposition rates. The deposition rates here are individually measured for antimony and tellurium on the surface of the gold thin film coated on a quartz crystal at room temperature. The actual deposition rates of the epitaxial $Sb_{2-x}V_xTe_3$ layers on sapphire substrates can not be obtained directly from the thickness monitor since the adhesion coefficients will definitely change due to different temperature settings and substrate properties.

Table 4.1 Effusion cell temperatures and deposition rates of antimony and tellurium for $Sb_{2-x}V_xTe_3$ epilayer growth.

Source Material	**Effusion Cell Temperature (°C)**	**Deposition Rate (Å/sec)**
Antimony (Sb)	512	0.6
Tellurium (Te)	375	1.4

4.2.1.2 Vanadium Flux Control

The purity of the highest grade of vanadium we could obtain is 99.8%. Since vanadium tends to wet other materials such as crucibles, it is difficult to prepare it with very high purity. This crucible wetting problem forces us to use vanadium rods instead of crucibles in the miniature e-gun system. However, using vanadium rods has its own problems. Incident e-beam tends to create a molten ball on top of the rod, and this molten ball often drops down and shorts the high voltage circuit generating electron beams, thus interrupting the deposition. Whenever this situation occurs, the whole body of the evaporator should be taken out from the ultra high vacuum growth chamber for repair. The shape change at the tip of the rod also effects the electric field distribution and results in unstable deposition rates. Once the deposition rate of vanadium becomes unstable, the growth procedure has to be terminated. Although we aimed for all films of comparable thickness, the instability of vanadium flux often forced us to terminate the deposition early and thus we ended up with films of different overall thickness. If the deposition rate of antimony is 0.6 Å / s, in order to achieve a $Sb_{2-x}V_xTe_3$ sample with vanadium fraction x=0.05, the vanadium deposition rate should be 0.43 Å/ min. Table 4.2 lists the relation between the power applied to

the e-gun evaporator and vanadium deposition rates. The maximum value of relatively stable deposition rates can be obtained is around 2.5 Å/ min which in principle gives a vanadium fraction x=0.26. To have a larger vanadium fraction, smaller antimony flux can be chosen while keeping the same Sb:Te flux ratio.

Table 4.2 A list of vanadium deposition rates given by different e-beam power levels. e-beam current and chamber pressure are also listed for reference.

e-beam current (mA)	e-beam power (W)	Pressure (Torr)	Vanadium Deposition Rate (Å/ min)
2.79	26.0	1.8×10^{-9}	0.02
2.81	28.0	2.0×10^{-9}	0.33
2.81	30.0	2.2×10^{-9}	0.62
2.83	32.5	2.6×10^{-9}	2.51

4.3 Structural Characterization

4.3.1 RHEED Patterns

The reflection high-energy electron diffraction patterns indicate that the films grow with their c axis perpendicular to the plane of the substrate and streak-like diffraction attests to a near two-dimensional mode of film growth.. An example of the RHEED pattern during the growth of Sb_2Te_3 and $Sb_{1.65}V_{0.35}Te_3$ thin films is shown in Figures 4.1 to 4.3. Fig. 4.1 shows the RHEED pattern of a (0001) sapphire substrate for $[01\bar{1}0]$ incident beam. Although the pattern appears diffusive due to the charging effect on an insulator, clear Kikuchi lines can still be seen, indicating that a very smooth and clean surface of a sapphire substrate is obtained after *in situ* substrate cleaning. During the growth, the distance between the streaks (streak spacing) in the RHEED pattern increased rapidly during the initial 10 sec of film growth while spots and rings

also appear in this initial stage as shown in Fig. 4.2. The appearance of the spotty and ring patterns indicates three dimensional growth and non-ideal crystalline nature. Afterwards, the streak spacing remains essentially unchanged for the entire duration of the deposition, i.e., up to the film thickness of ~500 nm. In addition, the spotty and ring patterns gradually disappear while the streak pattern becomes even clearer after several hundred Ǻ thin film growth (Fig. 4.3). Obviously, a rapid lattice relaxation takes place within the first few atomic layers as the Sb_2Te_3 strata evolve from highly strained layers (large in-plane lattice mismatch of about 11% between sapphire and Sb_2Te_3) to the essentially bulk-like layers of Sb_2Te_3. The RHEED pattern repeats at every step of 60 degree rotation on the films, indicating that the films grow with their basal plane parallel to the substrate surface and the trigonal axis (*c*-axis) perpendicular to the substrate.

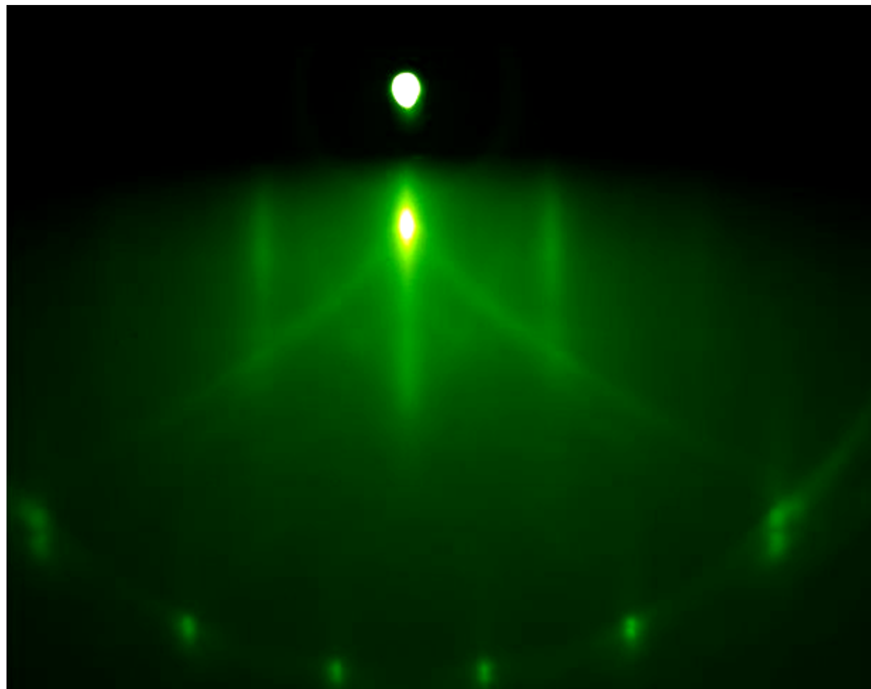

Figure 4.1 RHEED patterns of a (0001) sapphire substrate for $[0\,1\,\bar{1}\,0]$ incident beam after 30min 850°C *in situ* substrate cleaning.

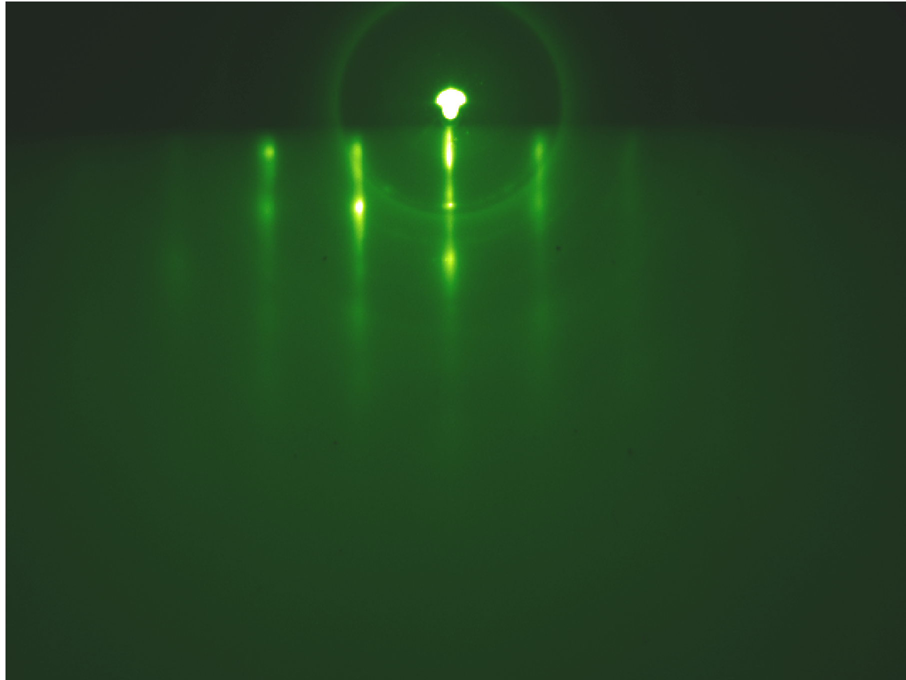

Figure 4.2 RHEED patterns observed during the first 10nm of $Sb_{2-x}V_xTe_3$ growth for $[2\bar{1}\bar{1}0]$ incident beam.

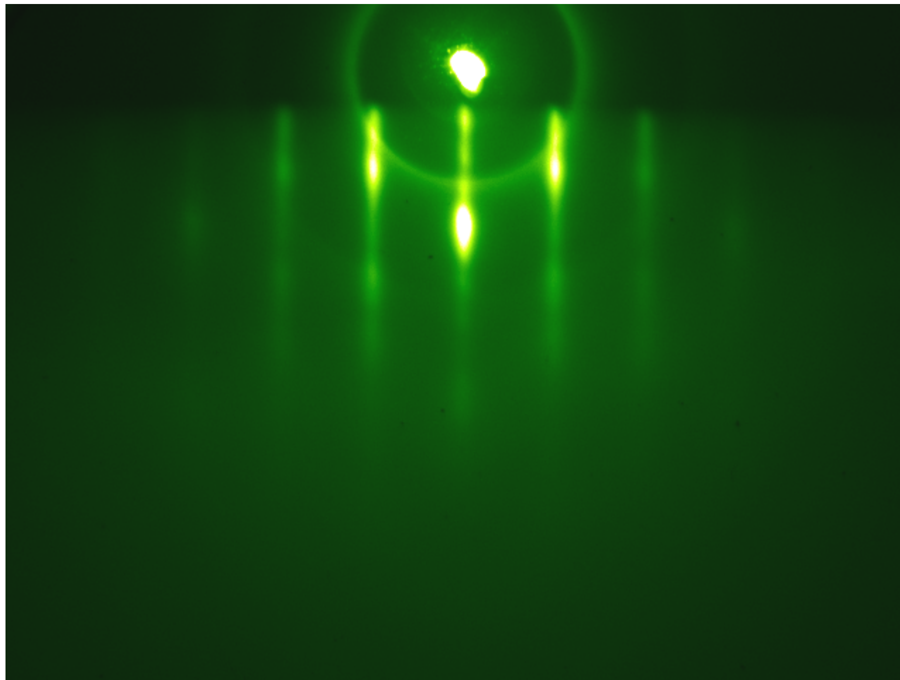

Figure 4.3 RHEED pattern observed after the first 10nm of $Sb_{2-x}V_xTe_3$ growth for $[2\bar{1}\bar{1}0]$ incident beam.

4.3.2 X-Ray Diffraction (XRD)

After being taken out of the chamber and before cutting, the thin films were analyzed by X-ray diffraction (XRD) to confirm their tetradymite-type crystal structure. Figure 4.4 shows the X-ray diffraction pattern of a bulk single crystal of Sb_2Te_3 prepared by Bridgman growth technique and of the films of $Sb_{2-x}V_xTe_3$ with x = 0, 0.15, 0.32, and 0.35. Only (00.n) peaks in the hexagonal unit cell are present, confirming that the films grow along the c-axis direction. After comparing possible X-ray characteristic diffraction peaks from pure vanadium, antimony, tellurium and their other compounds such as SbTe, $SbTe_2$ and Sb_2Te_5, no trace of any secondary phase formation was found from the XRD scans. The sapphire substrate peak is indicated in the XRD pattern of the sample with x = 0. The XRD scan of the sample with x = 0.15 is noisier than the other scans due to the small thickness (170 nm) of this particular film. Cleaner XRD patterns are obtained from the other samples since stronger diffraction intensity is given by a larger thickness. Nevertheless, precise peak positions can still be easily indicated even in the noisier X-ray diffraction spectrum. If vanadium doping causes the change in the lattice constant, a shift on the X-ray diffraction peaks should be observed. In the next section, the lattice constants of these vanadium-doped thin films will be determined from the X-ray diffraction pattern.

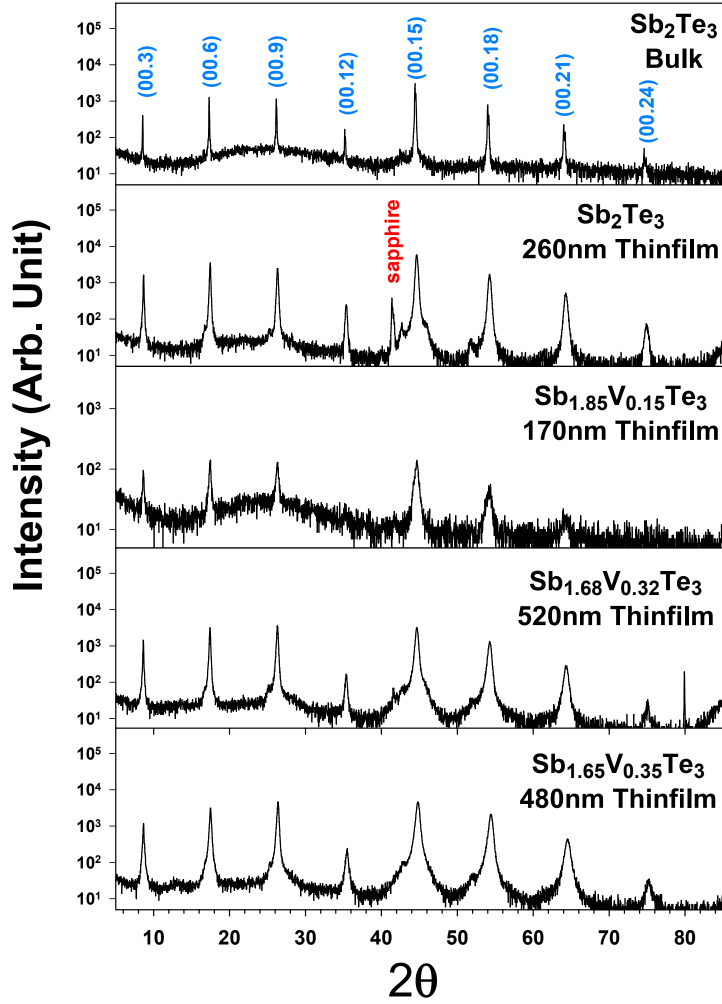

Figure 4.4 X-ray diffraction pattern from a bulk Sb_2Te_3 crystal and from $Sb_{2-x}V_xTe_3$ epitaxial thin films for x=0, 0.15, 0.32 and 0.35

In Figure 4.5 is plotted the dependence of the in-plane lattice constant *a* of $Sb_{2-x}V_xTe_3$ films as a function of vanadium concentration. These lattice constants were determined from the RHEED patterns taken during the growth and X-ray measurement. The lattice constants *a* and *c* of the films can be obtained by using the following relation:

$$\frac{1}{d_{hkl}} = \frac{2}{3}\frac{h^2 + hk + k^2}{a^2} + \frac{l^2}{c^2}, \tag{14}$$

where d_{hkl} is the distance between (h,k,l) planes. The (00.3), (00.6), (00.9), (00.12), (00.15), (00.18) and (00.21) peaks in the X-ray diffraction pattern give the values of $d_{00.l}$ (l=3, 6, 9, 12, 15, 18 and 21) which can be used for calculating the lattice constant c. The streak spacings from RHEED patterns also provide the information on d_{hkl}, thus the lattice constant a can be determined. The lattice constants a and c of the $Sb_{2-x}V_xTe_3$ thin film samples (x=0, 0.15, 0.32 and 0.35) are shown in Figure 4.5. Their unit cell volumes calculated from the lattice constants are also included in this figure. A higher vanadium doping level results in a smaller lattice constant a while this doping level dependence on lattice constant c is not as obvious. This decreasing trend on the lattice constant due to increasing doping levels may be an evidence of the participation of V^{3+} instead of V^{2+} ions in the Sb_2Te_3 matrix.

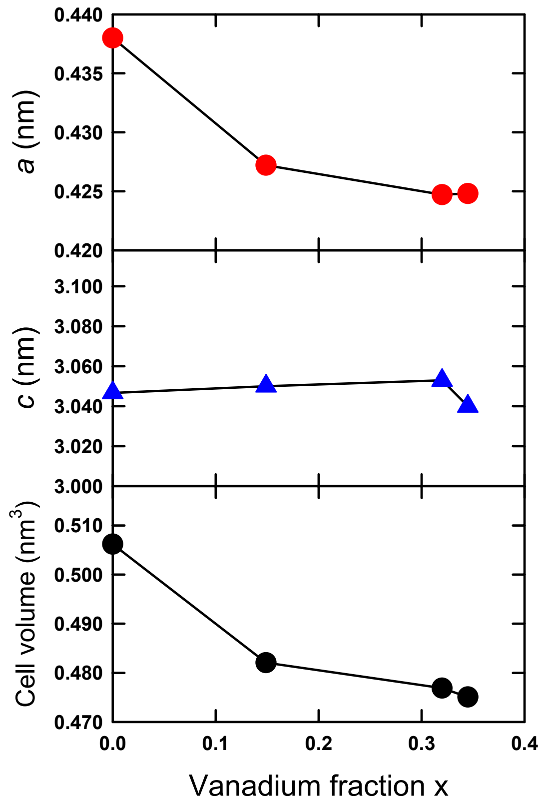

Figure 4.5 Lattice constants and cell volumes of $Sb_{2-x}V_xTe_3$ films vs. vanadium fraction x.

4.3.3 EPMA and Chemical Properties

All $Sb_{2-x}V_xTe_3$ thin film samples were characterized for the stoichiometry and vanadium concentration by using EPMA measurement. In EPMA measurement, the compositions of antimony and tellurium were analyzed according to the L_β line in their characteristic X-ray spectrum while composition of vanadium is determined with the L_β line of its X-ray spectrum. By comparing the intensity of these specific lines from the sample under test with those from a well-known standard samples, the chemical composition can be determined.

The composition of the $Sb_{2-x}V_xTe_3$ films was determined by averaging 75 randomly selected EMPA points for each film. All of these specimens have high compositional uniformity with smaller than 5% deviation in their vanadium concentrations. The atomic ratio (Sb, V) : Te were found close to 40% : 60%. The vanadium fractions of the four $Sb_{2-x}V_xTe_3$ thin film specimens are determined as x=0, 0.15, 0.32, and 0.35. By assuming a reasonable density calculated from the cell volumes (mentioned in the previous section), the thicknesses of these films were estimated and found to be consistent with the results from the Dektak profiler.

4.4 Transport and Magnetic Characterization

4.4.1 Transport Properties

The Hall coefficient was measured by a low-frequency 4-probe AC method in the magnetic field of 1T with 2 different orientations—parallel and perpendicular to *c*-axis. Assuming a single carrier model, the room temperature carrier density extracted from the data is given in Table 4.3. The positive Hall coefficients indicate

that holes are the dominant carriers. In comparison to bulk single crystals of Sb_2Te_3, the carrier density of the Sb_2Te_3 thin film is an order of magnitude smaller, suggesting that the antisite defects are not as prevalent in the MBE grown films as they are in crystals grown under near equilibrium conditions. Upon doping with vanadium, the density of holes rises but may saturate at high-vanadium concentrations. Figure 4.6 shows a temperature-dependent electrical resistivity of $Sb_{2-x}V_xTe_3$ films. Unlike the resistivity measured on bulk single crystals of Sb_2Te_3 which shows a positive coefficient of temperature dependence characteristic of a degenerate semiconductor, the resistivity of the Sb_2Te_3 thin film has a typical semiconducting trend (the resistivity goes higher at a lower temperature). The increased hole concentration upon doping with vanadium is clearly manifested in the much lower resistivity and a considerably weaker semiconducting character. The mobility calculated from the Hall coefficient and electrical resistivity decreases with the increasing concentration of holes.

Table 4.3 Hall coefficient (R_H), carrier concentration (p), resistivity (ρ) and mobility (μ) of a single crystal of Sb_2Te_3 and of $Sb_{2-x}V_xTe_3$ films at 300K.

x	R_H (cm^3/c)	p(cm^{-3})	ρ(μΩm)	μ(cm^2/Vs)
0, Bulk single crystal	0.0589	1.06×10^{20}	1.85	318.38
0	0.1207	5.17×10^{19}	51.91	23.25
0.15	0.0096	6.50×10^{20}	12.61	7.61
0.32	0.0038	1.64×10^{21}	9.98	3.81
0.35	0.0075	8.32×10^{20}	11.48	6.53

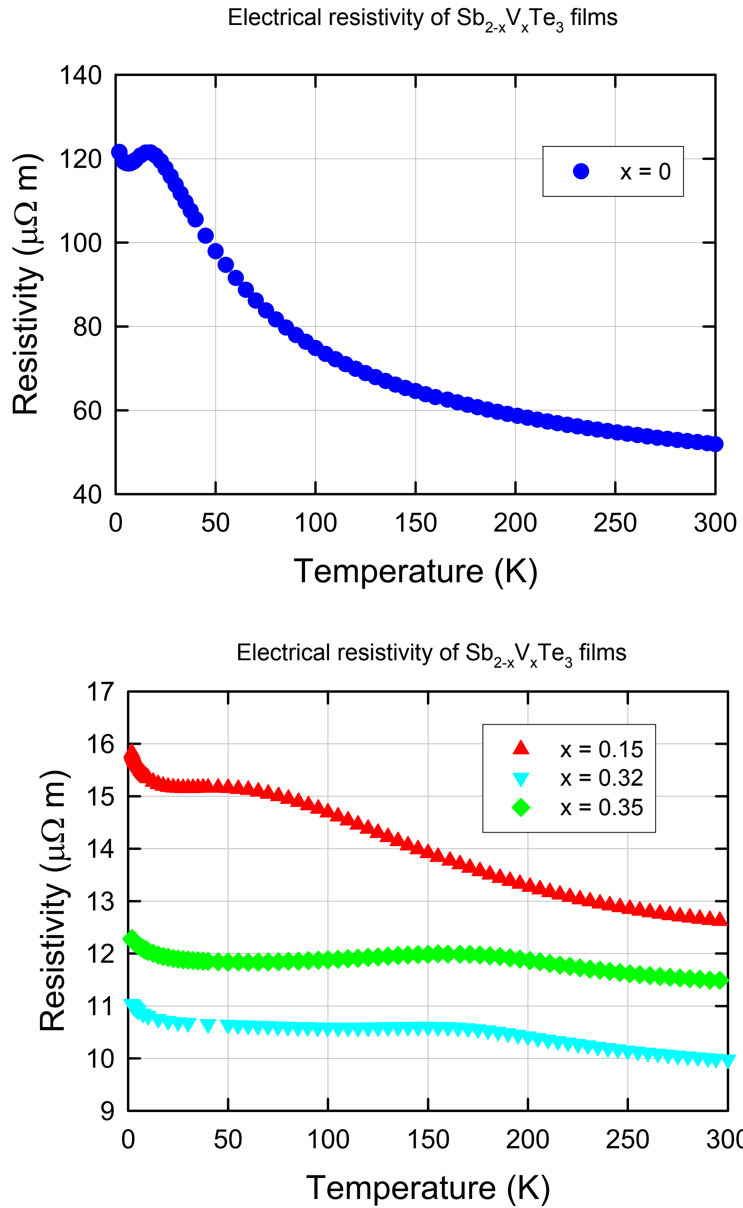

Figure 4.6 Temperature-dependent electrical resistivity of $Sb_{2-x}V_xTe_3$ films grown on sapphire (0 0 0 1) substrates.

4.4.2 Magnetization Measurement

4.4.2.1 Temperature-Dependent Magnetization

A Quantum Design superconducting quantum interference device (SQUID)-based magnetometer equipped with a 5.5 T magnet was used for

magnetization measurements. In order to accurately determine the magnetizations of the thin films, the magnetic responses from the background and substrate have to be taken into consideration as mentioned in section 3.5.1.1. The magnetic responses of the sapphire substrate as well as the plastic straw holder were measured separately and their contributions were subtracted from the raw data. Figure 4.7 shows the temperature-dependent magnetization of $Sb_{2-x}V_xTe_3$ (x=0.15, 0.32, 0.35) thin films during field cooling from 300 to 2 K in the field of 500 Oe applied parallel to the *c* axis of the films (parallel to the growth direction). Upturns on the curves indicate the development of spontaneous magnetization. The arrows in Figure 4.7 mark the inflection points on the curves that are usually taken as temperatures where the structure orders magnetically. Fitting the high-temperature susceptibility data to the Curie-Weiss law, we obtained the transition temperatures of 110, 171, and 182 K for x=0.15, 0.32, and 0.35, respectively.

.

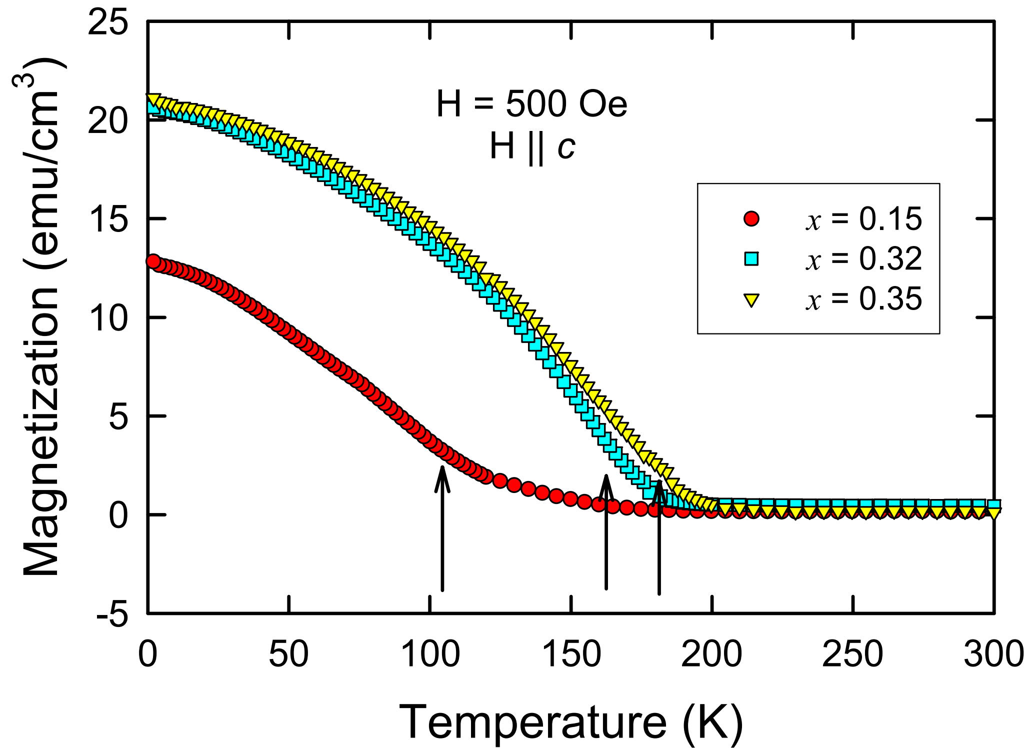

Figure 4.7 Temperature-dependent magnetization of $Sb_{2-x}V_xTe_3$ (x=0.15, 0.32, 0.35) thin films during field cooling from 300 to 2 K in the field of 500 Oe applied parallel to the *c* axis of the films. The arrows mark the inflection points on the curves.

4.4.2.2 M(H) Hysteresis Loop

Figure 4.8 shows the field dependence of the magnetization of $Sb_{1.65}V_{0.35}Te_3$ measured at 2 and 160 K. The demagnetizing field with a demagnetizing factor of 1 in the films was subtracted from the applied magnetic field in the *M(H)* plot. Well developed hysteresis loops are seen at both temperatures, although the coercive field has decreased from 1685 Oe to about 10 Oe as the temperature was raised from 2 to 160 K. Smooth hysteresis loops indicate a well-ordered ferromagnetic structure and coherent rotation of spins in the films. Equally robust and well developed hysteresis

loops were observed on other vanadium-doped Sb_2Te_3 films but with different coercive fields and critical temperatures corresponding to the different contents of vanadium.

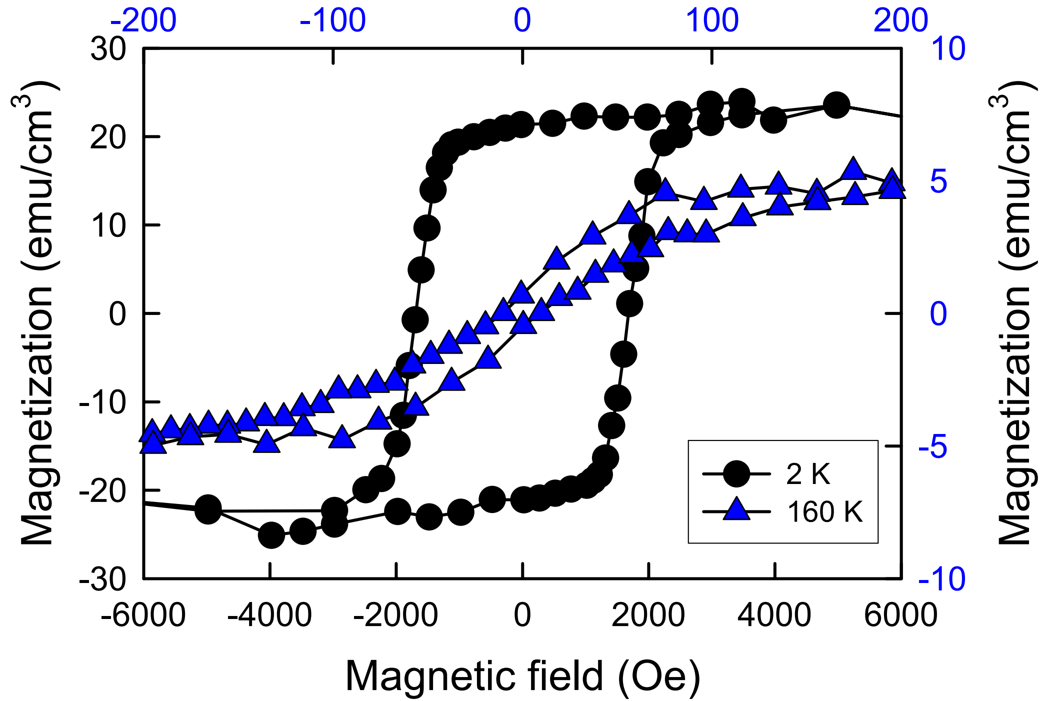

Figure 4.8 Hysteresis loops obtained on the $Sb_{1.65}V_{0.35}Te_3$ film at 2K and 160K.

4.4.3 Arrott Plots

We use Arrott plots to pinpoint the value of the ordering temperature T_C since the effect of magnetic anisotropy and domain rotation can be minimized [48]. As an example, Fig. 4.9 shows the Arrott plot for sample $Sb_{1.65}V_{0.35}Te_3$ around T_C. Equation 10 from Chapter 3 was used to fit the measured magnetization data and the fitting result indicates a transition temperature of 177 K, which is 5 K less than the value obtained from the high-temperature susceptibility results. Arrott plots yield T_C of 104, 168, and 177 K for x=0.15, 0.32, and 0.35, respectively. The dependence of the ordering temperature on the vanadium concentration is shown in Figure 4.10 and

indicates a linear trend. The data suggest that even higher values of the ordering temperature may be possible if one can further increase the concentration of vanadium.

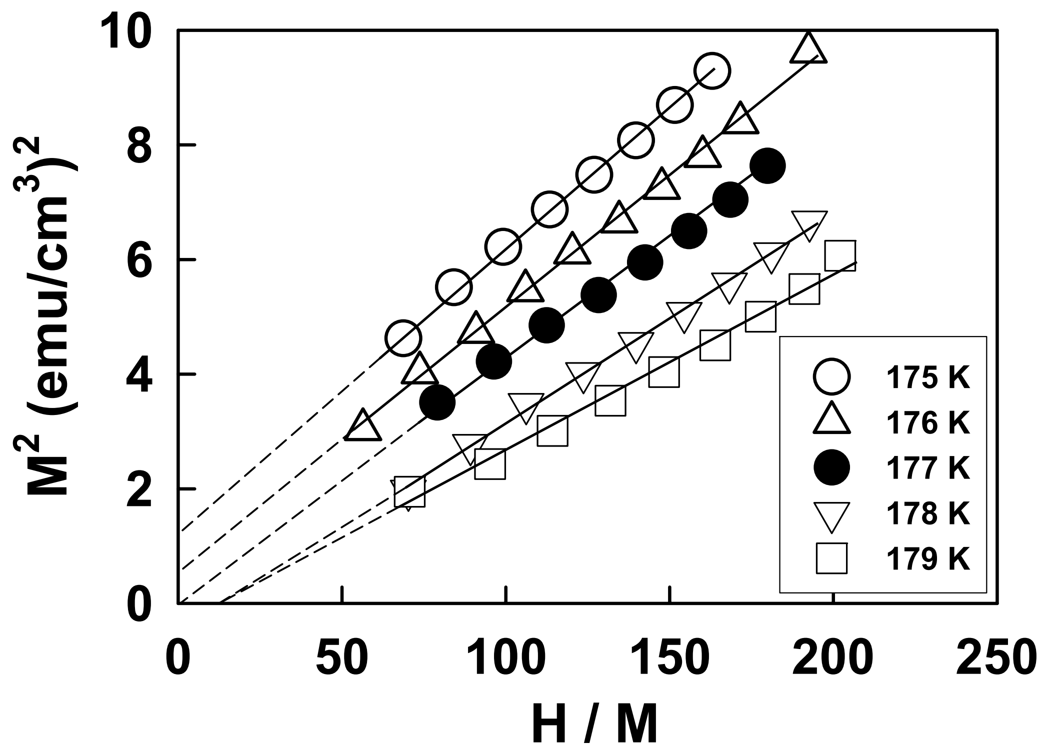

Figure 4.9 The Arrott plot for a thin-film sample $Sb_{1.65}V_{0.35}Te_3$ that yields the ordering temperature of 177 K.

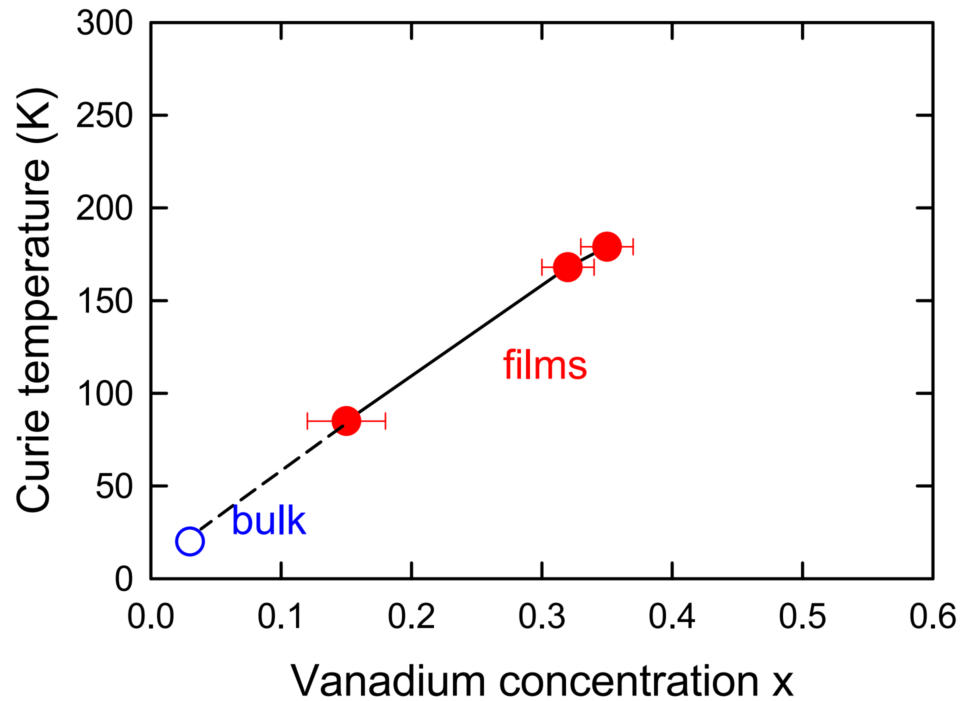

Figure 4.10 Ordering temperature of $Sb_{2-x}V_xTe_3$ thin films as a function of the vanadium concentration x. The error bars indicate an uncertainty in the content of vanadium.

4.4.4 Anomalous Hall Effect

The ferromagnetic state in $Sb_{2-x}V_xTe_3$ films was further confirmed by anomalous Hall effect and magnetoresistivity hysteresis measurements. Figure 4.11 shows the magnetic-field dependent Hall resistivity and magnetoresistivity of $Sb_{1.65}V_{0.35}Te_3$ at 2 K. Both the electrical resistivity and Hall resistivity were measured with the field parallel to the *c* axis and the excitation current applied perpendicular to the *c* axis. Peaks in the magnetoresistance occur at magnetic fields that correspond to zero magnetization (coercive field) and therefore maximum spin disorder in the structure. The Hall resistivity in magnetic materials is expressed as [49]

$$\rho_H = R_0 B + R_S M,$$

where R_0 is the ordinary Hall coefficient, B is the magnetic field, R_S is the anomalous Hall coefficient, and M is the magnetization of the sample. While the ordinary Hall effect dominates at high fields, as seen by the linear dependence of ρ_H with B, the anomalous Hall effect dominates at low field due to the contribution from the magnetization. Hysteresis in both magnetoresistance and the Hall resistivity is detectable to within a couple of degrees of T_C.

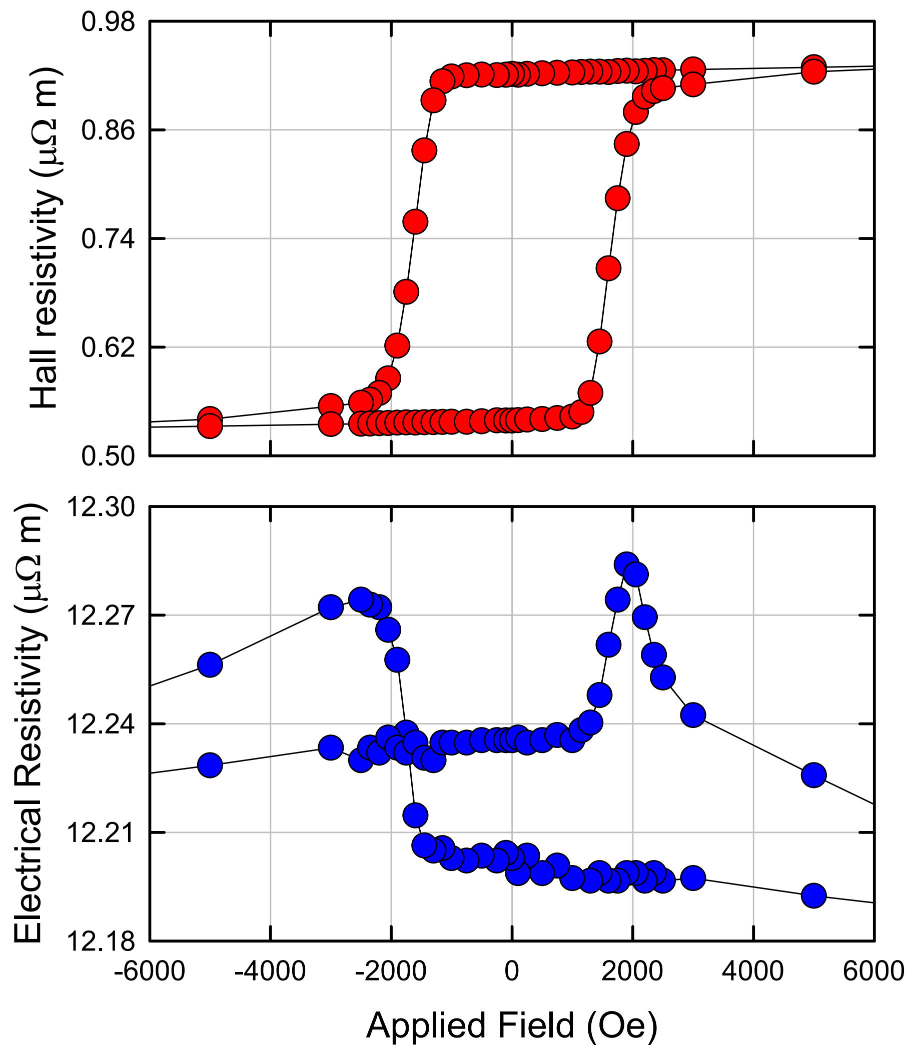

Figure 4.11 Hysteresis loops in the Hall effect and magnetoresistance observed at 2 K on a film with the composition $Sb_{1.65}V_{0.35}Te_3$.

4.5 Discussion

In order to find a possible mechanism of the ferromagnetism in transition-metal doped DMS, it is important to clarify the electronic configuration of the magnetic ion in the lattice where it resides. Transition metal ions which have *d*-orbitals located at the outer shells are known to assume several valence states depending on the lattice environment. The method based on the Curie-Weiss law fitting as described in section 3.5.2.1 is very successful in the case of bulk $Sb_{2-x}V_xSb_3$ with small vanadium doping levels (x<0.03) [26]. The excellent agreement for the expected number of Bohr magnetons and the value extracted from the Curie-Weiss law fitting strongly suggests that vanadium with a valence state (3+) substitutes on Sb sublattice, saturates the bonds, and matches the ionic state of Sb. However, due to the strong doping effect on these thin film specimens, this analysis method can not give any clear suggestions on the configuration of vanadium in the lattice.

Although a solid proof for a specific valence states based on effective Bohr magneton cannot be obtained from heavily doped thin films, the observations of their lattice constants and p-type carrier concentrations still offer useful information to predict possible locations and valence states. Impurities can be incorporated into the Sb_2Te_3 crystal lattice by substituting for the cation (Sb) or anion (Te), by occupying interstitial lattice sites, or possibly by entering the van der Waals gaps. The constant composition ratio of (Sb, V) : Te measured by EPMA provides a convincing evidence supporting that vanadium substitutes on Sb sublattice. Moreover, the ionic radii of Sb^{3+} and Te^{2-} in the octahedral coordination of the tetradymite structure are 0.76 Å and 2.21 Å, respectively. This is to be compared to the ionic radii of various vanadium ions. Vanadium ($3d^3 4s^2$) can give up its 4*s* electrons to become V^{2+} (with an ionic radius of 0.79 Å in octahedral coordination). Alternatively, vanadium can assume

3^+(0.64 Å), 4^+(0.58 Å), or even 5^+(0.54 Å) configurations. If V^{2+} with a larger ionic radius (0.79 Å) substitutes on Sb sublattice and contributes an extra free electron, an increase in the lattice constant and electron density should be observed; however, both predictions contradict the experimental result. Concerning the decreasing lattice constant with vanadium doping, V^{3+}, V^{4+} and V^{5+} with smaller ionic radii are likely to be the incorporated ions. If vanadium entered into the lattice at interstitial positions or the van der Waals gap, i.e., not forming strong bonds, it would likely lose its electrons to the conduction band, thus behaving as an effective electron donor. This situation is not supported by the experimental evidence that indicates substantial increase of hole concentrations due to the vanadium content. Furthermore, one would expect the *c* lattice parameter to increase rather than decrease if vanadium were in the van der Waals gap.

Hole carriers in the thin films can either be supplied by vanadium dopants (V^{4+} and V^{5+}) or come from the antistructural defects (Sb in Te position). It is not entirely clear which mechanism occurs in these thin films. It is possible for vanadium to have 4^+ or 5^+ valence states and act as an dopant for providing holes. V^{3+} is also a possible ion if vanadium can enhance formation of the antistructural defects during the growth.

To clarify the properties of vanadium-doped Sb_2Te_3 thin films, advanced analytical techniques such as X-ray Photoelectron Spectroscopy (XPS) and X-ray absorption and emission study of the valence states using synchrotron radiation should be undertaken.

4.6 Summary

In summary, we have prepared $Sb_{2-x}V_xTe_3$ films with x varying from 0 to 0.35 by MBE. Ferromagnetism that extends to temperatures of at least 177 K was found and confirmed by magnetization, magnetoresistance, and anomalous Hall effect measurements. Although higher vanadium doping obviously gives a higher Curie temperature, some issues are still not clear such as the role the vanadium impurity plays in the Sb_2Te_3 matrix and its influence on the hole concentrations. According to the discussion above, vanadium with 3^+ or 4^+ valence states is very likely involved; however the limited experimental data obtained from our thin film specimens are not adequate to provide a firm proof. Detailed studies of the electronic structure are needed in order to shed light on actual valence state and bonding of vanadium in the Sb_2Te_3 matrix.. In the following chapter, more systematical study will be devoted to Cr-doped Sb_2Te_3 thin film samples. Additional information will be collected and more detailed properties of tetradymite-type DMS are expected to be revealed.

Chapter 5
Chromium-Doped Tetradymite-Type Antimony Telluride

5.1 Introduction

Following the successful deposition of vanadium-doped Sb_2Te_3 epitaxial thin films, in this chapter, the research will be extended to another interesting transition metal, chromium. The 3*d* electron configuration of chromium is different from vanadium and may bring light to new properties concerning the tetradymite-type semiconductors.

5.2 Sample Preparation and Growth Condition

Thin films of $Sb_{2-x}Cr_xTe_3$ with x up to 0.59 were grown in our MBE system by simultaneously evaporating Sb, Te, and Cr onto sapphire (0001) substrates held at 312 °C. Sb and Te were evaporated using Knudsen cells while Cr was deposited with the aid of a miniature *e*-gun. The growth rate of all films was kept at 1.9–2.0 Å/ s. A fixed Te-rich flux ratio Sb: Te=1:4 was intentionally chosen since Te-rich conditions favored the replacement of Sb sites by Cr. In addition, since the deposition rates of Cr were always much smaller than the rates of Sb, the fixed flux ratio of Sb:Te can still yield the tetradymite-type Sb_2Te_3 structure with the correct stoichiometry regardless of the variation in the Cr flux. The deposition rates and overall thickness of the films (typically 0.15 μm) were controlled by calibrated quartz-crystal monitors.

5.3 Structural Characterization

RHEED was used to monitor the surface morphology and crystal properties during the growth. After the growth, the films were subsequently analyzed by x-ray diffraction and electron microprobe analysis (EPMA) to confirm their tetradymite-type crystal structure, film orientation, stoichiometry, and the content and homogeneity of Cr.

5.3.1 RHEED Patterns

Just like the RHEED patterns observed in vanadium-doped Sb_2Te_3 thin films, the RHHED patterns from these chromium-doped sample also indicate a rapid lattice relaxation during the growth of the first few monolayers. During the first few nanometer growth, the observed pattern was combined with streaks and rings. After a few nanometer depositions, streak-like reflection high energy electron diffraction (RHEED) pattern indicates a near layer-by-layer growth of the films on (0001) sapphire even though the lattice mismatch (11%) is rather large.

5.3.2 EPMA

A series of $Sb_{2-x}Cr_xTe_3$ films has been prepared spanning x up to 0.59. The composition of the $Sb_{2-x}Cr_xTe_3$ films was determined by averaging 30 measurements taken at randomly selected locations on each film. The EPMA maps indicate a homogeneously distributed Cr without any tendency to cluster at least on the scale of the instrument resolution. Table 5.1 show the thickness and chemical composition of each $Sb_{2-x}Cr_xTe_3$ thin film specimen.

Table 5.1 Chromium fraction and film thickness measured on different samples.

Sample Lot No.	e-beam power (Watt)	x	Thickness (Å)
20051219	29.0	0.10	2122
20060219	33.2	0.19	820
20060122	33.2	0.31	1759
20060123	33.0	0.44	1805
20060322	36.1	0.59	1638

5.3.3 X-Ray Diffraction

Fig. 5.1 shows the x-ray diffraction pattern of $Sb_{2-x}Cr_xTe_3$ films. Except for sapphire substrate peaks observed in the XRD pattern, only (00.n) reflections in the hexagonal unit cell are present, confirming that the films grow parallel to the *c*-axis direction. No trace of any secondary phase formation was found from the XRD scans.

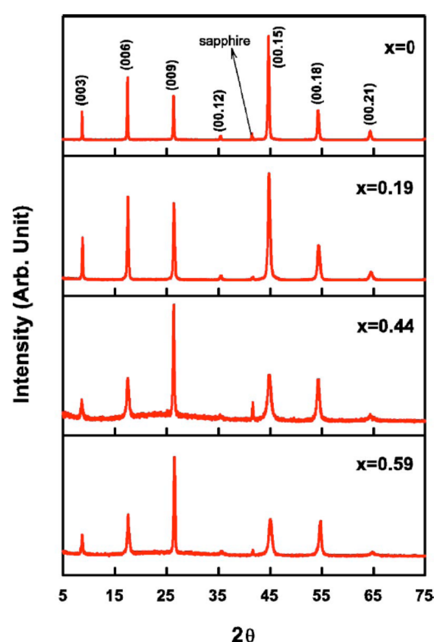

Figure 5.1 X-ray diffraction patterns of $Sb_{2-x}Cr_xTe_3$ films on sapphire (0001) substrates.

5.3.4 Lattice Constants

The dependence of the lattice constants *a* and *c* of $Sb_{2-x}Cr_xTe_3$ films respectively determined from the RHEED and XRD patterns as a function of chromium concentration *x* is plotted in Fig 5.2. The *a*-axis lattice constant decreases with the increasing concentration of chromium. The *c*-axis lattice constant also decreases with the increasing chromium content but the percentage change is much smaller. Overall, the hexagonal unit cell of the films decreases with the increasing x. Following the same analysis as in last chapter concerning the valence state and location of impurity ions, chromium is not likely to substitutes on the anion site of Te, enter inside the van der Waal gap, nor occupy interstitial positions. Given the formal ionic radii of Sb^{3+} (0.76 Å) and Te^{2-} (2.21 Å) in the octahedral coordination of the tetradymite structure and the ionic radii of various Cr ions [Cr^{2+} (0.80 Å), Cr^{3+} (0.62 Å), Cr^{4+} (0.55 Å), Cr^{5+} (0.49 Å)], it is clear that Cr cannot occupy the anion sites. If Cr occupied interstitial positions or was located in the van der Waals gap, large lattice expansion would ensue, and this is not observed. Moreover, weak bonding of Cr in such positions would likely lead to a stripping of its electrons and thus a decrease in the density of holes. As we discuss in the following section, the exactly opposite trend is observed—the density of holes increases modestly as more Cr is incorporated in the crystal lattice. Thus, the above considerations suggest that Cr substitutes on the Sb sublattice just as was the case of Cr in bulk single crystals of Sb_2Te_3 [50]. This conclusion is also strongly supported by the Cr magnetization analysis discussed later on in this chapter.

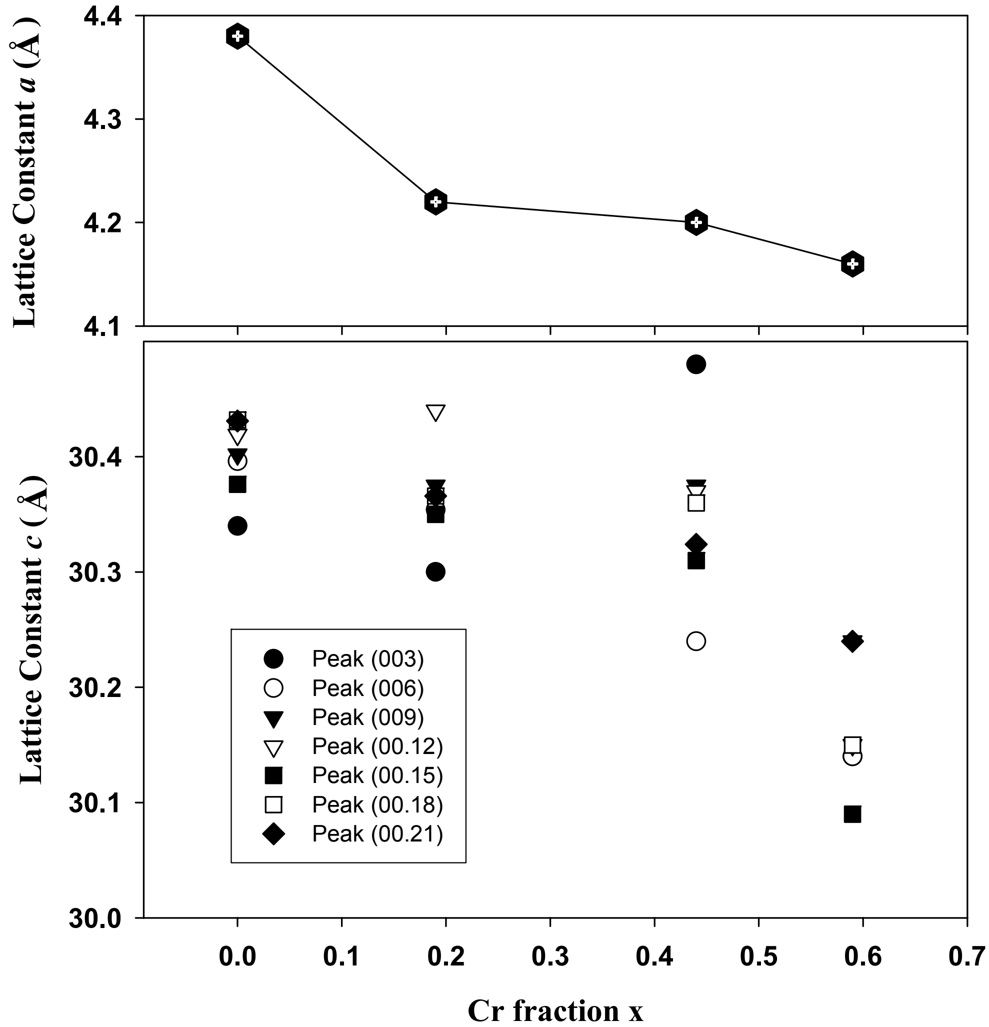

Figure 5.2 Lattice constants of $Sb_{2-x}Cr_xTe_3$ films as a function of Cr fraction x.

5.4 Electrical and Magnetic Properties

Magnetization measurements were done in a Quantum Design SQUID-based magnetometer equipped with a 5.5 T magnet. Great care was taken when extracting the magnetization data of the film samples. Magnetization of the sapphire substrate as well as of the plastic straw holder was measured separately and their respective contributions were subtracted from the raw data. Electrical resistivity and the Hall

effect were measured using an AC bridge with 16 Hz excitation, the current was injected parallel to the film plane and the magnetic field was oriented perpendicular to the film.

5.4.1 Magnetization

Ferromagnetism in our $Sb_{2-x}Cr_xTe_3$ films was confirmed by field dependence of the magnetization. Fig. 5.3 shows the temperature dependent magnetization of several films of $Sb_{2-x}Cr_xTe_3$ with a progressively increasing content of Cr. The data were taken in the magnetic field of 100 Oe applied perpendicular to the plane of the films upon cooling from 300 K down to 2 K. When the temperature is lowered below 200 K, the initial very small and nearly constant magnetization at high temperatures undergoes a sharp upturn, indicated by arrows in Figure 5.3. The sample with the highest content of Cr (x=0.59) has the highest onset temperature and the samples with the lower concentration of Cr show upturns at progressively lower temperatures. In comparison, pure Sb_2Te_3 displays a weakly diamagnetic behavior and on the scale of Fig. 5.3 its trace overlaps with the baseline with no hint of any upturn down to 2 K. The upturns on the magnetization curves of Cr-doped Sb_2Te_3 films indicate the onset of long-range magnetic ordering (ferromagnetism) in the film

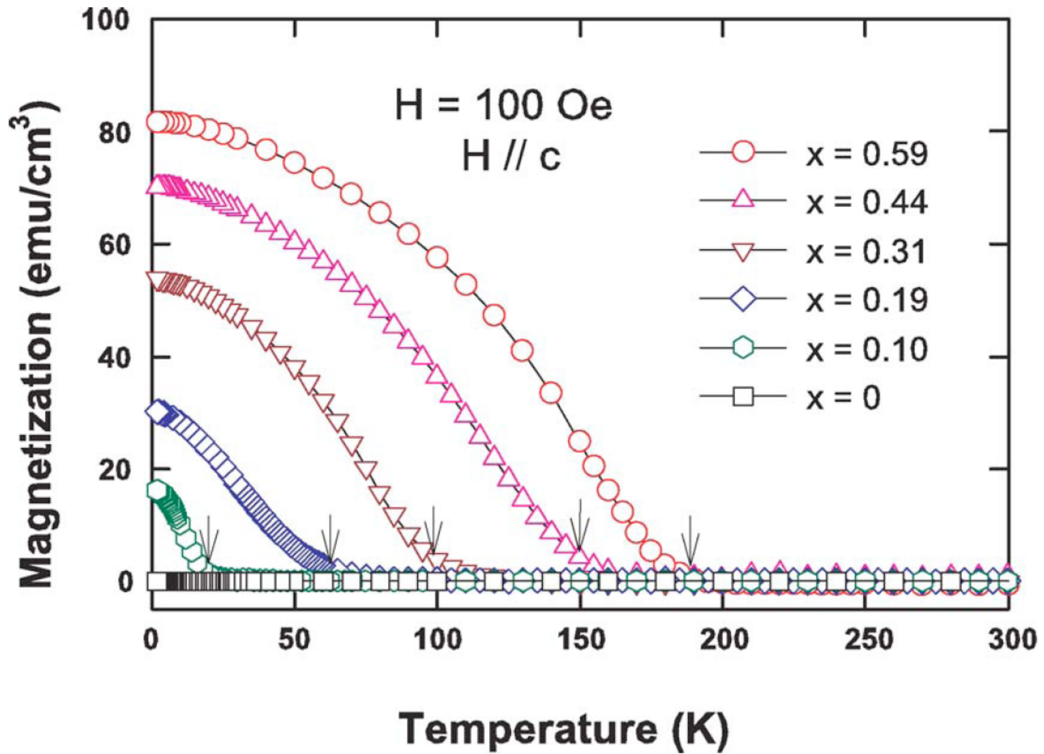

Figure 5.3 Temperature dependent magnetization of $Sb_{2-x}Cr_xTe_3$ thin films.

To verify the magnetic properties, low-temperature magnetization studies were performed in a field up to 3000 Oe. Well developed hysteresis loops were obtained in all of these Cr-doped thin films at a temperature of 10K upon cycling the magnetic field as shown in Fig. 5.4. The coercive field is about 200 Oe for a film with Cr fraction x=0.1 and increases to 850 Oe when the Cr content rises to x=0.59. Smooth hysteresis loops indicate a well-ordered ferromagnetic structure and coherent rotation of spins in the films. Both coercive field and saturation magnetization increase with increase of x.

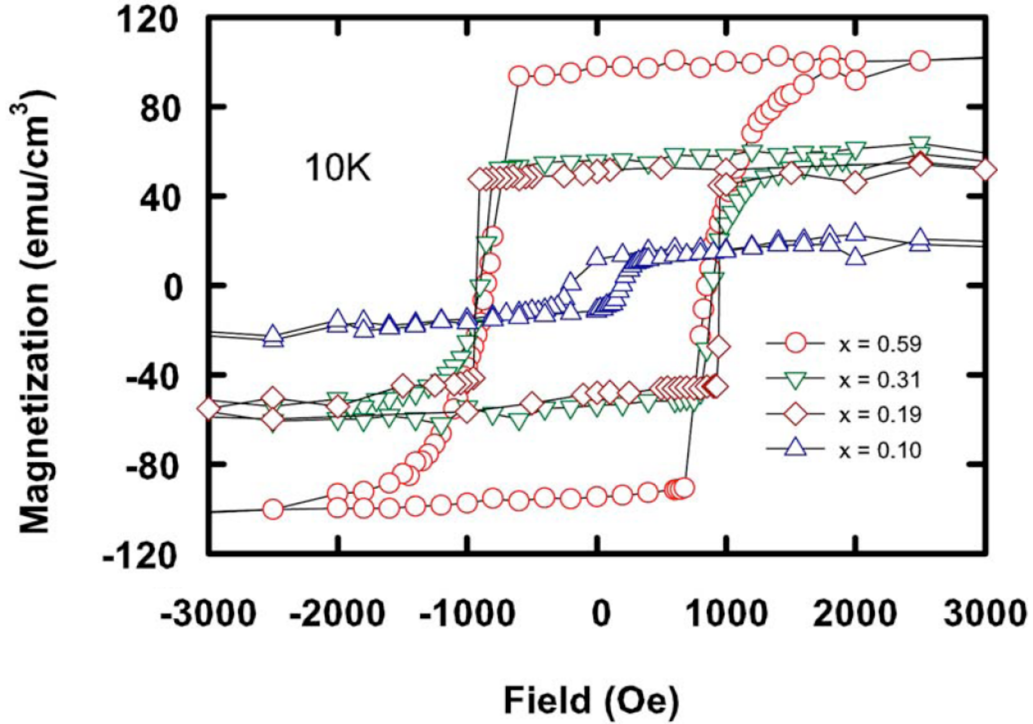

Figure 5.4 Magnetic hysteresis loops of $Sb_{2-x}Cr_xTe_3$ thin films.

5.4.2 Arrott Plots and Critical Temperatures

Just in the case of vanadium-doped Sb_2Te_3, we used Arrott plots to determine the exact value of the Curie temperature. Again, this technique minimizes the effect of magnetic anisotropy and domain rotation [48,51] and is viewed as the most reliable and accurate determination of the ordering transition. The Curie temperatures are shown in Fig. 5.5 as a function of Cr concentration *x*. A nearly linear increase of the Curie temperature with increasing concentration of Cr is observed. Currently, the maximum Curie temperature is 190 K for the film $Sb_{1.41}Cr_{0.59}Te_3$. Our data suggest that even higher values of the ordering temperature may be possible if one can further increase the concentration of Cr.

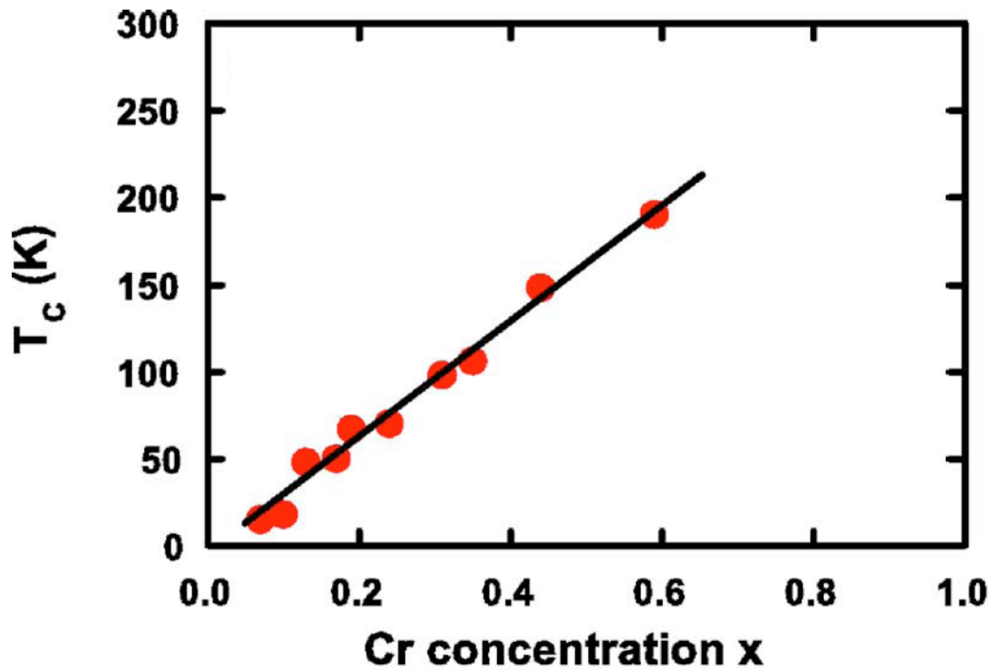

Figure 5.5 Curie temperature of $Sb_{2-x}Cr_xTe_3$ thin films as a function of Cr concentration *x*.

5.4.3 Resistivity and Transport Behavior

Figure 5.6 shows the temperature dependence of the electrical resistivity of the same films. The resistivity of an undoped Sb_2Te_3 film shows a typical semiconducting behavior with a negative coefficient of temperature dependence. This is different from bulk single crystals of Sb_2Te_3 which usually have a positive coefficient of temperature dependence characteristic of a degenerate semiconductor. Such difference is mainly due to the different carrier concentrations in Sb_2Te_3 single crystals and Sb_2Te_3 films. Typical carrier concentration in Sb_2Te_3 single crystals and Sb_2Te_3 film are 10^{20} cm^{-3} and 5.2×10^{19} cm^{-3}, [52] respectively, reflecting different concentrations of antisite defects of the type Sb_{Te} (i.e., antimony located on the site of Te). All curves of resistivity vs. temperature of Cr-doped films show a local maximum (hump) around T_C, which moves to higher temperatures with the increasing

concentration of Cr. Such behavior of the resistivity is the result of spin-disorder scattering that sets in at the paramagnetic-to-ferromagnetic transition [53,54]; in other words, it indicates the magnetic ordering temperature of the films. The temperatures at which the resistivity reaches the local maximum are marked with arrows in Figure 5.6. It can be seen that these temperatures correspond very well to the magnetic onset temperatures in Figure 5.3. While $Sb_{2-x}Cr_xTe_3$ films with low Cr content (x=0.31) show metallic character of resistivity, (except at very low temperatures where a slight upturn is observed), the two films with high content of Cr (x=0.44 and x=0.59) show a negative temperature coefficient in their paramagnetic

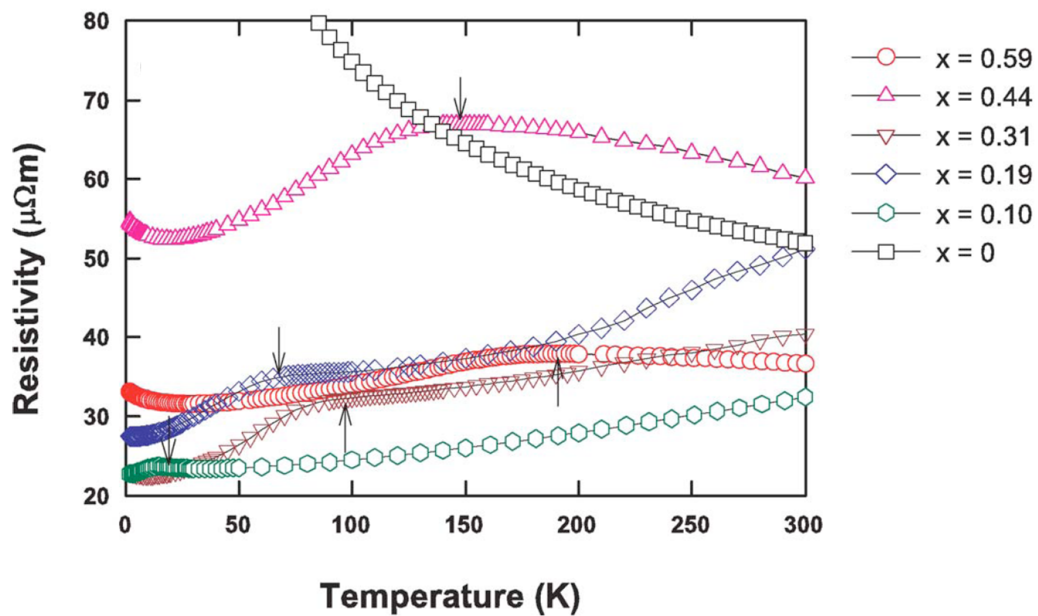

Figure 5.6 Temperature dependent electrical resistivity of $Sb_{2-x}Cr_xTe_3$ films in zero magnetic field.

domain, i.e., the films undergo a metal-insulator transition as a function of Cr concentration. These two films also display more pronounced upturns at the lowest temperatures. Below the magnetic ordering temperatures, all resistivity curves show

similar temperature dependences characterized by a decreasing resistivity before a minimum is reached at temperatures varying from 29 K down to 2.5 K, the lower temperature corresponding to the lower Cr concentration. It is not clear whether the upturns at very low temperatures arise as a consequence of localization or are a signature of the carrier freeze out. Dyck et al.[50] and Kulbachinskii et al.[55] studied the temperature dependence of the resistivity of Cr-doped Sb_2Te_3 bulk single crystals and their results indicated metallic behavior. The Cr mole fraction x in their bulk crystalline samples is less than 0.1 and in this range of concentrations our data on Cr-doped Sb_2Te_3 films are in good agreement with the bulk Cr-doped Sb_2Te_3 crystals. We note that impurity concentration dependent metal-insulator transition was also observed in Mn-doped GaAs [56,57].

5.4.4 Hall Measurement

5.4.4.1 Hall Measurement and Carrier Concentration

Room temperature hole concentration was obtained through Hall coefficient measurements. Since at 300 K all films are in their paramagnetic phase, there is no complication with an anomalous Hall effect contribution, and the carrier density can be unambiguously determined, assuming that a single band model adequately describes the carrier spectrum. Unlike in Bi_2Te_3 where the intrinsic conduction starts to contribute at ambient temperatures, the gap in Sb_2Te_3 is larger (0.26 eV) and the intrinsic effects do not enter the picture at 300 K. Figure 5.7 shows the hole concentration as a function of Cr content. Overall, the concentration of holes increases modestly with the Cr content. The actual hole concentration in each film is also influenced by the density of antisite defects, i.e., the particular nonstoichiometry that

reflects the growth conditions and perhaps even by the interaction of these native defects with the Cr ions.

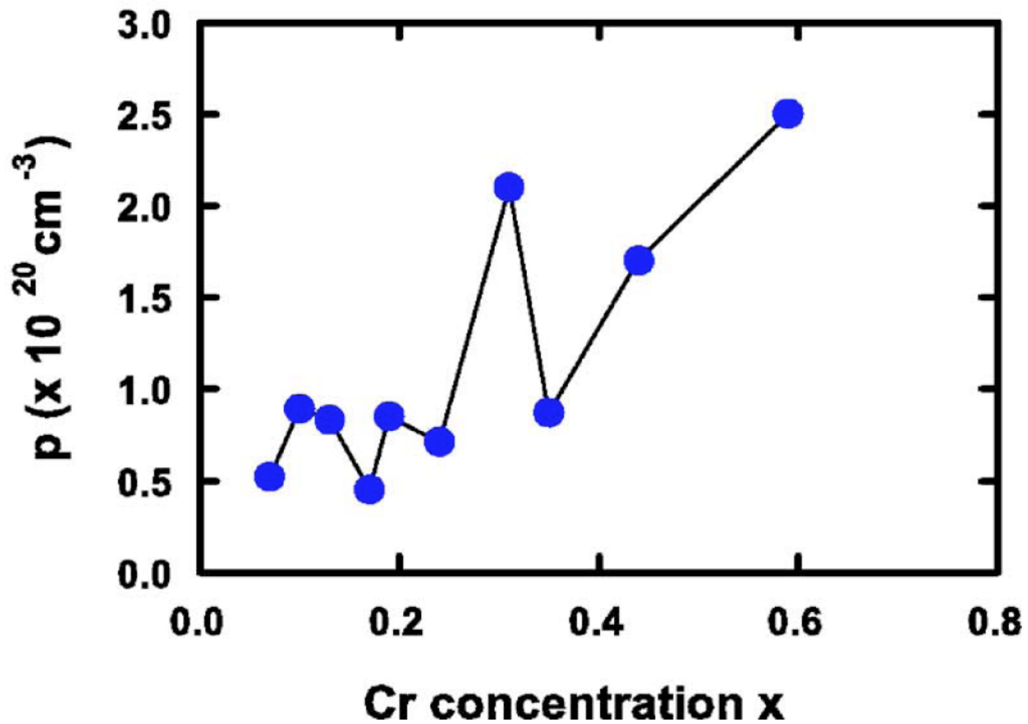

Figure 5.7 Room temperature hole concentration as a function of Cr content *x*.

5.4.4.2 Anomalous Hall Measurement

The ferromagnetic state in $Sb_{2-x}Cr_xTe_3$ films was further confirmed by anomalous Hall effect measurements. Figure 5.8 shows the magnetic field dependent Hall resistivity of $Sb_{2-x}Cr_xTe_3$ films at 10 K. The Hall resistivity was measured with the field parallel to the c axis and the excitation current applied perpendicular to the c axis. As already stated in section 3.5.3.2, the Hall resistivity in magnetic materials is expressed as: $\rho_H = R_0 B + R_M M$, where R_0 is the ordinary Hall coefficient, B is the magnetic field, R_M is the anomalous Hall coefficient, and M is the magnetization of the sample. While the ordinary Hall effect dominates at high fields, as seen by the linear dependence of ρ_H with B, the anomalous Hall effect dominates at low fields due

to the contribution from the magnetization. Similar to the case of vanadium-doped Sb_2Te_3, hysteresis loops in the Hall effect are detectable to within a couple of degrees of T_C.

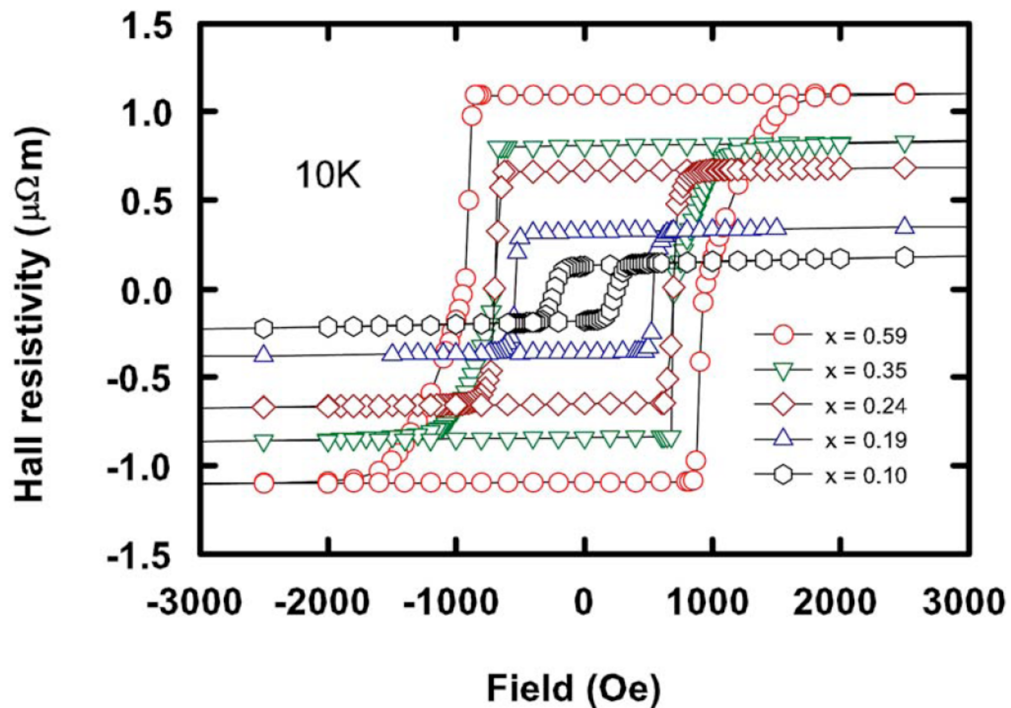

Figure 5.8 Magnetic field dependent Hall resistivity of $Sb_{2-x}Cr_xTe_3$ films.

5.4.5 XPS Measurement

X-ray Photoelectron Spectroscopy measurement was taken on a Kratos Axis Ultra XPS in order to study the chemical binding property of chromium in Sb_2Te_3 matrix. As shown in Fig. 5.9, the XPS spectra were taken on a 215nm thick, $Sb_{2-x}Cr_xTe_3$ (x=0.22) thin film sample before Ar^+ ion etching and after 40min, 90min and 140min ion etching. Carbon and oxygen are both common contaminants on the surface of many samples. The 1s O peak and 1s C peak are clearly seen in the surface of our sample before ion etching, indicating possible native oxidation and acetone or isopropanol residence at the surface. These contaminations were observed only near

the surface since their peaks in the spectrum disappeared after the ion etching. The typical binding energies of Cr $2p^{3/2}$ and $2p^{1/2}$ are around 574.1 eV and 583.8 eV, respectively [58]. To study the possible binding energy shifts due to different valence states, the spectrum near the target energy should be carefully analyzed. Fig. 5.10 is an enlarged spectrum from Fig. 5.9 with an energy scale from 565eV to 585eV. In Fig. 5.10, if compared to the spectrums after ion etching which have only two main peaks (at around 570 eV and 580 eV) , the spectrum before ion etching show two other obvious peaks (at 573 eV and 584 eV). Each chromium peak is split into two peaks on the surface, revealing the presence of two forms of chromium. In general, an element with a higher valence number has a higher binding energy. The shift is around 3~4eV between the extra peak and the main peak. Therefore, these extra peaks are believed from chromium native oxide (possibly Cr^{6+} in CrO_3) at the surface since only large valence number difference can cause a shift more than 3eV. As can be seen in Fig. 5.10, the $2p^{1/2}$ and $2p^{3/2}$ peaks for Cr inside the thin film sample are very close to the $3d^{3/2}$ and $3d^{5/2}$ peaks for Te. Thus, chromium in the thin film is likely to have smaller valence number (2^+ or 3^+). In order to analyze the spectra in more detail and get more solid evidence for the valence state of Cr, higher resolution scan and Te peak subtraction should be taken.

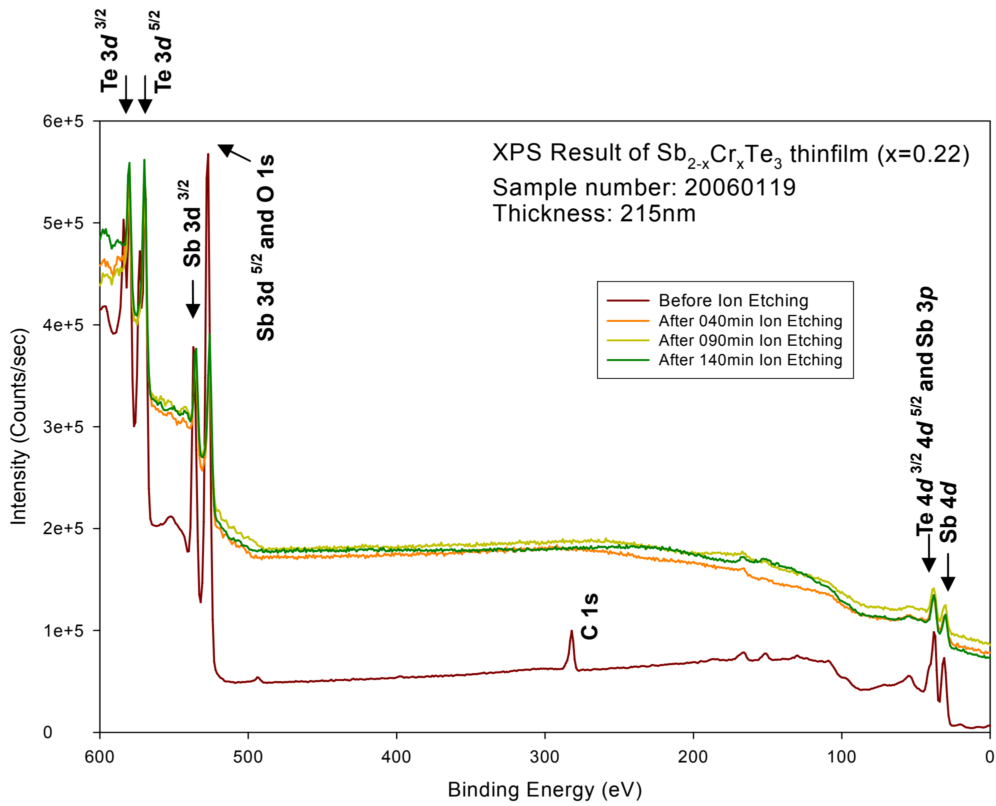

Figure 5.9 XPS Spectrum of the $Sb_{1.78}Cr_{0.22}Te_3$ thin film sample before ion etching and after 40mins, 90mins and 140mins ion etching, marked with specific binding energies of related elements.

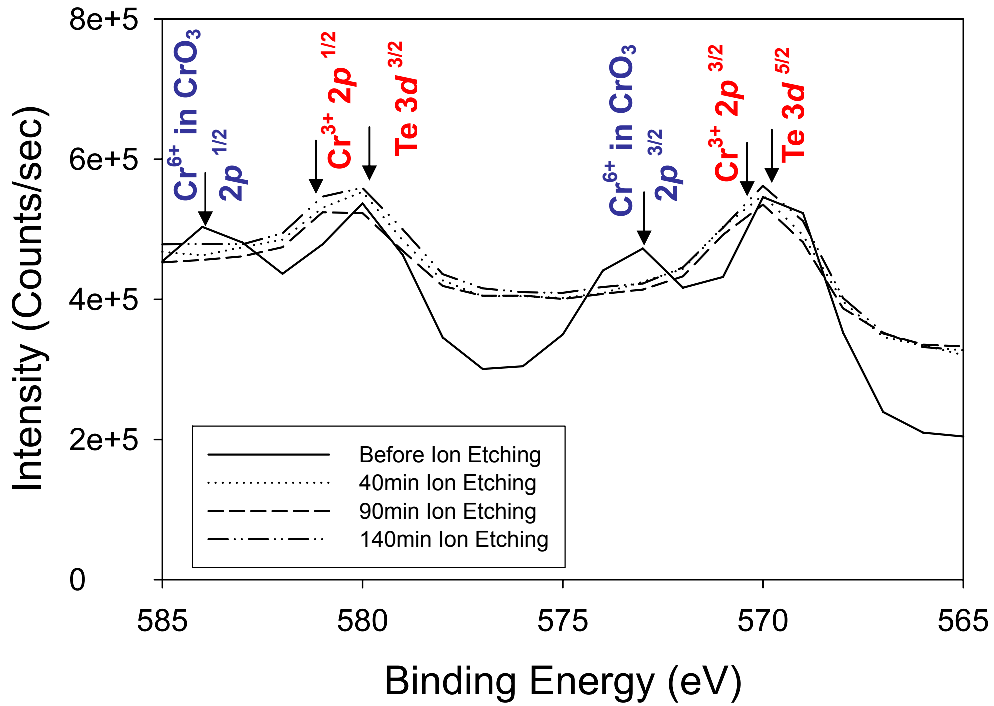

Figure 5.10 The enlarged XPS spectrum for binding energy around 575eV for the analysis of Cr.

5.5 Discussion

It is evident that the films of $Sb_{2-x}Cr_xTe_3$ display robust ferromagnetism. Moreover, as Fig. 5.11 indicates, the plot of the Curie temperature is proportional to $xp^{1/3}$ where x is the impurity concentration and p is the density of holes. This might suggest that the well-known Ruderman-Kittel-Kasuya- Yoshida (RKKY) interaction is at play [59,60] and the films thus represent an example of a diluted magnetic semiconductor (DMS). However, as with essentially all DMSs, a question arises regarding a possible formation of clusters or precipitate phases that might be the source of the long-range magnetic order instead of uniformly distributed Cr atoms on the Sb sublattice. At this stage, we do not have available a detailed structural

information, such as high resolution transmission electron micrographs. Furthermore, as Fig. 5.6 indicates, the dependence of the carrier (hole) density on the concentration of Cr ions is rather weak and the Curie temperature in dominated by its dependence on the Cr content x rather than its dependence on the charge carrier density p. These are clearly issues that make the case for the RKKY interaction and the diluted character of these magnetic semiconductor films debatable. Nevertheless, there are also features that are supportive of the notion that these films are diluted magnetic semiconductors. From the high field-saturation magnetization (M_S) done at 10 K, the number of Bohr magnetons per Cr ion in the $Sb_{2-x}Cr_xTe_3$ films can be estimated by M_S/N, where N is the number of Cr ions determined by EPMA. Our calculations give the values of the number of Bohr magnetons per Cr ion as 3.04 μ_B, 2.97 μ_B, 3.00 μ_B, and 2.86 μ_B, for x=0.10, 0.24, 0.35, 0.59, respectively. Overall, the values are very close to $3\mu_B$ across the entire spectrum of Cr concentrations, including low concentrations of Cr in bulk single crystals, and indicate three unpaired spins all pointing in the same direction, i.e., the spin only value of S=3/2. Thus, there is a strong and consistent evidence for the valence state of Cr being 3^+ as it substitutes for the formally Sb^{3+} ion on the antimony sublattice. It should be pointed out that the 3^+ valence of antimony is merely a formal designation for Sb-Te bonding in Sb_2Te_3 which in reality is not purely ionic but has a substantial covalent character as well. The apparently isoelectronic substitution of Cr for Sb is the main reason why one observes a rather weak charge carrier (hole) dependence on the content of Cr. Nevertheless, the overall fivefold increase in the density of holes is detected, Fig. 5.7, and this just might be enough to support the RKKY interaction mechanism. Had the films contained impurity phases such as CrTe, Cr_3Te_4, or Cr_2Te_3 (known to be ferromagnetic with saturation moments around 2.0–2.7 μ_B and Curie temperatures ranging from 180 K to 340 K), we would not observe a linearly dependent variation of

T_C on the concentration of Cr nor the smooth hysteresis loops.

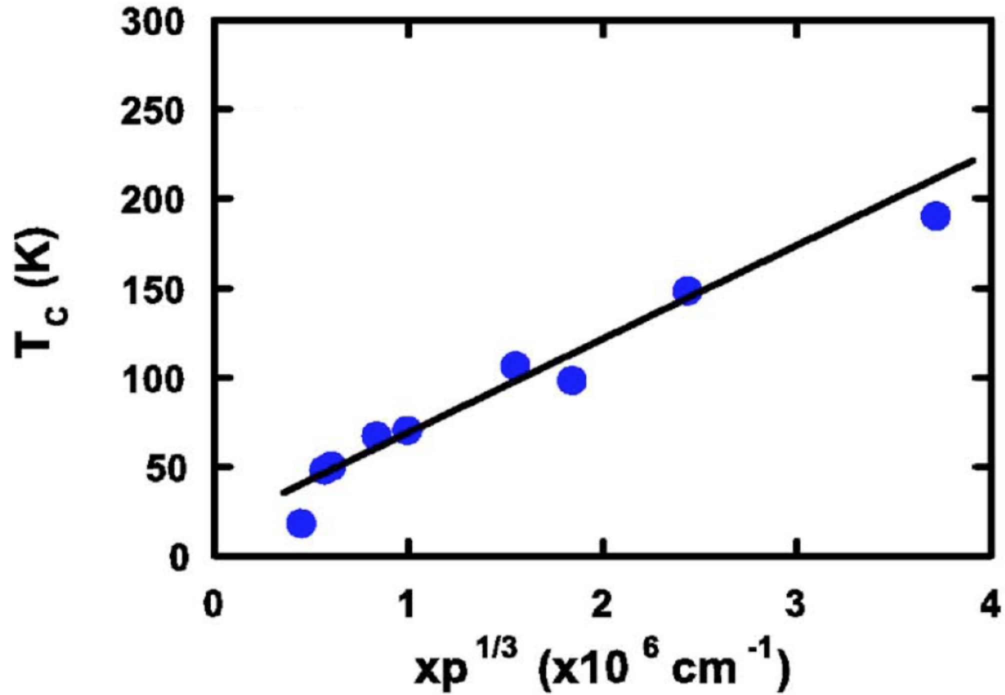

Figure 5.11 Curie temperature of $Sb_{2-x}Cr_xTe_3$ thin films as a function of $xp^{1/3}$.

5.6 Summary

In summary, by making use of low-temperature molecular beam epitaxy, we have been able to dramatically extend the range of solubility of Cr in Sb_2Te_3 and prepared well oriented $Sb_{2-x}Cr_xTe_3$ films with x up to 0.59. The films possess high Curie temperatures that increase linearly with the content of Cr and reach 190 K in $Sb_{1.41}Cr_{0.59}Te_3$ films. The ferromagnetic state was confirmed by hysteresis in the magnetization and by the presence of the anomalous Hall effect. Magnetization analysis indicates that Cr substitutes on the antimony sublattice and attains the valence state of 3^+, just as was the case in bulk single crystals. The resulting relatively weak dependence of the density of holes on the content of Cr brings into question the applicability of the RKKY interaction. On the other hand, the linearly varying Curie

temperature and smooth hysteresis loops suggest that the system is consistent with the behavior of a diluted magnetic semiconductor. The preferentially perpendicular orientation of magnetic spins in the films of $Sb_{2-x}Cr_xTe_3$ makes the system of potential interest for ultrahigh density perpendicular magnetic recording.

Chapter 6
Iron-Doped Tetradymite-Type Bismuth Telluride

6.1 Introduction

Bi_2Te_3 is also a tetradymite-type semiconductor similar to Sb_2Te_3 but with a narrower bandgap. A transition metal impurity is supposed to have similar effect on magnetic properties in Bi_2Te_3 system. Ferromagnetism at low temperature (up to 12K) has been confirmed in $Bi_{2-x}Fe_xTe_3$ bulk crystalline samples (x=0.08) [61]. Therefore, it is very interesting to study the $Bi_{2-x}Fe_xTe_3$ material with a higher Fe content.

6.2 Sample Preparation

$Bi_{2-x}Fe_xTe_3$ epitaxial thin film samples were grown on sapphire (0001) substrates at by LT-MBE with Te-rich growth condition. The flux ratio of Bi : Te is kept at 1:3. The deposition rates of Bi and Te are 0.3 Å/sec and 0.9 Å/sec respectively, given by the calibrated crystal thickness monitor. The deposition rate of iron was controlled by the power of the miniature e-beam evaporator. The growth temperature for $Bi_{2-x}Fe_xTe_3$ epitaxial thin films is around 300°C.

6.3 Structural Determination

6.3.1 RHEED and XRD

The lattice mismatch of Bi_2Te_3 on sapphire (8%) is smaller than the mismatch of Sb_2Te_3 on sapphire (11%). During the first several nanometer growth, both streaks and spots were observed. The spotty pattern indicated the three dimensional growth on the substrate. The spotty pattern gradually disappeared and then only clean streak patterns left after about 15nm growth. The streak patterns have a similar 3-fold symmetry (repeat every 60 degree of rotation) as mentioned in 4.3.1. XRD measurement only showed peaks from planes parallel to c-plane. No other peak was observed. These results from RHEED and XRD indicated these thin films were grown epitaxially in a single crystal form and the c-axis is perpendicular to the sample surface in a hexagonal structure.

6.3.2 Lattice Constants

The lattice constants of the samples with different iron contents were extracted from the RHEED patterns and the XRD measurement. Figures 6.1 and 6.2 show the a-axis and c-axis lattice constants as a function of iron fraction x. Both lattice constants of a and c decrease with increasing iron fraction since the ionic radius of iron is smaller than the radii of bismuth and tellurium.

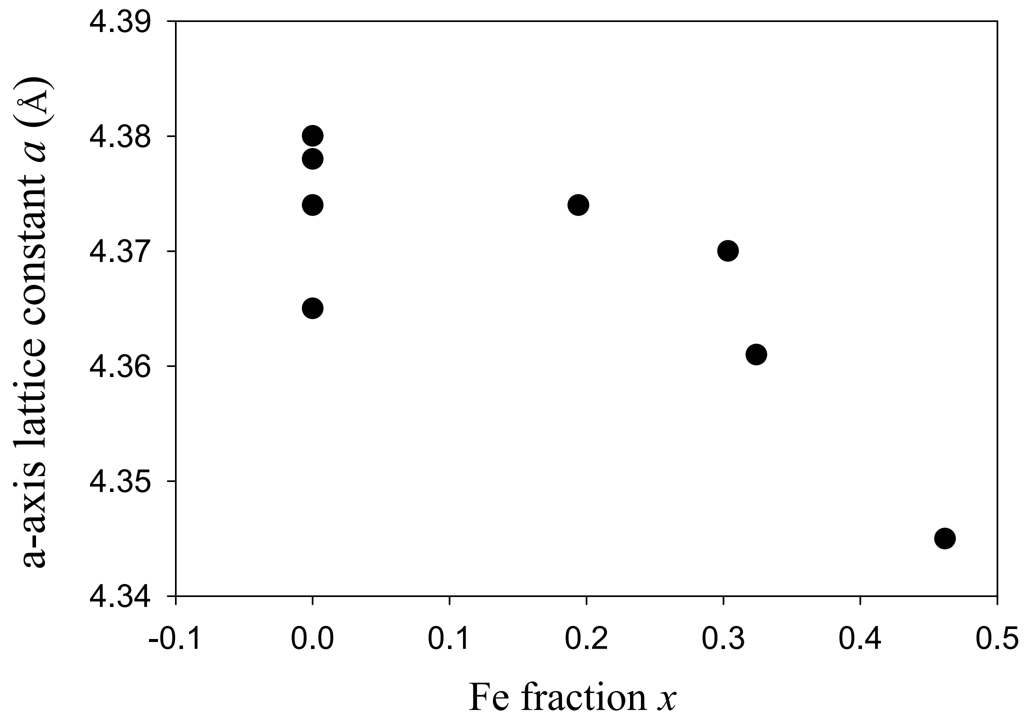

Figure 6.1 a-axis lattice constant a vs. Fe fraction *x*

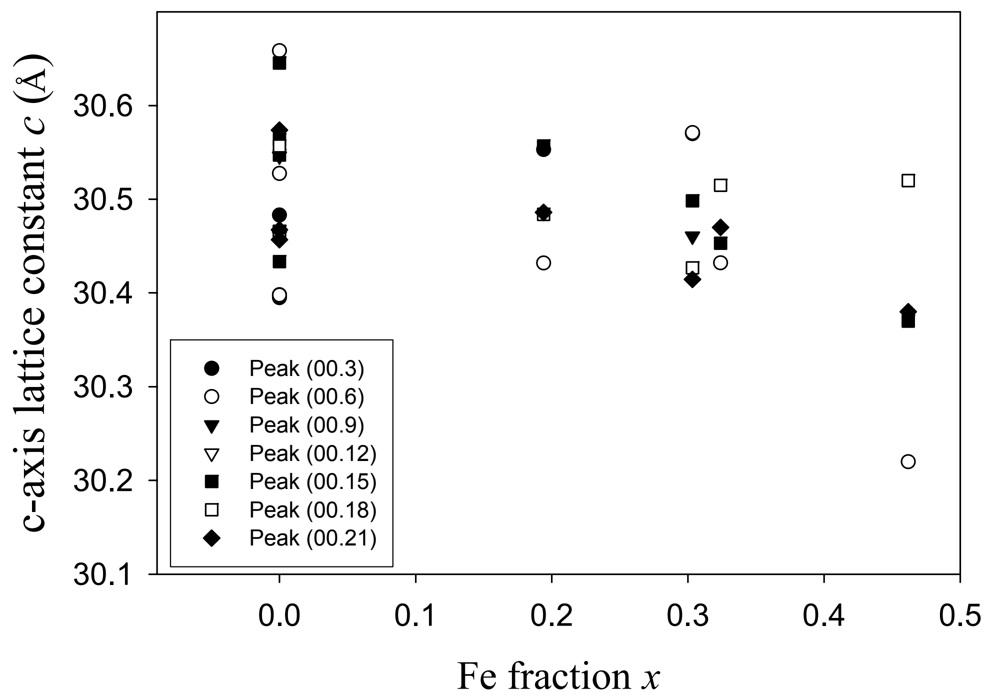

Figure 6.2 c-axis lattice constant vs Fe fraction *x*

6.4 Characterization

6.4.1 Transport Properties and Hall Measurement

Hall effect and resistivity measurements were taken on $Bi_{2-x}Fe_xTe_3$ thin film samples (for x=0, 0.19 and 0.46) to characterize their transport properties. Fig. 6.5 shows the temperature dependent resistivity from 2K to 350K. In the lower temperature range (<100K), the resistivity of Fe-doped samples is larger than the resistivity of undoped one, indicating the doping of iron cause impurity scattering thus lower the carrier mobility. While the pure Bi_2Te_3 thin film sample show a notable temperature dependent resistivity, the resistivity of the Fe-doped samples display only a very weak effect of temperature, revealing that the conduction electrons in doped samples are less sensitive to phonon scattering. A data set of carrier concentration, resistivity and mobility measured at 10K on a Bi_2Te_3 bulk single crystal sample and $Bi_{2-x}Fe_xTe_3$ thin film samples (for x=0, 0.19 and 0.46) is listed on Table 6.1. One can notice that the bulk sample presents *p*-type conductivity while these thin film samples have *n*-type behavior. The electron mobility of the thin film samples is even lower than the hole mobility measured on the bulk crystal. The depression on mobility is considered to be related to surface and interface scattering in thin film samples. Fe seems not a good donor in the Bi_2Te_3 thin films due to weak dependence between carrier concentration and the Fe fraction x. Thus it is likely that the Fe ions interact with the antisite defects and this interaction plays a major role in the variation of the charge-carrier density. The *n*-type conductivity may be related to Te-rich growth condition since antisite defects of the type Te_{Bi} (i.e., tellurium located on the site of bismuth) can contribute free electrons.

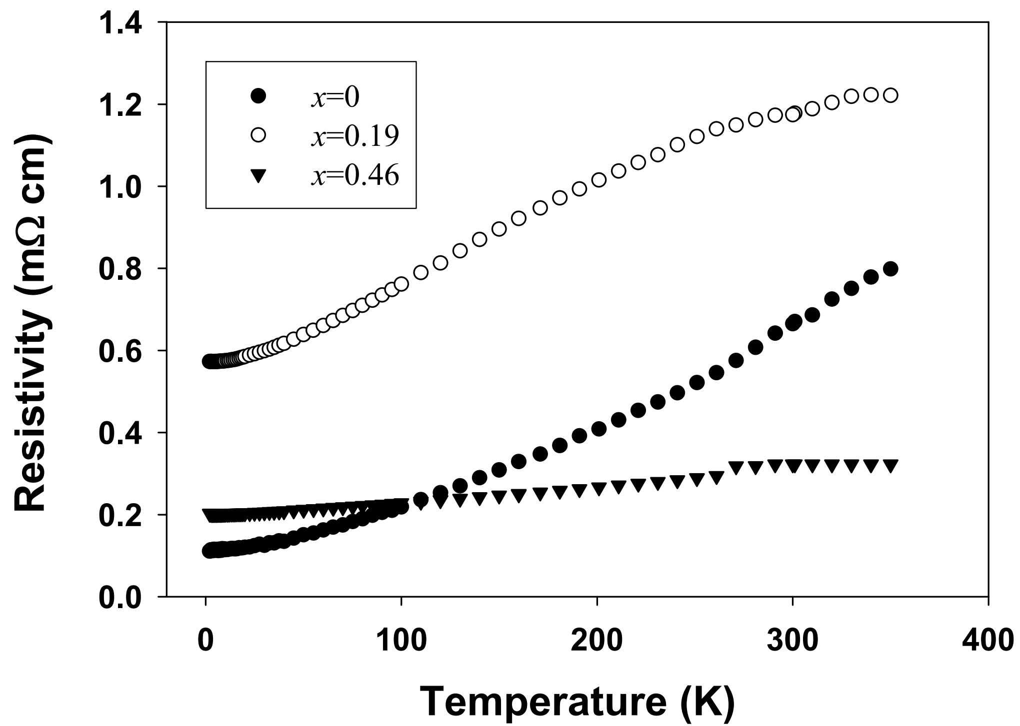

Figure 6.3 Temperature dependent electrical resistivity of $Bi_{2-x}Fe_xTe_3$ films in zero magnetic field.

Table 6.1 Carrier concentration (*n or p*), resistivity (ρ) and mobility (μ) of a single crystal of Bi_2Te_3 and of $Bi_{2-x}Fe_xTe_3$ films at 10K.

X	p(cm^{-3})	ρ(mΩ cm)	μ(cm^2/Vs)
0, Bulk single crystal	1.127×10^{19}	0.279	1989.02

X	n(cm^{-3})	ρ(mΩ cm)	μ(cm^2/Vs)
0	5.49×10^{19}	0.114	998.63
0.19	4.57×10^{19}	0.575	237.85
0.46	2.36×10^{20}	0.202	131.10

6.4.2 Magnetic Properties of *n*-Type $Bi_{2-x}Fe_xTe_3$

In order to study the magnetic properties, field-dependent magnetization measurement was done by using SQUID-based Magnetic Property Measurement System (MPMS). After subtracting the magnetic response from the substrate and background, the field-dependent magnetization *M*(H) curve obtained on the pure Bi_2Te_3 thin film sample showed a negative slop, indicating a diamagnetic behavior (negative magnetic susceptibility χ). The $Bi_{2-x}Fe_xTe_3$ epitaxial thin films (for x=0.19 and 0.46) have positive slop curves but no hysteresis loop was observed down to a temperature of 2K. This observation suggests that iron enters the structure in the form of ions and makes Bi_2Te_3 a paramagnetic material. The lack of spontaneous magnetic ordering was further confirmed by Hall effect measurement since no hysteresis in both magnetoresistance and the Hall resistivity was observed at a temperature of 2K. Moreover, in the temperature dependent resistivity curve (Fig. 6.5), no distinct slope change due to the spin-flip scattering at the FM–PM transition (as mentioned in 5.4.3) was observed.

6.5 Discussion

According the observation in 6.4.1, the iron atoms don't act as donors since the change of carrier concentration is mainly due to the antisite defects. If Fe with a valence value 2^+ substitutes the bismuth site, an extra free electron will be contributed and a strong relation between iron content and carrier concentration should be observed. Therefore, it is more likely that Fe^{3+} substitutes on the trivalent bismuth cation.

The RKKY interaction with mean field approximation as described in section

1.4 gives a reasonable explanation to our observation. Electrons have smaller effective masses and a small exchange integral, which impede the formation of ferromagnetic states; thus spontaneous magnetic ordering is hard to be obtained on these *n*-type $Bi_{2-x}Fe_xTe_3$ thin film samples.

Although the Te-rich growth condition brought a lot of convenience for sample preparation, a more precise flux ratio control should be taken to obtain *p*-type thin film samples which will definitely extended the depth of this study.

6.6 Summary

$Bi_{2-x}Fe_xTe_3$ epitaxial thin film samples (x=0, 0.19 and 0.46) had been successfully prepared by LT-MBE. Compared to the *p*-type bulk samples grown in stoichometry condition, these $Bi_{2-x}Fe_xTe_3$ thin films present *n*-type conductivity. This *n*-type behavior may be due to the Te-rich growth condition. This *n*-type $Bi_{2-x}Fe_xTe_3$ thin film samples showed simple paramagnetic behavior which is believed from Fe^{3+} ions incorporated in the Bi_2Te_3 matrix. According the prediction based on RKKY interaction with mean field approximation, the lack of spontaneous magnetic ordering is believed to be related to smaller effective masses and a small exchange integral of the conduction carriers—electrons in an *n*-type environment.

Chapter 7

F/N/F Trilayer Structure

7.1 Introduction

In Chapter 5, ferromagnetism of $Sb_{2-x}Cr_xTe$ thin films at 190K has been demonstrated. It is very intriguing to check if these ferromagnetic thin films could be used in some simple devices as an initial step of spintronic applications. In this chapter, a ferromagnetic/non-ferromagnetic/ferromagnetic (F/N/F) trilayer structure is introduced not only for demonstrating the capability of device fabrication but also for the study of interlayer interaction.

The configuration of these trilayer samples consists of two ferromagnetic $Sb_{2-x}Cr_xTe$ layers separated by a thin non-magnetic Sb_2Te_3 layer. It is very interesting to observe how the magnetic spins from two different layers interact and how the inserted non-magnetic layer and its thickness can alter this interaction. The interaction of this kind is called interlayer exchange coupling (IEC) which will be introduced more in a coming section.

7.2 Sample Preparation

Our trilayer structure $Sb_{2-x}Cr_xTe_3/Sb_2Te_3/Sb_{2-y}Cr_yTe_3$ comprises a pure nonmagnetic Sb_2Te_3 layer sandwiched by two ferromagnetic layers with different Cr doping concentrations, i.e., with different Curie temperatures. The capability of

precision layer-by-layer growth control of the MBE system makes it possible to fabricate this trilayer structure.

The growth parameters for Cr-doped Sb_2Te_3 epitaxial thin films obtained in Chapter 5 were used for the preparation of trilayer samples. Precision Cr concentrations and control of thin film thickness can be achieved in our MBE system. A thin undoped Sb_2Te_3 layer in the middle of the trilayer structure can be fabricated by interrupting the Cr flux. A short time interruption of Cr molecular beam flux is carried out by precision time shutter control of our miniature E-beam evaporator. During the interruption, Cr molecular beam flux can be tuned by adjusting the e-beam power to a desired and stable Cr concentration level for the deposition of the top ferromagnetic $Sb_{2-y}Cr_yTe_3$ layer.

Several trilayer samples with different spacer thicknesses (0, 2, 4, 10 nm) had been carefully prepared by the MBE thin film growth while the top and bottom ferromagnetic SbCrTe layers of these films were kept at the same thickness, namely 50nm. Clear streak-like patterns from *in-situ* RHEED monitoring persisted for the entire growth duration, indicating that these thin film samples were grown substantially in a good layer-by-layer fashion with nice crystalline quality. Thus, the assumption of pinhole free samples is convincing.

7.3 Interlayer Exchange Coupling (IEC)

Since the discovery of antiferromagnetic interlayer exchange coupling between ferromagnetic metals separated by a nonmagnetic metal or semiconductor spacers, [62,63,64,65,66] investigations of this kind have been extended to the so-called all semiconductor trilayer structures which typically represent two

ferromagnetic semiconductor layers separated by a semiconductor or insulator layer with a specific thickness. The interlayer exchange coupling (IEC) between the ferromagnetic layers through the nonmagnetic layer has been the focus of investigations. IEC between two ferromagnets separated by a nonmagnetic metal spacer has been studied both theoretically [67,68] and experimentally [62,63,64]. By replacing metallic ferromagnets with ferromagnetic semiconductors and the metallic spacer with a semiconductor, the so-called all semiconductor *F*/*N*/*F* trilayer structure can be fabricated and used to investigate the IEC in semiconductor nanostructures. So far, IEC in all-semiconductor *F*/*N*/*F* trilayer structures has only been studied in GaMnAs/AlGaAs/GaMnAs [69,70,71,72] and InMnAs/InAs/InMnAs [73] systems through tunneling magnetoresistance investigations. IEC in magnetic semiconductor nanostructures as a function of temperature and spacer thickness can also be studied with Hall effect measurements since abnormal Hall resistivity of a magnetic thin film is proportional to the magnetization which includes the IEC between the ferromagnetic layers.

7.4 IEC on F/N/F Trilayers

Figure 7.1 shows a schematic of the F/N/F trilayer structure. Two ferromagnetic layers, $Sb_{1.66}Cr_{0.34}Te_3$ on the top and $Sb_{1.81}Cr_{0.19}Te_3$ at the bottom, are separated by a thin layer of nonmagnetic Sb_2Te_3 whose thickness is varied from 0 to 10 nm. H_{c1} and H_{c2} are the coercive fields of $Sb_{1.81}Cr_{0.19}Te_3$ and $Sb_{1.66}Cr_{0.34}Te_3$ blocks, respectively, at a given temperature. Measurements of the individual films of $Sb_{1.81}Cr_{0.19}Te_3$ and $Sb_{1.66}Cr_{0.34}Te_3$ show that the Curie temperatures are 67 and 106 K, respectively. When the trilayer structure is cooled below the Curie temperature, its magnetic behavior is determined not only by the Cr-doped Sb_2Te_3 layers but also by the

IEC between these layers. As shown on the left-hand side of Fig. 7.2, when there is *no* IEC between the top and bottom layers, the total magnetization of the trilayer structure will be simply the sum of these two layers' magnetizations which are not correlated. If initially a high magnetic field (pointing up) is applied to saturate the trilayer structure and then the magnetic field is gradually reduced, the following behavior should be observed: (1) when $H>H_{c2}$, and since $H_{c2}>H_{c1}$, the spins in both the top and bottom Cr-doped Sb_2Te_3 layers will be aligned with the direction of the external magnetic field; (2) when the magnetic field is reduced and reversed and it satisfies $H_{c1}<|-H|<H_{c2}$, the spins in the top SbCrTe layer will still be aligned parallel to the original direction of the magnetic field, but the spins in the bottom layer will be reversed, i.e., pointing down. Therefore, the total magnetization will be reduced. A *two-step* decrease of the total magnetization will be observed as a result of sequential alignments of the spins in the bottom and top layers by the external magnetic field. If the field is further reduced to a condition $|-H|>H_{c2}$ and then reversed to the condition of stage 4, a similar two-step increase of the total magnetization will also be observed.

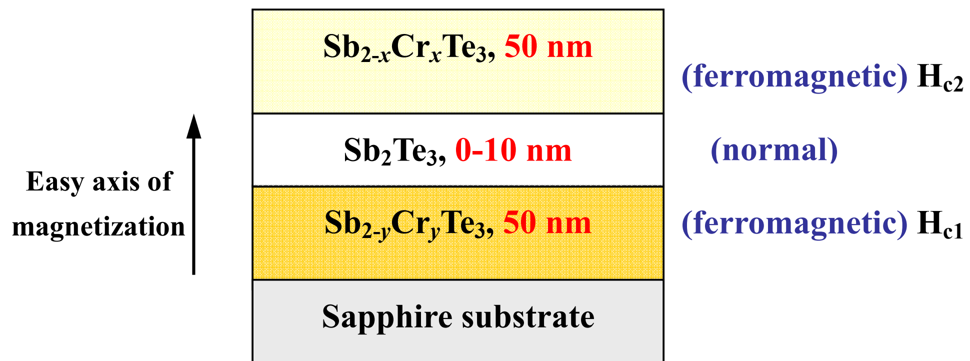

Figure 7.1 A schematic of the *F*/*N*/*F* trilayer structure based on $Sb_{2-x}Cr_xTe_3/Sb_2Te_3/Sb_{2-y}Cr_yTe_3$. The coercive fields for $Sb_{2-x}Cr_xTe_3$ and $Sb_{2-y}Cr_yTe_3$ ferromagnetic layers are assumed to be H_{c2} and H_{c1} respectively.

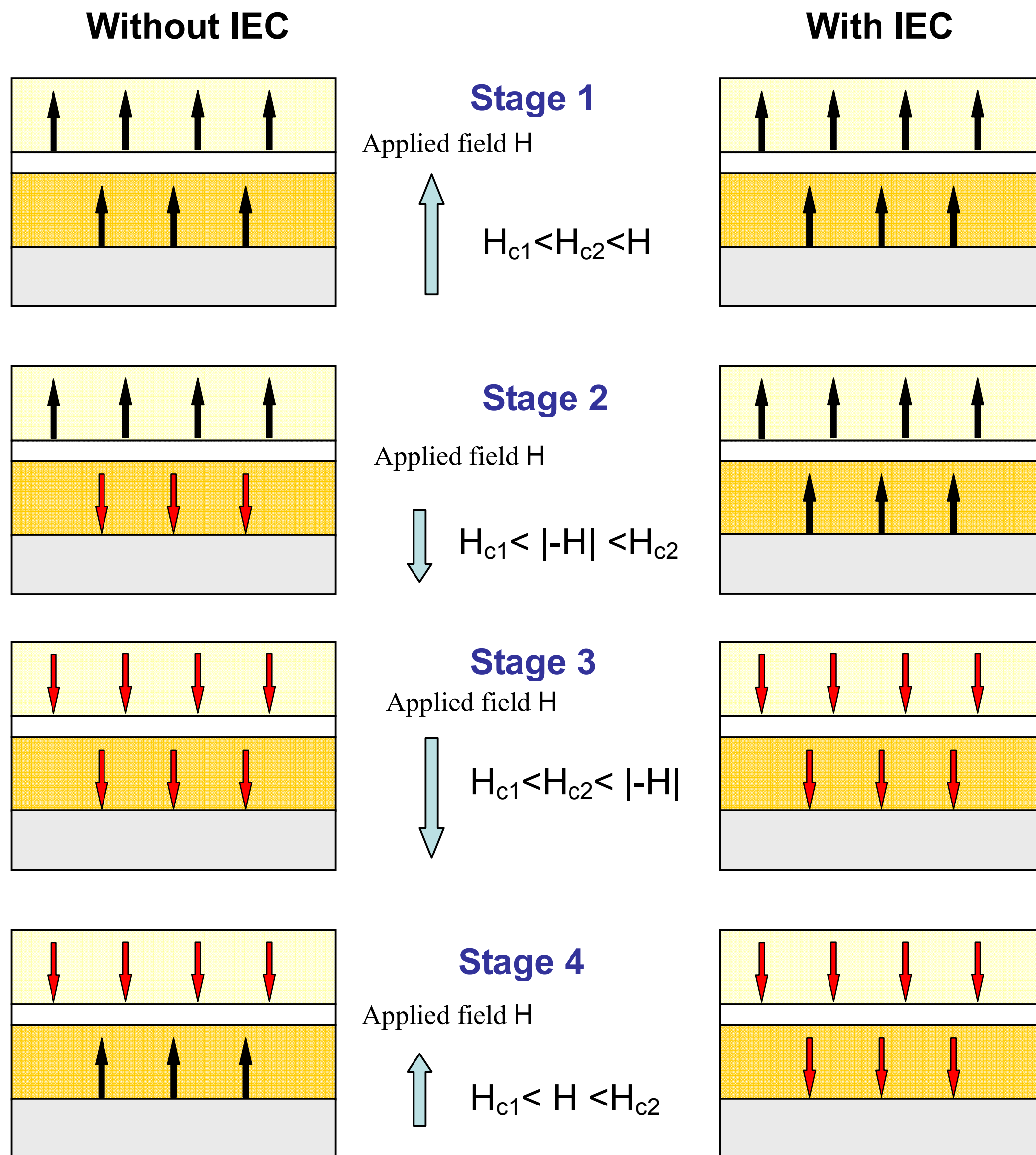

Figure 7.2 (Left side) A schematic of the spin configuration of the *F*/*N*/*F* trilayer *without* IEC. (Right) A schematic of the spin configuration of the *F*/*N*/*F* trilayer *with* IEC.

If we consider that the ferromagnetic IEC is present between the top and bottom Cr-doped layers, as depicted in Figure 7.1, the total magnetization of the trilayer structure will be determined by the sum of the magnetizations of the top and bottom layers plus the contribution from the ferromagnetic IEC. The ferromagnetic

IEC correlates the magnetic moments of the top and bottom layers, and now these two magnetizations behave like a single moment (a situation shown on the right-hand side of Fig. 7.2) instead of two uncorrelated moments. If a high magnetic field is applied to saturate the trilayer structure (assume again the direction of the external field is up) and then the field is gradually reduced, one should observe the following behavior described from stage 1 to 4: (1) when $|H|>H_{c2}$, and since $H_{c2}>H_{c1}$, the spins in both the top and bottom Cr-doped Sb_2Te_3 layers will be aligned with the direction of the external magnetic field; (2) when the magnetic field is reduced and reversed and it satisfies $H_{c1}< |-H| <H_{c2}$, the spins in the top layer obviously remain aligned to the original direction of the magnetic field and point up, and the spins in the bottom layer will also point up instead of down due to the ferromagnetic IEC between these two layers. The total magnetization of such a trilayer structure will be larger than that without ferromagnetic IEC. (3) When the field is further reduced and reaches a condition $|-H|<H_{c2,}$ all the spin in both layers follow the applied magnetic field and point down. (4) When the field is reversed again and increased to a value $H_{c1}< |H| <H_{c2}$ as shown in Fig. 7.2 stage 4; due to IEC, all spins remain pointing downward.

The difference between the hysteresis loops with and without IEC effect is very obvious. If IEC effect is not present, a clear two step pattern in the hysteresis loop should be easily seen. Therefore, the field dependence of magnetization will indicate whether there is ferromagnetic IEC or not in the trilayer structure.

7.5 Characteristics

Temperature dependent Hall resistivity of $Sb_{1.66}Cr_{0.34}Te_3$/ Sb_2Te_3/ $Sb_{1.81}Cr_{0.19}Te_3$ trilayer structures has been measured using an AC bridge with 16 Hz excitation. Figures 7.2(a), (c), (e), and (g) show the magnetic field dependent Hall

resistivity of the $Sb_{1.66}Cr_{0.34}Te_3/Sb_2Te_3/Sb_{1.81}Cr_{0.19}Te_3$ trilayer structures taken

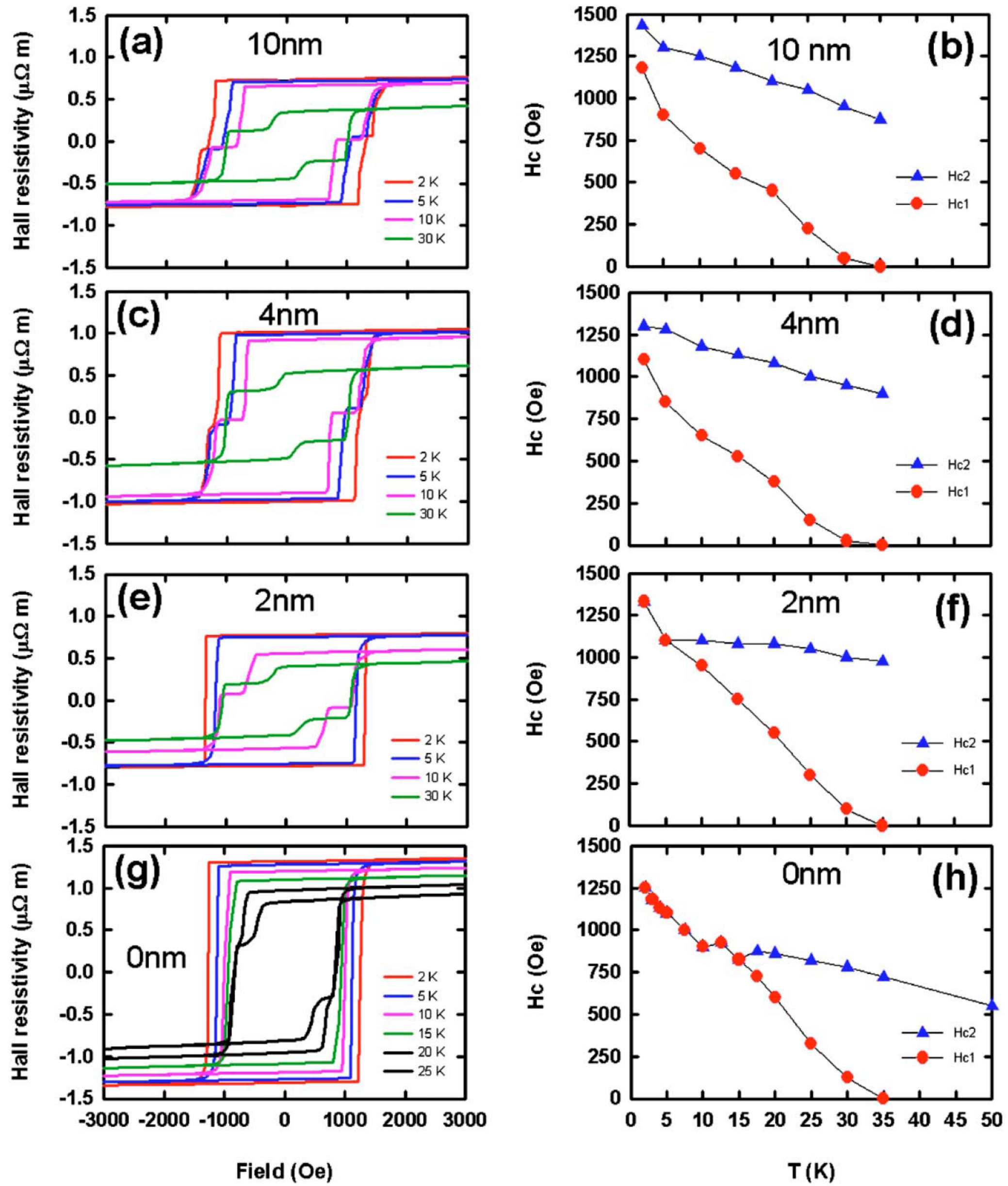

Figure 7.3 Magnetic field-dependent Hall resistivity for $Sb_{1.66}Cr_{0.34}Te_3$/ Sb_2Te_3/ $Sb_{1.81}Cr_{0.19}Te_3$ trilayer structures with various spacer thickness: (a) 10 nm, (c) 4 nm, (e) 2 nm, and (g) 0 nm. Coercive fields as a function of temperature for $Sb_{1.66}Cr_{0.34}Te_3$ /Sb_2Te_3/ $Sb_{1.81}Cr_{0.19}Te_3$ trilayer structures with various spacer thickness: (b) 10 nm, (d) 4 nm, (f) 2 nm, and (h) 0 nm.

at different temperatures and for the Sb_2Te_3 spacer thicknesses of 10, 4, 2, and 0 nm, respectively. For samples with the Sb_2Te_3 spacer layer thickness of 10 nm (Fig. 7.2(a)) and 4 nm (Fig. 7.2(c)), the Hall resistivity undergoes a two-step decrease when the magnetic field is reduced from 5 T and reversed, i.e., the spins in the top and bottom layers are rotated by the magnetic field independently at all temperatures down to 2 K. There is no ferromagnetic IEC in such trilayers since the top and bottom layers respond to the magnetic field separately. For samples with the Sb_2Te_3 spacer layer thicknesses of 2 nm (Fig. 7.2(e)) and 0 nm (Fig. 7.2(g)), there exists a critical temperature which tends to increase with the decreasing Sb_2Te_3 spacer thickness. Below such that critical temperature, the Hall resistivity undergoes only one-step transition when the magnetic field is reduced from 5 T and reversed, i.e., the spins in the top and bottom layers are rotated by the magnetic field in unison. The critical temperature is about 5 K for a sample with the Sb_2Te_3 spacer thickness of 2 nm and 15 K for a sample with the Sb_2Te_3 spacer thickness of 0 nm. The correlated behavior of the spins in both the top and bottom Cr-doped Sb_2Te_3 layers indicates that there is a strong ferromagnetic interlayer exchange coupling between the layers through the Sb_2Te_3 spacer when the thickness of the latter is small enough.

The strength of IEC between the ferromagnetic layers depends on several parameters that include but are not limited to the magnetization and thickness of the ferromagnetic layers. According to Parkin *et al.*,[64] an experimental measure of the strength of antiferromagnetic IEC includes the so called saturation field H_S, which is the field at which the magnetization curve first deviates from the high field slope. This field marks the strength of the antiferromagnetic IEC. The above authors then defined the strength of IEC in Co/Cr, Co/Ru, and Fe/Cr superlattices to be $H_S \cdot M \cdot t_f$, where H_S, M, and t_f are the saturation field, magnetization, and thickness of the

ferromagnetic layer, respectively. For ferromagnetic IEC in *F*/*N*/*F* trilayer structures, such definition is also valid since the saturation field H_S indicates the complete rotation and alignment of the ferromagnetically correlated spins in both F layers. H_S at 2 K is indicated with arrows in Figures 7.2(a), (c), (e), and (g). Since the anomalous Hall resistivity is proportional to the magnetization, the field at which the Hall data depart from the high field slope is the signature of the first deviation of magnetization from the high field slope. For a fixed ferromagnetic layer thickness and temperature, the ICE strength is a function of H_S only. Therefore, H_S can be used as a measure of the interlayer exchange coupling between the Cr-doped Sb_2Te_3 layers through the Sb_2Te_3 layer. Fig. 7.3 plots the dependence of H_S on the Sb_2Te_3 spacer thickness at temperatures ranging from 2 to 35 K. It is clear that the strength of ferromagnetic IEC in $Sb_{2-x}Cr_xTe_3/Sb_2Te_3/Sb_{2-y}Cr_yTe_3$ trilayer structures is both temperature and spacer thickness dependent. H_S tends to decrease with increasing temperature, but shows a complicated dependence on the spacer thickness. It is not clear at this moment whether the dependence of H_S on the spacer thickness at low temperature (25 K) is of oscillatory nature or not. More data points at various spacer thicknesses will be required to address this issue.

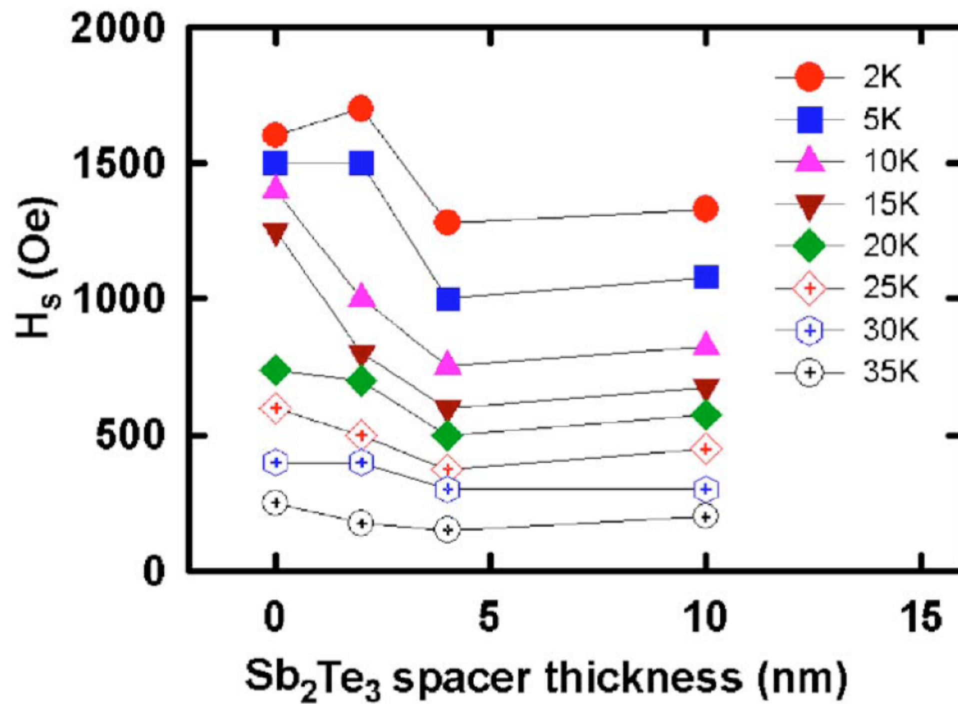

Figure 7.4 Saturation field H_S as a function of temperature and Sb_2Te_3 spacer thickness.

7.6 Summary

In summary, ferromagnetic interlayer exchange coupling was found in semiconductor $Sb_{1.66}Cr_{0.34}Te_3/Sb_2Te_3/Sb_{1.81}Cr_{0.19}Te_3$ trilayers as a function of both the Sb_2Te_3 spacer thickness and the temperature. At low temperatures and for small thickness of the spacer layer, the ferromagnetic IEC couples the two ferromagnetic layers and the entire trilayer structure behaves like a single magnetic layer. This finding opens the door for future applications of semiconductor spintronics based on the Sb_2Te_3 system such as ultrahigh density perpendicular magnetic recording that is being investigated.

Chapter 8
Conclusions

8.1 Conclusions

The objective of this thesis is twofold. One is to solidify the understanding of the ferromagnetic state that develops in the semiconducting lattice of Sb_2Te_3 and Bi_2Te_3 upon doping with certain transition metal ions based on intrinsic science interests. The other is to explore the potential for technological applications via the dual feature of charge carrier transport and spin manipulation.

The demonstrated high Curie temperatures observed in the tetradymite-type DMS thin film samples advance and broaden the scope of DMS system. In particular, the high anisotropic nature of the matrix, octahedrally bonded environment, and the distinctly different transition metals as opposed to manganese (Mn), all are believed to provide a new insight into the nature of magnetic interactions in semiconductors and make transition metal-doped Sb_2Te_3 and Bi_2Te_3 interesting study targets.

The tetradymite-based materials are not the mainstream of present-day semiconductor technology, but their excellent thermoelectric properties make them premier materials for thermoelectric application, particularly as thermoelectric coolers. The integration of the high-T_c transition metal-doped Sb_2Te_3 or Bi_2Te_3 films with a Sb_2Te_3/Bi_2Te_3 heterostructure thermoelectric cooler would not be difficult and might result in novel devices. Curie temperatures of 177K and 190K on $Sb_{2-x}V_xTe_3$ and

$Sb_{2-x}Cr_xTe_3$, respectively, have been achieved and multilayer thin film growth with precision control of transition metal concentration has also been demonstrated. These outcomes strongly support the future success in the fabrications and applications of the novel devices. Although high T_c might be obtained by increasing the doping, some drawbacks also appear at the same time. High doping with transition metals will eventually degrade the crystal quality and thus affect the electronic transport properties. The metal-like transport property of SbCrTe observed in Chapter 5 is an example. The trade off between high Curie temperature and good semiconductor property is a crucial concern for finding an optimal doping level.

The influence of charge carrier density on the magnetic state of the structure has been studied. The nature of transition metal impurity in the host lattice also has been partially explored although some issues remain to be clarified. In chapter 5, Curie temperature proportional to $xp^{1/3}$ is clearly observed where x is the impurity concentration and p is the density of holes. This observation suggests that the Ruderman-Kittel-Kasuya-Yoshida (RKKY) interaction is at play and the films thus represent an example of a diluted magnetic semiconductor (DMS).

8.2 Future Work

Diluted magnetic semiconductor quantum dots could be a good solution to overcome the drawback of material quality degradation due to heavier doping for higher T_c ferromagnets. The highly doped DMS can be localized in the quantum dots which play the role of a spin provider while the other part outside the quantum dots is still a normal semiconductor material with excellent transport properties. Based on the prediction of the mean field Zener model, higher density of states would increase the Curie temperature. A higher density of state of 1D quantum dot in comparison to the

density of states of the 3D structure can result in a higher Curie temperature.

The ferromagnetism is believed to be related to partically filled *d*-shells of transition metals which interplay with *sp*-orbitals of Sb_2Te_3 and Bi_2Te_3. In order to understand the mechanism, the valence states and lattice environment of these transition metal ions should be further clarified.

Rare-earth atoms have partially filled *f*-shells that carry magnetic moment that may couple with the sp-orbitals of Sb_2Te_3 and Bi_2Te_3. Such *s*, *p*-*f* interactions in rare-earth element-doped $A_2^{V}B_3^{VI}$ diluted magnetic semiconductors might play a similar role as in the case of transition metal-based tetradymite-type DMS. This new and vast area of explorations is likely to be a fertile ground for new magnetic phenomena and will be an exciting topic to be pursued by my successor in the laboratory.

BIBLIOGRAPHY

---

[1] A. Hirohata, Y. B. Xu, C. M. Guertler, and J. A. C. Bland, "Spin-dependent Electron Transport at the Ferromagnet/Semiconductor Interface," *J. Appl. Phys.* **85**, 5804 (1999).

[2] T. Kasuya and A. Yanase, "Anomalous Transport Phenomena in Eu-Chalcogenide Alloys," Rev. Mod. Phys. 40, 684-696 (1968).

[3] J.K. Furdyna, "Diluted magnetic semiconductors," *J. Appl. Phys.* **64**, R29-R64 (1988).

[4] J.K. Furdyna and J. Kossut, Vol. Eds., *Semiconductors and Semimetals*, R. K. Willardson and A.C. Beer, Yreatise Eds., Academic Press, **Vol. 25** (1988).

[5] T. Dietl, A. Haury, and Y. M. d'Aubigne, "Free Carrier-Induced Ferromagnetism in Structures of Diluted Magnetic Semiconductors," *Phys. Rev*. **B55**, R3347-R3350 (1997).

[6] H. Munekata, H. Ohno, S. von Molnar, A. Segumuller, L. L. Chang and L. Esaki, "Diluted magnetic III-V semiconductors," Phys. Rev. Lett. **63**, 1849 (1989).

[7] H. Ohno, H. Munekata, T. Penny, S. von Molnar and L. L. Chang, "Magnetotransport properties of *p*-type (In,Mn)As diluted magnetic III-V semiconductors," Phys. Rev. Lett. **68**, 2664 (1992)

[8] J. De Boeck**,** R. Oesterholt**,** A. Van Esch, H. Bender, C. Bruynseraede, C. Van Hoof, and G. Borghs, "Nanometer-scale magnetic MnAs particles in GaAs grown by molecular beam epitaxy," *Phys. Rev. Lett*. **68**, 2744 (1996)

[9] K.Y. Wang, R.P. Campion, K.W. Edmonds, M. Sawicki, T. Dietl, C.T. Foxon, B.L. Gallagher, "Magnetism in (Ga,Mn)As Thin Films with TC up to 173K,"

27th International Conference on the Physics of Semiconductors - ICPS-27. AIP Conference Proceedings, Volume 772, pp. 333-334 (2005)

[10] M. L. Reed, N. A. El-Masry, H. H. Stadelmaier, M.K. Ritums, M. J. Reed, C. A. Parker, J. C. Roberts, S. M. Bedair, "Room Temperature Ferromagnetic Properties of (Ga,Mn)N", Appl. Phys. Letters 79, 3473-3475 (2001).

[11] S. Dhar, O. Brandt, A. Trampert, L. Däweritz, K. J. Friedland, K. H. Ploog, J. Keller, B. Beschoten, and G. Güntherodt, "Origin of high-temperature ferromagnetism in (Ga,Mn)N layers grown on 4H–SiC(0001) by reactive molecular-beam epitaxy", *Appl. Phys. Letters* **82**, 2077-2079 (2003).

[12] Kenji Ueda, Hitoshi Tabata, and Tomoji Kawai, "Magnetic and electric properties of transition-metal-doped ZnO films," *Appl. Phys. Letters* **79**, 988-990 (2001)

[13] P. Sharma, A. Gupta, K. V. Rao, F. J. Owens, R. Sharma, R. Ahuja, J. M. Osorio Guillen, B. Johansson, and G. A. Gehring, "Ferromagnetism Above Room Temperature in Bulk and Transparent Thin Films of Mn-doped ZnO," *Nature Materials* **2**, 673-667 (2003).

[14] D. C. Kundaliya, S. Ogale, S. Lofland, S. Dhar, C. J. Metting, S. R. Shinde, Z. Ma, B. Varughese, K. V. Ramanujachary, L. Salamanca-Riba and T. Venketesan, "On the origin of high temperature ferromagnetism in low temperature processed Mn-Zn-O system," *Nature Materials* **3**, 709 (2004).

[15] Yuji Matsumoto, Makoto Murakami, Tomoji Shono, Tetsuya Hasegawa, Tomoteru Fukumura, Masashi Kawasaki, Parhat Ahmet, Toyohiro Chikyow, Shin-ya Koshihara, and Hideomi Koinuma, "Room-Temperature Ferromagnetism in Transparent Transition Metal-Doped Titanium Dioxide", *Science* **291**, 854-856 (2001).

[16] S. A. Chambers, S. Thevuthasan, R. F. C. Farrow, R. F. Marks, J. U. Thiele, L. Folks, M. G. Samant, A. J. Kellock, N. Ruzycki, D. L. Ederer, and U. Diebold, "Epitaxial growth and properties of ferromagnetic co-doped TiO_2 anatase," *Appl. Phys. Letters* 79, 3467-3469 (2001)

[17] N. Theodoropoulou, A. F. Hebard, M. E. Overberg, C. R. Abernathy, S. J. Pearton, S. N. Chu, and R. G. Wilson, "Unconventional Carrier-Mediated Ferromagnetism above Room Temperature in Ion-Implanted (Ga, Mn)P:C," *Phys. Rev. Lett.* **89**, 107203/1-4 (2002).

[18] Gennadiy A. Medvedkin, Takayuki Ishibashi, Takao Nishi, Koji Hayata, Yoichi Hasegawa and Katsuaki Sato, "Room Temperature Ferromagnetism in Novel Diluted Magnetic Semiconductor $Cd_{1-x}Mn_xGeP_2$," *Jpn. J. Appl. Phys.* **39**, L949-L951 (2000).

[19] Sunglae Cho, Sungyoul Choi, Gi-Beom Cha, Soon Cheol Hong, Yunki Kim, Yu-Jun Zhao, Arthur J. Freeman, John B. Ketterson, B. J. Kim, Y. C. Kim, and Byung-Chun Choi, **"**Room-Temperature Ferromagnetism in $(Zn_{1-x}Mn_x)GeP_2$ Semiconductors**,"** *Phys. Rev. Lett.* **88**, 257203/1-4 (2002).

[20] Tomasz Dietl, "Dilute magnetic semiconductors: Functional ferromagnets," *Nature Materials* **2**, 646-648 (2003)

[21] C. Zener, "Interaction Between the *d*-Shells in the Transition Metals," *Phys. Rev.* **81**, 440 (1951).

[22] H. Akai, "Ferromagnetism and Its Stability in the Diluted Magnetic Semiconductor (In, Mn)As," *Phys. Rev. Lett.* **81**, 3002-3005 (1998).

[23] Jürgen König, Hsiu-Hau Lin, and Allan H. MacDonald, "Theory of Diluted Magnetic Semiconductor Ferromagnetism," *Phys. Rev. Lett.* **84**, 5628-5631 (2000).

[24] Masafumi Shirai, Takaki Ogawa, Isao Kitagawa and Naoshi Suzuki, "Band structures of zinc-blende-type MnAs and $(MnAs)_1(GaAs)_1$ superlattice," *Journal of magnetism and magnetic materials* **177-181**, 1383-1384 (1998).

[25] T. Ogawa, M. Shirai, N. Suzuki and I. Kitagawa, "First-principles calculations of electronic structures of diluted magnetic semiconductors (Ga,Mn)As," *Journal of magnetism and magnetic materials* **196-197**, 428-429 (1998).

[26] J. S. Dyck, P. Hájek, P. Lošťák, and C. Uher, "Diluted magnetic semiconductors based on $Sb_{2-x}V_xTe_3$ ($0.01 \leq x \leq 0.03$)," *Phys. Rev. B* **65**, 115212 (2002).

[27] V. A. Kul'bachinski, A. Yu. Kaminski, K. Kindo, E. Naryumi, K. Suga, P. Lostak, and P. Svanda, "Low-temperature ferromagnetism in a new diluted magnetic semiconductor $Bi_{2-x}Fe_xTe_3$," *Journal of Experimental and Theoretical Physics Letters* **73**, 352 (2001).

[28] H. Scherrer and S. Scherrer, "Bismuth Telluride, Antimony Telluride, and their Solid Solutions," in *CRC Handbook of Thermoelectronics*, ed. By D. M. Rowe (Chemical Rubber, Boca Raton, FL, 1995), pp.211-237.

[29] V. A. Kul'bachinski, H. Ozaki, Y. Miyahara, and K. Funagai, "A tunneling spectroscopy study of the temperature dependence of the forbidden band in Bi_2Te_3 and Sb_2Te_3 ," *Journal of Experimental and Theoretical Physics Letters* **97**, 1212-1218 (2003).

[30] Y. Tokura and N. Nagaosa, "Orbital Physics in Transition-Metal Oxides," *Science* **288**, 462 (2000).

[31] R. D. Shannon, "Revised Effective Ionic Radii and Systematic Studies of Interatomic Distances in Halides and Chalcogenides", *Acta Cryst.* **A32** 751-767 (1976).

[32] E. Groubert and A. Boyer, “Structural and electrical properties of bismuth telluride films grown by the molecular beam technique,” *Journal of materials science letters* **7**, 575-577 (1998)

[33] Y. Iwata, H. Kobayashi, S. Kikuchi, E. Hatta, K. Mukasa, “In situ refection high-energy electron diffraction (RHEED) observation of Bi_2Te_3/Sb_2Te_3 multilayer film growth,” *Journal of Crystal Growth* **203**, 125-130 (1999)

[34] A. Giani, F. Pascal-Delannoy, A. Boyer, A. Foucaran, M. Gschwind and P. Ancey, “Elaboration of Bi_2Te_3 by metal organic chemical vapor deposition,” *Thin solid films*, 303, 1-3 (1997)

[35] W. Kern and J. Vossen, Eds., “*Thin Film Processes*,” Academic Press: New York, 1978, Ch V-1.

[36] W. Braun, Applied RHEED, Springer Tracts in Modern Physics, vol. 154, Springer-Verlag, Berlin, 1999.

[37] I. Hernández-Calderón and H. Höchst, “New method for the analysis of reflection high-energy electron diffraction: α-Sn(001) and InSb(001) surfaces,” *Phys. Rev. B.* **27**, 4961-4965 (1983),

[38] H.H. Farrell and C. J. Palmstrøm, “Reflection high energy electron diffraction characteristic absences in GaAs(100) (2×4)–As: A tool for determining the surface stoichiometry,” *J. Vac. Sci. Technol. B.* **8,** 903. (1990),

[39] T. Hashizume, Q.K. Xue, J. Zhou, A. Ichimiya and T. Sakurai, **“**Structures of As-Rich GaAs(001)-(2×4) Reconstructions,” *Phys. Rev. Lett.* **73**, 2208-2211(1994).

[40] P. K. Larson, J.H. Neave, J.F. van der Veen, P.J. Dobson and B.A. Joyce, **“**GaAs(001)-*c*(4×4): A chemisorbed structure,” *Phys. Rev. B.* **27**, 4966-4977 (1983).

[41] L. Wang, P. Kratzer and M. Scheffler, “Energetics of InAs thin films and islands on the GaAs(001) substrate,” *Jpn. J. Appl. Phys.* **39** (2000), p. 4298-4301

[42] D.W. Pashley, J.H. Neave and B.A. Joyce, “A model for the appearance of chevrons on RHEED patterns from InAs quantum dots,” *Surf. Sci.* **476** , 35-42 (2001).

[43] T. Hanada, B.-H. Koo, H. Totsuka and T. Yao, “Anisotropic shape of self-assembled InAs quantum dots: Refraction effect on spot shape of reflection high-energy electron diffraction,**”** *Phys. Rev. B.* **64**, 165307 [6 pages] (2001).

[44] H. P. Klug and L. E. Alexandewr, “X-ray Diffraction Procedures For Polycrystalline and Amorphous Materials,” New York; John Wiley & Sons (1974).

[45] D. A. Neumann, Xiaomei Zhu, H. Zabel, T. Henderson, R. Fischer, W. T. Masselink, J. Klem, C. K. Peng, and H. Morkoç, “Structural properties of GaAs on Si and Ge substrates**,”** *Journal of Vacuum Science & Technology B* **4**, 642-644 (1986).

[46] A. Arrott and J. Noakes, “Approximate equation of state for nickel near its critical temperature,” Phys. Rev. Lett 19, 786-789 (1967).

[47] P. E. Brommer and J. J. M. Franse, in Ferromagnetic materials, eds. K. H. J. Buschow and E. P. Wohlfarth, vol. 5 (North-Holland, Amsterdam, 1990) p.323

[48] A. Arrott, “Criterion for Ferromagnetism from Observations of Magnetic Isotherms,” *Phys. Rev.* **108**, 1394 (1957).

[49] *The Hall Effect and its Applications*, edited by C. L. Chien and C. R. Westgate Plenum, New York, 1980.

[50] J. S. Dyck, Č. Drašar, P. Lošták, and C. Uher, "Low-temperature ferromagnetic properties of the diluted magnetic semiconductor $Sb_{2-x}Cr_xTe_3$," Phys. Rev. B **71**, 115214 (2005).

[51] H. Saito, V. Zayets, S. Yamagata, and K. Ando, "Room-Temperature Ferromagnetism in a II-VI Diluted Magnetic Semiconductor $Zn_{1-x}Cr_xTe$," *Phys. Rev. Lett.* **90**, 207202 (2003).

[52] Y.-J. Chien, Z. Zhou, and C. Uher, "Growth and transport properties of $Sb_{2-x}V_xTe_3$ thin films on sapphire substrates," J. Cryst. Growth **283**, 309 (2005).

[53] S. von Molnar and T. Kasuya, "Evidence of Band Conduction and Critical Scattering in Dilute Eu-Chalcogenide Alloys," Phys. Rev. Lett. **21**, 1757-1761 (1968).

[54] T. Kasuya, Prog. Theor. Phys. **16**, 45 (1956).

[55] V. A. Kulbachinskii, P. M. Tarasov, and E. Brueck, "Anomalous transport and ferromagnetism in the diluted magnetic semiconductor $Sb_{2-x}Cr_xTe_3$," *Physica B* **368**, 32 (2005).

[56] F. Matsukura, H. Ohno, A. Shen, and Y. Sugawara, "Transport properties and origin of ferromagnetism in (Ga,Mn)As," *Phys. Rev. B* **57**, R2037 (1998).

[57] A. Oiwa, S. Katsumoto, A. Endo, M. Hirasawa, Y. Iye, H. Ohno, F. Matsukura, A. Shen, and Y. Sugawara, "Nonmetal-metal-nonmetal transition and large negative magnetoresistance in (Ga, Mn)As/GaAs," Solid State Commun. **103**, 209-213 (1997).

[58] J. C. Fuggle and N. Mårtensson, "Core-Level Binding Energies in Metals," *J. Electron Spectrosc. Relat. Phenom.*, 1980, **21**, 275.

[59] T. Jungwirth, W. A. Atkinson, B. H. Lee, and A. H. MacDonald, Phys. Rev. B **59**, 9818 (1999).

[60] C. H. Ziener, S. Glutsch, and F. Bechstedt, *Phys. Rev. B* **70**, 075205 (2004)

[61] V. A. Kul'bachinskii, A. Yu. Kaminskii, K. Kindo, Y. Narumi, K. Suga, P. Lostak and P. Svanda, "Low-temperature ferromagnetism in a new diluted magnetic semiconductor $Bi_{2-x}Fe_xTe_3$," *JETP letter* **73**, 352-356 (2001)

[62] P. Gruenberg, R. Schreiber, Y. Pang, M. B. Brodsky, and H. Sowers, "Layered Magnetic Structures: Evidence for Antiferromagnetic Coupling of Fe Layers across Cr Interlayers," *Phys. Rev. Lett.* **57**, 2442-2445 (1986).

[63] M. N. Baibich, J. M. Broto, A. Fert, F. Nguyen Van Dau, F. Petroff, P. Eitenne, G. Creuzet, A. Friederich, and J. Chazelas, "Giant Magnetoresistance of (001)Fe/(001)Cr Magnetic Superlattices," Phys. Rev. Lett. **61**, 2472-2475 (1988).

[64] S. S. P. Parkin, N. More, and K. P. Roche, "Oscillations in exchange coupling and magnetoresistance in metallic superlattice structures: Co/Ru, Co/Cr, and Fe/Cr," *Phys. Rev. Lett*. **64**, 2304-2307 (1990).

[65] R. R. Gareev, D. E. Buergler, M. Buchmeier, D. Olligs, R. Schreiber, and P. Gruenberg, "Metallic-Type Oscillatory Interlayer Exchange Coupling across an Epitaxial FeSi Spacer," *Phys. Rev. Lett.* **87**, 157202 (2001).

[66] Z. Y. Liu and S. Adenwalla, "Oscillatory Interlayer Exchange Coupling and Its Temperature Dependence in $[Pt/Co]_3/NiO/[Co/Pt]_3$ Multilayers with Perpendicular Anisotropy," *Phys. Rev. Lett.* **91**, 037207 (2003).

[67] P. Bruno, "Theory of interlayer magnetic coupling," *Phys. Rev. B* **52**, 411-439 (1995)

[68] L. L. Hinchey and D. L. Mills, "Magnetic properties of superlattices formed

from ferromagnetic and antiferromagnetic materials," *Phys. Rev. B* **33**, 3329-3343 (1986)

[69] N. Akiba, F. Matsukura, A. Shen, Y. Ohno, H. Ohno, A. Oiwa, S. Katsumoto, and Y. Iye, "Interlayer exchange in (Ga,Mn)As/(Al,Ga)As/(Ga,Mn)As semiconducting ferromagnet/nonmagnet/ferromagnet trilayer structures," *Appl. Phys. Lett.* **73**, 2122-2124 (1998)

[70] D. Chiba, N. Akiba, F. Matsukura, Y. Ohno, and H. Ohno, "Magnetoresistance effect and interlayer coupling of (Ga, Mn)As trilayer structures ," *Appl. Phys. Lett.* **77**, 1873-1875 (2000)

[71] S. J. Chung, S. Lee, I. W. Park, X. Liu, and J. K. Furdyna, "Possible indication of interlayer exchange coupling in GaMnAs/GaAs ferromagnetic semiconductor superlattices ," *J. Appl. Phys.* **95**, 7402-7404 (2004).

[72] P. Sankowski and P. Kacman, "Interlayer exchange coupling in (Ga,Mn)As-based superlattices**,"** *Phys. Rev. B* **71**, 201303(R) (2005).

[73] S. Yanagi, H. Munekata, Y. Kitamoto, A. Oiwa, and T. Slupinski, "Interlayer coupling in (In,Mn)As/InAs/(In,Mn)As magnetic semiconductor trilayer structures," *J. Appl. Phys.* **91**, 7902-7904 (2002).